The Development and Application of SubLIME: Sublimation of Laboratory Ices Millimeter/submillimeter Experiment

By

Katarina M. Yocum

A dissertation submitted in partial fulfillment of

the requirements for the degree of

Doctor of Philosophy

(Chemistry)

at the

University of Wisconsin-Madison

2022

Date of final oral examination: 01/07/2022

This dissertation is approved by the members of the Doctoral Committee:
Susanna L. Widicus Weaver, Department of Chemistry, UW-Madison
Gilbert M. Nathanson, Department of Chemistry, UW-Madison
Etienne Garand, Depatment of Chemistry, UW-Madison
Stefanie N. Milam, Astrochemistry Laboratory, NASA Goddard Space Flight Center

Declaration of Authorship

I, Katarina M. Yocum, declare that this thesis titled, "The Development and Application of SubLIME: Sublimation of Laboratory Ices Millimeter/submillimeter Experiment" and the work presented in it are my own. I confirm that:

- This work was done wholly or mainly while in candidature for a research degree at this University.
- Where any part of this thesis has previously been submitted for a degree or any other qualification at this University or any other institution, this has been clearly stated.
- Where I have consulted the published work of others, this is always clearly attributed.
- Where I have quoted from the work of others, the source is always given. With the exception of such quotations, this thesis is entirely my own work.
- I have acknowledged all main sources of help.
- Where the thesis is based on work done by myself jointly with others, I have made clear exactly what was done by others and what I have contributed myself.

Signed:

_____

Date:

_____

Abstract

Katarina M. Yocum

The Development and Application of SubLIME: Sublimation of Laboratory Ices Millimeter/submillimeter Experiment

The work presented in this dissertation involved the development of a laboratory technique to reveal new information about cosmic ice chemistry. The Sublimation of Laboratory Ices Millimeter/submillimeter Experiment (SubLIME) combines millimeter and submillimeter (mm/submm) spectroscopy, infrared spectroscopy, and mass spectrometry to explore the connection between ice and gas chemistry in cold regions of space by studying the intricate details of sublimation. The studies examined ice chemistry driven by UV photons, how those chemical reactions differ under temperature variations, and how UV photons and heat effect the sublimation process. Procedures were developed for determining surface binding energy, sublimation enthalpy, rotational temperature, and gas density. The millimeter/submillimeter spectroscopic technique can unambiguously identify structural isomers, conformational isomers, and isotopologues, making it highly complementary to previous gas-phase mass spectrometry techniques typically implemented for laboratory cosmic ice studies. Furthermore, the laboratory spectra are directly comparable to observational data from submillimeter/far-IR telescopes and provide an avenue for laboratory modeling of telescope data to guide future observational discoveries.

Acknowledgements

It has been a crazy trip these past 4.5 years of graduate school. I have learned more than I could have ever imagined when I first started my degree in September 2017. I've been introduced to countless fields of science. I've been exposed to the competitive research side of academia in America. I traveled across the country to several new cities and states to present my research and met many incredible people along the way. This trip was one that I could not have managed on my own and I must acknowledge those who helped make it successful.

Dr. Susanna Widicus Weaver, my PhD advisor, you have offered me many unique opportunities during my time in your research group. You presented me with a very challenging thesis project that I have loved and hated all at the same time. Most importantly, you taught me how to be a completely independent scientist. You gave me the freedom to take this project to be my own and were never upset with me when I would take it in a new direction. I loved that I had that trust and freedom. You introduced me to the worlds of rotational spectroscopy and radio astronomy. Lastly, you allowed me to move to an entirely different state to conduct research at an amazing institution, NASA Goddard Space Flight Center, for the past year and a half. This was a truly unique opportunity that I hope other students have the chance to experience. Thank you for your support and knowledge.

Dr. Stefanie Milam, I considered you to be my co-advisor. You have also provided me with many unique opportunities the past few years. You taught me that no matter how hard I work, I can always work harder and achieve more. You are a very caring mentor who is constantly sending me opportunities to get exposed to the field and connecting me with other great scientists. Thank you for helping to bring me to Goddard where you gave me the opportunity to build a brand-new lab at NASA and to even be a part of choosing the lab name. There are not many graduate students who can say that. I am looking forward to working with you after

graduation and to always RTFM.

Dr. Rolf Mayrhofer, my first true mentor, you have always been an inspiration for me. Your fascinating and well-planned lectures inspired me to pursue physical chemistry. Physical chemistry is a very challenging field, but the way you explained the concepts was very understandable and demonstrated to me that I was intelligent enough to study physical chemistry. You were very encouraging and without that I would not have gone to graduate school. Thank you for all of your letters of recommendation and your endless support. It is obvious that you want your students to be successful. Any student that gets to work with you is very lucky because you are a truly special mentor.

The first two research mentors I worked with, Dr. Mark Loeffler and Dr. Reggie Hudson, both deserve a big thank you. Mark, you taught me everything there is to know about building an ultrahigh vacuum chamber which was a key to my success in graduate school. You have always been supportive in writing me letters of recommendation and even answering research questions over email years after working directly with you. Reggie, you introduced me to astrochemistry and taught me so much fundamental knowledge about the field. That knowledge was also a key to my success as a graduate student. Thank you both for exposing me to cosmic ice chemistry at a young age. You have both played an important role in my career.

Dr. Perry Gerakines, you have been a very helpful mentor during my graduate career. I have learned a lot from you. Everything from how to be a better writer to tricks to use in the lab to how to pronounce acetaldehyde. Your presence on my thesis project was very important. You greatly helped to secure funding for my entire degree and allowed me to borrow pretty much whatever I needed while we were building a new lab during a pandemic. Thank you for being so supportive of this project!

I must give a huge thank you to all the students that worked with me on my thesis project. First, Houston Smith, you introduced me to the project and taught me how to use the mm/submm spectrometer. You also came up with the design of the new vacuum chamber and purchased many of the instruments that were incorporated. Leslie Mora, you were the first undergraduate student that I ever mentored. We had so much fun together. You helped me collect data, analyze data, design a

fully digital notebook, and you helped with the early stages of building the new experimental setup. Ethan Todd, you were a pleasure to work with. You helped me write data acquisition code, write data analysis code, collect data, analyze data, characterize the UV lamp, build the experimental setup, and you were so fast to produce results. Chris Schwaiger, you always made lab fun. You helped me build the experimental setup, calibrate instruments, characterize the UV lamp, and design a multipass spectrometer. Nathan Harper, you didn't work directly with me, but you did help me numerous times in the lab with installing the cryostat, tightening and loosening bolts, and lifting heavy things. Morgan Giese, you were the first student that I mentored completely virtually. Despite being multiple states apart, you managed to learn Python, write a successful data analysis program, and discovered that the absorption signal line shape is not a pure second derivative Gaussian. You are all so brilliant and I loved working with you! You taught me so much and I hope you learned as much from me as I did from all of you.

I would be totally lost if it weren't for my friends. I must extend a very special shoutout to Hayley Bunn and Connor Wright– my lab mates and my best friends. I likely would have dropped out if I didn't have you both. We have so many memories and I am so happy to have you as lifelong friends. Thank you for all the science conversations, reminding me what simple words mean, lab shenanigans, coffee runs, and all the times you kept me sane. Dr. Alec Kroll, thank you for helping edit my abstracts and papers, teaching me useful lab skills, meaningful science conversations, having great taste in music, and all of the fun times we shared. Chase Shultz, thank you for your help in lab holding, lifting, tightening, untightening, and your kind presence as my desk neighbor. Dr. Kevin Roenitz, thank you for teaching me how to always stand my ground and boosting my confidence.

Jake Barnes, my best friend and life partner, thank you for always supporting me, complementing me, grounding me, and for all of the intelligent extraordinary conversations we have. You have always been my number one advocate. You have provided financial support during my poor college student years for rent, groceries, and way too much take-out. You provided programming support and taught me the basics of Python. Most importantly, you gave me courage to keep going when I thought I couldn't anymore, and I am forever grateful for you.

Contents

Declaration of Authorship i

Abstract ii

Acknowledgements iii

1 Introduction 1

1.1 Introduction to Astrochemistry . . . 1

1.1.1 Cosmic Ice Chemistry . . . 3

Laboratory Cosmic Ice Chemistry . . . 4

1.1.2 Rotational Spectroscopy as a Tool for Laboratory Astrochemistry 5

1.2 Dissertation Overview . . . 6

2 Experimental Methods 8

2.1 SubLIME Setup Descriptions . . . 8

2.1.1 Emory University Experimental Setup 1 . . . 8

2.1.2 Emory University Experimental Setup 2 . . . 10

2.1.3 NASA GSFC Experimental Setup 3 . . . 12

2.2 Analytical Techniques . . . 14

2.2.1 Millimeter/submillimeter Spectroscopy . . . 14

Submillimeter Limits of Detection . . . 16

Optical Filter Tests . . . 18

2.2.2 Infrared Spectroscopy . . . 19

2.2.3 Mass Spectrometry . . . 20

2.2.4 Laser Interferometry . . . 21

2.3 Energetic Processing of Ice Samples . . . 23

2.3.1 UltraViolet (UV) Processing . . . 23

UV Flux Characterization . . . 23
UV Photolysis and Photodesorption Experiments . . . 26
2.3.2 Thermal Processing . . . 27

3 Proof-of-Concept: Submillimeter Spectroscopic Detection of Sublimated Ice Samples 28

3.1 Introduction . . . 28
3.2 Background . . . 29
3.2.1 Comparison of Laboratory Techniques . . . 29
3.2.2 Thermal Desorption of Water and Methanol Ice Samples . . . 30
3.3 Experimental Methods . . . 32
3.3.1 Thermal Desorption of Ice Samples . . . 32
3.4 Results and Discussion . . . 32
3.4.1 Thermal Desorption of H_2O, D_2O, and CH_3OH . . . 32
3.5 Conclusions and Future Work . . . 40

4 Structure-Specific Identifications of Products of UV-photolyzed Methanol Ice with SubLIME 41

4.1 Introduction . . . 41
4.2 Experimental Techniques . . . 43
4.2.1 Ice Sample Creation . . . 44
4.2.2 UV Photolysis and Thermal Processing of Ice Samples . . . 44
4.2.3 Infrared Spectra of Methanol Ices . . . 45
4.2.4 Submillimeter/far-IR Spectra of Sublimated UV-Photolyzed Methanol Ices . . . 45
4.2.5 Standards and Background Tests . . . 46
4.3 Results and Analysis . . . 48
4.3.1 Low Temperature UV Photolysis at 12 K . . . 48
4.3.2 Heating from 12 to 300 K . . . 50
4.3.3 Gas-phase Composition at 300 K . . . 51
Ketene C_2H_2O . . . 53
The C_2H_4O Isomers Acetaldehyde, Ethylene Oxide, and Vinyl Alcohol . . . 53

The C_2H_6O Isomers Ethanol and Dimethyl Ether 55
The $C_2H_4O_2$ Isomers Methyl Formate, Glycolaldehyde, and Acetic Acid 57
The $C_2H_6O_2$ Isomers Ethylene Glycol and Methoxymethanol . 59
Acetone $(CH_3)_2CO$ 60
4.3.4 Rotation Diagram Analysis Procedure and Results 61
4.4 Discussion 66
4.4.1 The Benefits of Utilizing Submillimeter/far-IR Spectroscopy to Identify Products of Sublimated Astrophysical Ices 66
Direct Comparison to Submillimeter/Far-IR Telescope Data . . 66
Detection and Quantification of Structural Isomers, Conformational Isomers, and Isotopologues 68
4.4.2 Methanol Branching Ratio Implications 68
4.4.3 Astrophysical Implications 70
4.5 Conclusions 74

5 UV Photodesorption Studies of Water, Methanol, and Carbon Monoxide Ices **75**
5.1 Introduction 75
5.2 Experimental Methods 79
5.2.1 Water 80
5.2.2 Methanol 80
5.2.3 Carbon Monoxide 81
5.3 Results and Discussion 82
5.3.1 Preliminary Tests 82
5.3.2 Water Photodesorption 83
5.3.3 Methanol Photodesorption 84
5.3.4 Carbon Monoxide Photodesorption 87
5.3.5 Limitations of SubLIME for Photodesorption Experiments . . . 89
5.4 Conclusions 90

6 Conclusions and Future Directions **93**
6.1 Conclusions 93

6.2 Future Directions of SubLIME 94
6.2.1 Spectroscopic Techniques 94
6.2.2 Conformational and Structural Isomer Analysis of Important Prebiotic Molecules 96

A Additional Details on Spectral Analysis **97**
A.1 Submillimeter Spectral Assingment 97
A.2 Rotation Diagram Analyses Parameters 97

Bibliography **99**

List of Figures

1.1 Life Cycle of a Star . . . 2
1.2 Space Weathering Processes of Interstellar Ice . . . 4

2.1 Emory University Experimental Setup 1 . . . 9
2.2 Emory University Chamber Rebuild (Before/After) . . . 10
2.3 Emory University Experimental Setup 2 . . . 11
2.4 Spectral Power: Z-cut Quartz vs. Sapphire Viewports . . . 12
2.5 NASA GSFC Experimental Setup 3 . . . 13
2.6 Schematic of the Millimeter/submillimeter Spectrometer . . . 15
2.7 WR9-SGx-M Transmitter Frequency Outputs . . . 15
2.8 Limit of Detection: H_2O . . . 17
2.9 Fast-Sweep Detection of Methanol . . . 18
2.10 Noise Reduction with an Optical Filter . . . 19
2.11 Ice Deposition Interference Fringes . . . 22
2.12 H_2O Ice Sublimation Rates: 155 K vs. 150 K . . . 22
2.13 Circuit Schematic for UV Flux Measurements . . . 24
2.14 UV Flux Measurements: Saturation Current . . . 25
2.15 UV Flux Measurements: Flux vs. Microwave Power . . . 25
2.16 UV Flux Measurements: Flux vs. H_2 Gas Pressure . . . 26

3.1 Submillimeter Spectroscopic Detections of Sublimated Ice Samples: H_2O, D_2O, and CH_3OH . . . 34
3.2 Linear Relationship of Submillimeter Absorption Signal vs. Thermal Desorption Rate . . . 35
3.3 Thermal Desorption of H_2O Ice Samples: First-Order Kinetics . . . 36

3.4 TPD Curves of H_2O Ice: Submillimeter Spectroscopy vs. Mass Spectrometry . . . 37
3.5 Exponential Fit of H_2O Ice TPD to Determine Surface Binding Energy . 38
3.6 Clausius-Clapeyron Relationship: H_2O Ice Sample (145 - 175 K) 39

4.1 IR Spectra of a UV-Photolyzed Methanol Ice Sample (12 K) 49
4.2 IR Spectra of CH_3OH Ice Before/After Photolysis 49
4.3 IR Spectra UV-Photolyzed CH_3OH Ice Sample Warmup 51
4.4 Broadband Submillimeter Spectra of a Sublimated UV-Photolyzed CH_3OH Ice Sample 52
4.5 Ketene Detections 53
4.6 Acetaldehyde Detections 54
4.7 Ethylene Oxide Detections 55
4.8 Vinyl Alcohol Detections 55
4.9 Trans-Ethanol Detections 56
4.10 Gauche-Ethanol Detections 57
4.11 Dimethyl Ether Detections 57
4.12 Methyl Formate Detections 58
4.13 Glycolaldehyde Detections 59
4.14 Acetone Detections 60
4.15 Rotation Diagrams of Sublimated Products 62
4.16 Laboratory Spectra Compared to HIFI Survey of Orion-KL 67
4.17 Abundance Ratios of Orion-KL Compared to Laboratory Results . . . 70
4.18 Abundance Ratios of Hot Cores Compared to Laboratory Results . . . 71
4.19 Abundance Ratios of Comets Compared to Laboratory Results 72

5.1 H_2O Vapor Photolysis 83
5.2 UV Photodesorption of H_2O 83
5.3 UV Photodesorption of CH_3OH: Thin Ice Sample 85
5.4 UV Photodesorption of CH_3OH: Thick Ice Sample 86
5.5 UV Photodesorption of H_2 87
5.6 IR Spectra of Thin and Thick CO Ice Samples 87
5.7 UV Photolysis of CO Ice 88

5.8 UV Photodesorption of CO 89

List of Tables

2.1 Millimeter and Submillimeter Spectrometer Detection Limits 18

3.1 An overview of the thermal desorption kinetic parameters of previous H_2O ice studies. 31

4.1 IR Assignment of UV-Photolyzed CH_3OH Ice Sample (12 K) 50

4.2 Summary of Rotation Diagram Analyses Results 65

A.1 Submillimeter Spectral Assignment from 806500 to 812890 MHz . . . 97

A.2 Rotation Diagram Parameters 98

List of Abbreviations

COM	**C**omplex **O**rganic **M**olecule
EI-MS	**E**lectron **I**onization **M**ass **S**pectrometry
FTIR	**F**ourier **T**ransform **I**nfra**R**ed
HOPG	**H**ighly **O**riented **P**yrolytic **G**raphite
ISM	**I**nter**S**tellar **M**edium
LOD	**L**imit **O**f **D**etection
MDHL	**M**icrowave-**D**ischarge **H**ydrogen-flow **L**amp
mm/submm	**M**illimeter/**S**ubmillimeter
NASA	**N**ational **A**eronautics **S**pace **A**dministration
GSFC	**G**oddard **S**pace **F**light **C**enter
PID	**P**roportional-**I**ntegral-**D**erivative
PSD	**P**hase-**S**ensitive **D**etection
RAIRS	**R**eflection **A**bsorption **I**nfra**R**ed **S**pectroscopy
SNR	**S**ignal-to-**N**oise **R**atio
SubLIME	**Sub**limation of **L**aboratory **I**ces **M**illimeter/submillimeter **E**xperiment
TPD	**T**emperature **P**rogrammed **D**esorption
UHV	**U**tra**H**igh **V**acuum
UV	**U**ltra**V**iolet

Chapter 1

Introduction

1.1 Introduction to Astrochemistry

Space is an extremely harsh environment with extraordinary low pressures, intense radiation fields, and a range of temperature extremes from near absolute zero to thousands of Kelvin. Because of this, it was once thought that most of the matter could only exist in the form of atoms and dust grains–not individual molecules. This was disproven in 1937 when the first interstellar molecule was detected from a single emission line of the CH molecule (Swings et al., 1937). Three years later, the CH detection was confirmed by McKellar (1940) who identified several more emission lines of CH and additional emission lines for the CN molecule, proving that molecules do exist in the interstellar medium (ISM), despite the high radiation and cold conditions. Since then, hundreds of molecules have been detected in the ISM ranging in size and complexity including radicals (e.g., MgCN (Ziurys et al., 1995) and C_7H (Guélin et al., 1997)), ions (e.g., C_3N^- (2008) and HCO^+ (Buhl et al., 1970; Klemperer, 1970; Woods et al., 1975)), polycyclic aromatic hydrocarbons (e.g., c-C_9H_8 (Burkhardt et al., 2021)), fullerenes (C_{60} (Cami et al., 2010)), molecules with a chiral center (CH_3CHCH_2O (McGuire et al., 2016)), and prebiotic organics (e.g., NH_2CH_2CN (Belloche et al., 2008) and NH_2CONH_2 (Jimenez-Serra et al., 2020)). Consequently, the interdisciplanry field of astrochemistry was developed to examine the increasingly rich chemistry of space.

The astrochemistry community strives to quantitatively determine the cycle of matter in the universe from a chemical perspective. From an astrophysical perspective, the cycle of matter can be described by the stages of star and planet formation

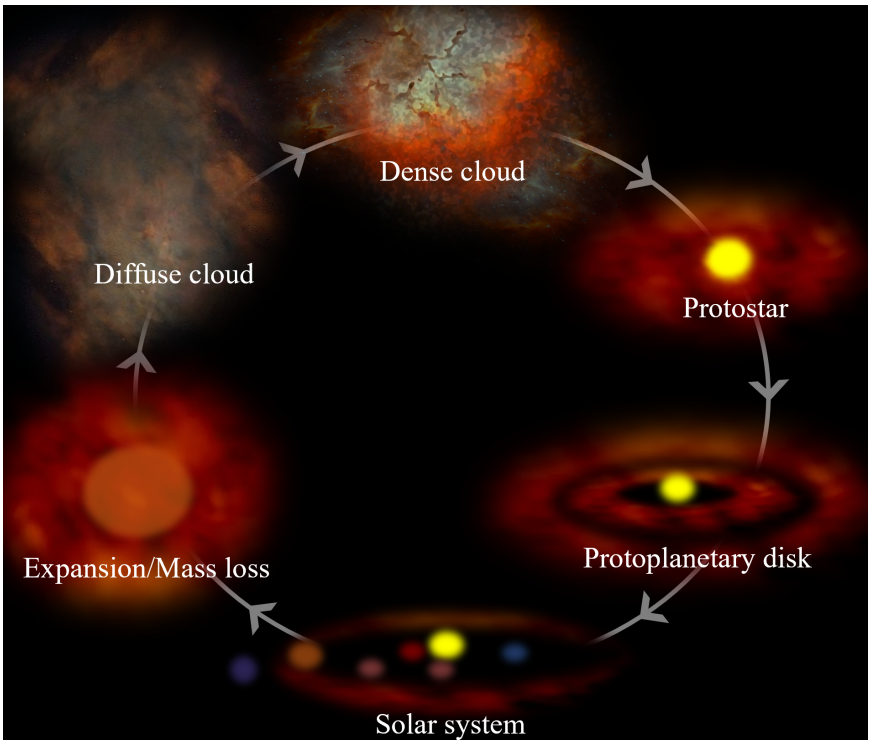

FIGURE 1.1: The stages of star and planetary system formation and destruction.

(Figure 1.1). In general, the prestellar stages consist of the diffuse cloud, dense cloud, and protostar stages which eventually transform to a protoplanetary disk followed by a planetary system. Eventually the star dies, expanding material into the ISM, and the cycle starts over. Therefore, the matter of the universe is constantly being altered, recycled, and transported. In fact, presolar grains (i.e., grains that formed before the Sun) have been found in primitive meteorites that were delivered to Earth (Haenecour et al., 2016; Nittler et al., 2018; Nittler et al., 2020; Pravdivtseva et al., 2020; Zinner, 1998) providing sufficient evidence that matter is recycled and transported.

In astrochemistry, the matter in space is broken into three categories: gas, dust, and ice. Dust consists of refractory compounds (e.g., graphite, diamond, and silicates) and ice consists of volatile compounds (e.g., H_2O, CO, NH_3, and CH_3OH) in the solid phase. The physical and chemical alteration of these molecules is dictated by the temperature and other sources of energy (e.g., UV photons and cosmic rays) that penetrate the region where they exist. For example, in our solar system the objects closest to the Sun are composed of mostly dense refractory compounds (i.e.,

the rocky planets) and volatile compounds exist in the outer solar system (i.e., gas giants, icy planets, and comets) where the temperature is much colder. Objects in the outer solar system also experience less radiation from the Sun and are theorized to house "pristine" molecules that were preserved from the presolar stage. Furthermore, small bodies such as asteroids and comets can transport volatiles across the solar system and thus are a potential delivery mechanism for water and other important molecules for prebiotic chemistry on Earth.

1.1.1 Cosmic Ice Chemistry

Volatile chemicals across the universe play an essential role in the formation of important prebiotic molecules such as amino acids, sugars, and nucleobases. In the extremely cold conditions of space, volatile chemicals solidify to form ices composed of not only water, but small organic molecules and nitrogen bearing species including key ingredients for biochemistry: C, N, O, H. These ices exist in cold regions such as ice-coated dust grains in dense interstellar clouds, cold planetary surfaces like the polar ice caps of Mars, on the surface of Ocean Worlds such as Europa, Titan, and Enceledus, and in small bodies such as comets and asteroids. Chemical reactions in cosmic ices are driven by space weathering processes such as those depicted in Figure 1.2. These processes also drive chemical species to be sputtered or sublimated to the gas phase where they then contribute to the gas-phase composition and abundances of the matter that surrounds the icy object. When ice surface chemistry is not considered in chemical models of star- and planet-forming regions the column densities of organic molecules are severely underestimated (Herbst, 2017; Wakelam et al., 2015). Even when the models include gas-grain processes such as ice-surface reaction mechanisms, photodesorption, and cosmic-ray driven reaction mechanisms occurring deeper in the ice mantle, the abundances of some molecules are still unexplained (Abplanalp et al., 2016; Herbst, 2017). Therefore, there are connections between ice and gas chemistry (i.e., gas-grain interactions) that are not fully understood. This connection is critical for explaining discrepancies between computational models of star-forming regions and the observed chemical abundances of the ISM. It also plays a role in explaining the gas-phase abundances of cometary coma and planetary atmospheres. The work herein explored the connection between ice

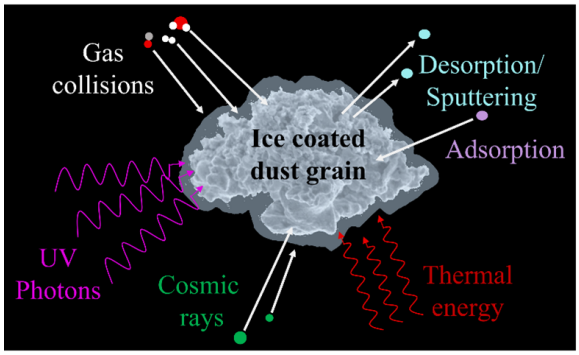

FIGURE 1.2: Space weathering processes that drive chemical and physical changes on cosmic ice surfaces (e.g., an ice-coated dust grain).

surface chemistry and gases that sublimate/desorb from the ice surface due to heat and UV photons.

Laboratory Cosmic Ice Chemistry

Laboratory experiments have been conducted for decades to study cosmic ice chemistry by recreating interstellar, cometary, and planetary conditions in a laboratory setting (Carrascosa et al., 2021b; Gerakines et al., 2004; Greenberg et al., 1972; Hudson et al., 2017; Moore et al., 1983; Schutte et al., 1993). These experiments commonly use ultra-high and high-vacuum chambers to simulate the low density and cold conditions of interstellar clouds, icy planetary bodies, and/or comets to study the solid-phase chemistry driven by energetic processing from particles (e.g., protons and electrons), UV photons, and/or heat. The chemistry examined ranges from the formation of small molecules (e.g. H_2O, CH_4, NH_3) (Dulieu et al., 2010; Fedoseev et al., 2014; Qasim et al., 2020) to larger molecules commonly referred to as complex organic molecules (COMs; molecules with 6+ atoms) (2021; Lee et al., 2009; Meinert et al., 2016). Previous studies have also investigated the sublimation of COMs after low temperature formation in cosmic ice analogs via heat (Abou Mrad et al., 2016; Butscher et al., 2016; Schneider et al., 2019) and UV photodesorption (Bertin et al., 2016; Öberg et al., 2009a; Paardekooper et al., 2016b). Varying results have been produced from these studies. For example, Öberg et al. (2009a) reported the UV photodesorption yield of methanol as $2.1(\pm1.0) \times 10^{-3}$ molecules photon^{-1} and it was later determined by Bertin et al. (2016) that the photodesorption yield of methanol

is on the order of 10^{-5} molecules photon^{-1}, and the photofragments of methanol desorb in much higher yields than the intact molecule. These experiments are further complicated by the fact that it becomes difficult to calculate the concentrations of each unique product due to analytical techniques having overlapping signals. The analytical techniques traditionally implemented to monitor chemical changes during energetic processing are Fourier Transform infrared (FTIR) spectroscopy to analyze the solid ice sample, and electron ionization mass spectrometry (EI-MS) to analyze sublimated gases (Allamandola et al., 1988; Cruz-Diaz et al., 2016; Greenberg et al., 1972; Hudson et al., 1991; Öberg et al., 2009b). These techniques are essential for identifying new molecules from processed ice samples because they are very sensitive, but they are limited by functional group overlaps in the IR spectra and mass fragment overlaps in the mass spectra making the unique identification of COMs very challenging and, in some cases, impossible. Thus, as the field progresses, the developments of new structure-specific analytical techniques are required.

The work described herein involved the development of a laboratory technique to reveal new information about cosmic ice chemistry. The Sublimation of Laboratory Ices Millimeter/submillimeter Experiment (SubLIME) combines millimeter and submillimeter (mm/submm) spectroscopy, infrared spectroscopy, and mass spectrometry to explore the connection between ice surface chemistry and the gases that surround icy surfaces in space by studying the intricate details of sublimation. SubLIME focuses on the chemistry driven by ultraviolet (UV) photons, how those chemical reactions differ under temperature variations, and how UV photons and heat affect the sublimation process.

1.1.2 Rotational Spectroscopy as a Tool for Laboratory Astrochemistry

SubLIME is the first laboratory technique to utilize millimeter and submillimeter spectroscopy (i.e., rotational spectroscopy) for the chemical analysis of species that sublimate from energetically processed ice samples. Rotational spectroscopy is a powerful technique for uniquely identifying components of complex gas mixtures because it is very structure-specific. Rotation of a three-dimensional molecule around the three principal axes (a, b, and c) gives rise to unique moments of inertia that depend on the masses of the atoms making up the molecule and the distance from the

rotating atoms to the center of mass of the molecule. This results in quantized rotational energies levels that lead to unique structure-specific spectral fingerprints. For many molecules, the effects of centrifugal distortion, internal rotation, and hyperfine splitting provide further structural information (Gordy et al., 1984; Townes et al., 1975; Wollrab, 1967). The structure-specificity of rotational spectroscopy makes it a widely used tool in astrochemistry and, in fact, mm/submm spectroscopy is the most widely used technique for probing the gas-phase compositions of the ISM (Crockett et al., 2010; Widicus Weaver et al., 2017; Willis et al., 2020), cometary coma (Cochran et al., 2015; Roth et al., 2021), and planetary atmospheres (Moreno et al., 2017; Parks et al., 2021). The three main benefits that mm/submm spectroscopy provides for laboratory cosmic ice experiments are (1) the direct comparison of laboratory spectra with mm/submm spectra collected by telescopes; (2) the unambiguous identification of sublimated products including structural isomers, conformers, and isotopologues; and (3) quantification of uniquely identified molecules to compare to astrochemical models of the ISM and planetary atmospheres.

1.2 Dissertation Overview

This dissertation presents the details of the SubLIME setup, proof-of-concept results for the millimeter and submillimeter spectroscopic detection of sublimated ice samples, the results of experiments that examined the products of UV-photolyzed methanol ice, and preliminary work toward detecting UV-photodesorbed products. The dissertation is organized as follows:

Chapter 2: The experimental methods are described.

Chapter 3: Proof-of-concept experiments are presented to demonstrate that millimeter/submillimeter spectroscopy can be used to detect sublimated ice samples of water (H_2 and D_2O) and methanol (CH_3OH).

Chapter 4: The results of experiments are presented that used submillimeter spectroscopy as a structure-specific technique to uniquely identify and quantify sublimated products of a methanol (CH_3OH) ice sample processed with UV photons and heat. The abundance ratios of organic products were compared to those detected in hot cores and comets.

Chapter 5: The results of UV photodesorption experiments are presented and the limitations of direct-absorption millimeter/submillimeter spectroscopy are discussed.
Chapter 6: Conclusions of the dissertation are presented along with the motivations for future studies.

Chapter 2

Experimental Methods

2.1 SubLIME Setup Descriptions

The SubLIME setup was designed to study the chemical and physical changes of cosmic ice analogs driven by UV photons by combining three analytical techniques: millimeter and submillimeter (mm/submm) spectroscopy, infrared spectroscopy, and mass spectrometry. The results presented herein were collected in two different vacuum chambers and using three different experimental setups. The first chamber was built at Emory University and the second chamber was built at NASA Goddard Space Flight Center (GSFC). The first experimental setup was built by previous students at Emory University prior to 2017, and the setup went through an in-depth rebuild in 2018 to address some limitations and to implement several new experimental techniques. The second chamber at NASA GSFC was designed from the basis of the rebuilt Emory University chamber with some additional improvements. The original Emory University chamber is described in 2.1.1 and the details of the chamber rebuild are described Section 2.1.2. Lastly, a description of the NASA GSFC setup can be found in Section 2.1.3.

2.1.1 Emory University Experimental Setup 1

Figure 2.1 shows a detailed schematic of the chamber before it was rebuilt in 2018. The setup, which from here on will be referred to as experimental setup 1, consisted of a series of vacuum pumps and gauges, a cryostat, a direct-absorption mm/submm spectrometer, a UV photolysis lamp, and a gas-inlet valve. The base pressure of the vacuum chamber was $\sim 2.0 \times 10^{-7}$ Torr achieved by an Œrlikon Leybold TW90

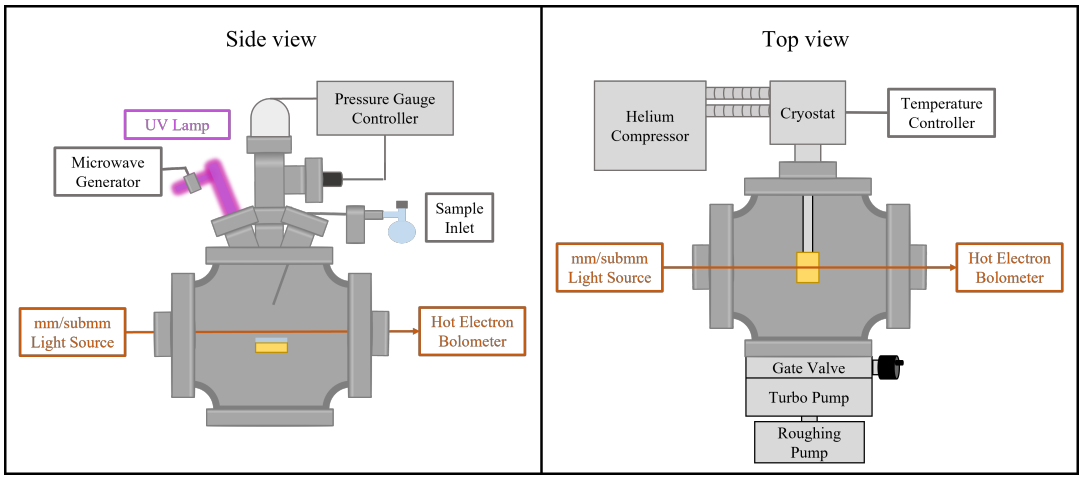

FIGURE 2.1: Schematic of the vacuum chamber before the 2018 rebuild (experimental setup 1). Ice samples were formed on a cold substrate depicted at the center of the vacuum chamber.

turbopump backed by an Edwards EM30 rotary vane pump. A pneumatic gate valve (High Vacuum Apparatus Mfg., Inc., 124-0600) was used to isolate the chamber from the pumps when needed. Ice samples were formed at the center of the vacuum chamber on a polished nickel substrate (Advanced Research Systems, Inc., SHNO-1B) attached to the cold arm of a closed-cycle helium cryostat (APD Cryogenics 256844D1, expander model DE-202B) connected to a helium compressor (APD Cryogenics, HC-2).

The temperature of the substrate was controlled with a PID temperature controller (Lake Shore Cryotronics, 330) and was monitored via a thermocouple sensor (Lake Shore Cryotronics). The base temperature of the substrate was ∼30 K. A 36 Ω metallized heater (Lake Shore Cryotronics), located on the tip of the cold arm, was used to heat the substrate from ∼30 to 300 K. A multi-port flange (MDC Precision Products LLC, 409009) was connected to the top port of the vacuum chamber and provided three 2.75-inch ConFlat® (CF) ports where the UV photolysis lamp (Opthos Inc., LR-H), sample inlet gas line, and pressure gauges were secured. Sapphire viewports (Kurt J. Lesker Company, VPZL-275S) located on either side of the chamber were the entrance and exit ports for the light beam of the mm/submm spectrometer. The mm/submm light beam passed straight through the chamber ∼2 cm above the sample to detect products sublimated from an ice sample upon heating and/or UV photolysis. Some preliminary results were collected with this setup and

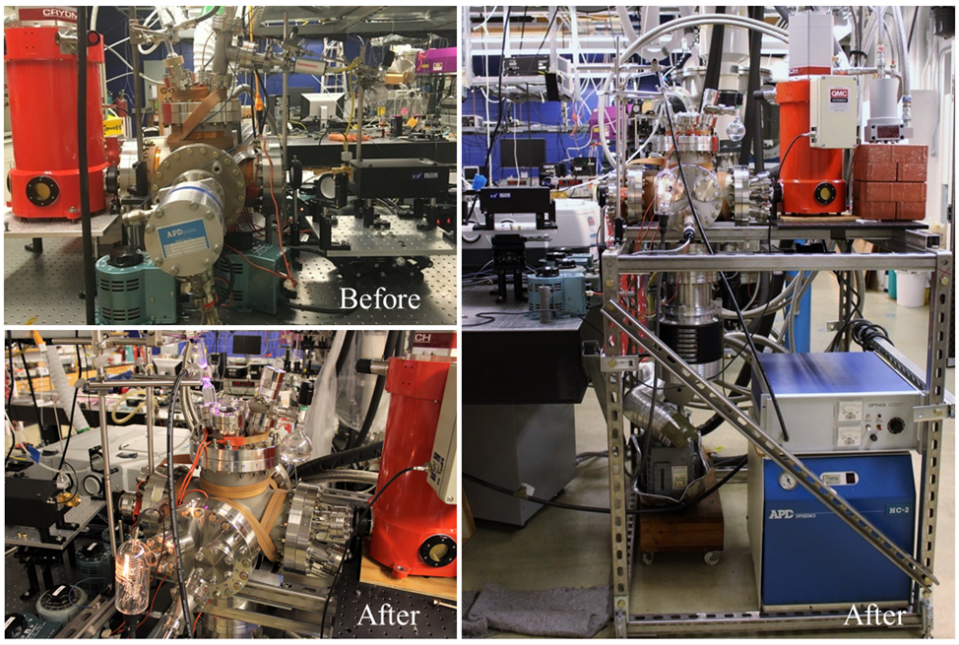

FIGURE 2.2: The top left image shows experimental setup 1 before reconstruction, the bottom left image shows experimental setup 2 after reconstruction, and the right image shows the entire experimental setup 2 including the new housing structure.

are discussed in Chapter 3.

2.1.2 Emory University Experimental Setup 2

A new design of the SubLIME setup was constructed in late 2018 to improve experimental reproducibility and to incorporate several new analytical techniques. Figure 2.2 shows pictures of the setup before and after the vacuum chamber was rebuilt and Figure 2.3 shows a detailed schematic of the rebuilt setup, referred to henceforth as experimental setup 2.

First, a new support structure was built and the setup was removed from the optics table to allow access to the bottom 8-inch CF port and to improve the support and stability of the overall setup. Next, the vacuum level was increased to ultrahigh vacuum (UHV) conditions to decrease contamination and to improve the pressure stability during static experiments when the vacuum chamber was isolated from the pumps. The base pressure of the vacuum chamber was decreased to $\sim 1.0 \times 10^{-9}$ Torr by replacing all vacuum connections with UHV CF components. Next, several new analytical techniques were incorporated to the setup including

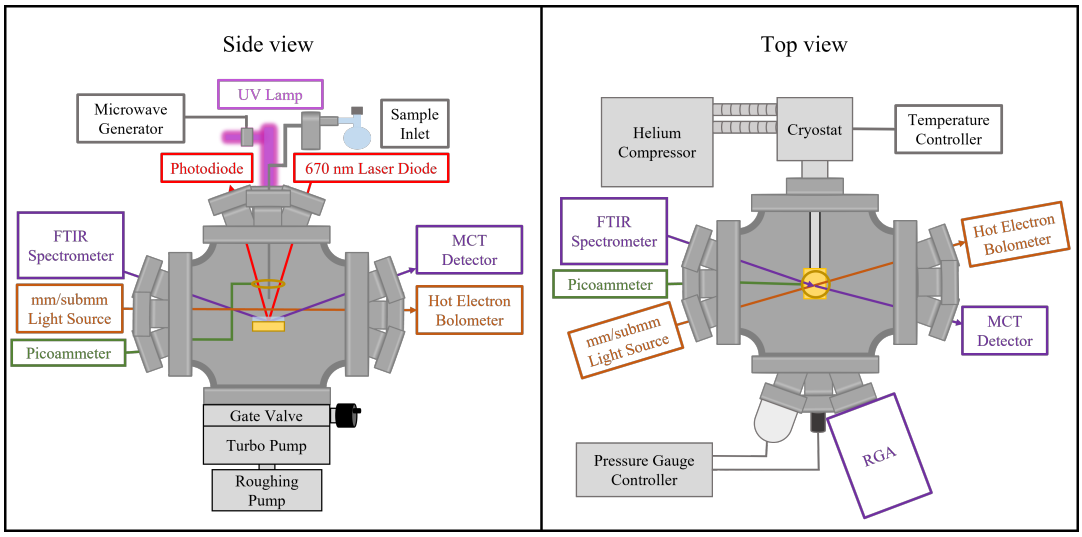

FIGURE 2.3: Schematic of experimental setup 2 after the 2018 rebuild. Ice samples are formed on a cold substrate depicted at the center of the vacuum chamber. This setup was originally located at Emory University and has now been relocated to the University of Wisconsin-Madison.

(1) a Fourier-Transform Infrared (FTIR) spectrometer for spectroscopic analysis of solid-phase ice samples, (2) a quadrupole mass spectrometer for gas-phase analysis, (3) a laser interferometer for monitoring sample deposition and sublimation, and (4) a photoelectron technique to measure UV flux of the photolysis lamp. Lastly, several components were replaced or updated. The static UV photolysis lamp was replaced with a microwave-discharge hydrogen-flow lamp to increase the UV photon flux at the substrate. Refer to Section 2.3.1 for the details of the UV lamp. The sapphire viewports were replaced with z-cut quartz viewports to increase the spectral power of the mm/submm spectrometer. Figure 2.4 shows a comparison of the spectral power from 470-700 GHz for the z-cut quartz viewports and the sapphire viewports and shows that the z-cut quartz viewports transmit more submillimeter light than the sapphire viewports. The nickel plated substrate was replaced with a gold plated substrate (Advanced Research Systems, Inc., SHNO-1B) for preforming reflection absorption infrared spectroscopy (RAIRS) of the ice samples. The thermocouple temperature sensor was replaced with a silicone diode sensor (Scientific Instruments, SI-410) and the temperature controller was upgraded to a Scientific Instruments 9700 temperature controller for higher accuracy temperature readout and control. The pressure gauge controller was upgraded to an Agilent Technologies

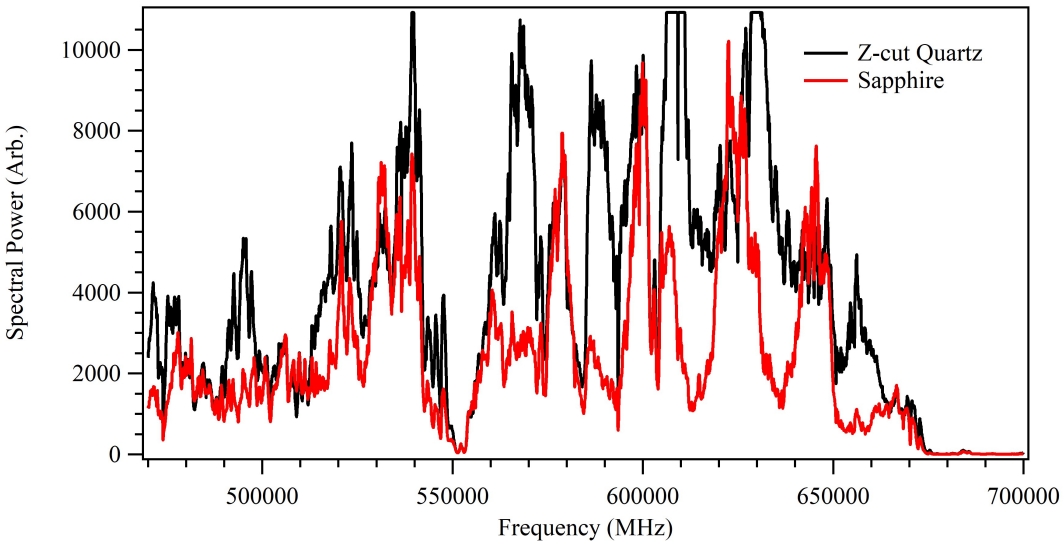

FIGURE 2.4: Comparison of the spectral power of the mm/submm light source through sapphire viewports (red) and z-cut quartz viewports (black) from 470-700 GHz (0.638-0.428 mm).

XGS-600 gauge controller. The pneumatic gate valve was replaced with a manual gate valve (MDC Precision Products LLC, GV-6000V) for better control when pumping out the vacuum chamber after static experiments. Lastly, the sample inlet line was rebuilt with a new UHV high-precision gas dosing valve (Pfeiffer Vacuum Inc., UDV-046), multiple sample attachments for more than one analyte, and a pumping line separate from the vacuum chamber.[1]

2.1.3 NASA GSFC Experimental Setup 3

A new version of the SubLIME setup was recently designed and built at NASA GSFC and was based on experimental setup 2 originally located at Emory University and is now located at the University of Wisconsin-Madison. This setup is referred to as experimental setup 3 henceforth.

The experiment takes place in a custom designed spherical stainless steel vacuum chamber (diameter = 12 inches, NorCal Products) and a schematic is shown in 2.5. A turbopump (Agilent Technologies, TV301 Navigator) located on the bottom 8-inch CF port achieves a base pressure of $\sim 3.0 \times 10^{-9}$ Torr and is backed by a three-phase rotary vane pump (Edwards, EM30). A closed-cycle-helium cryostat

[1] In experimental setup 1, the sample line was pumped through the vacuum chamber.

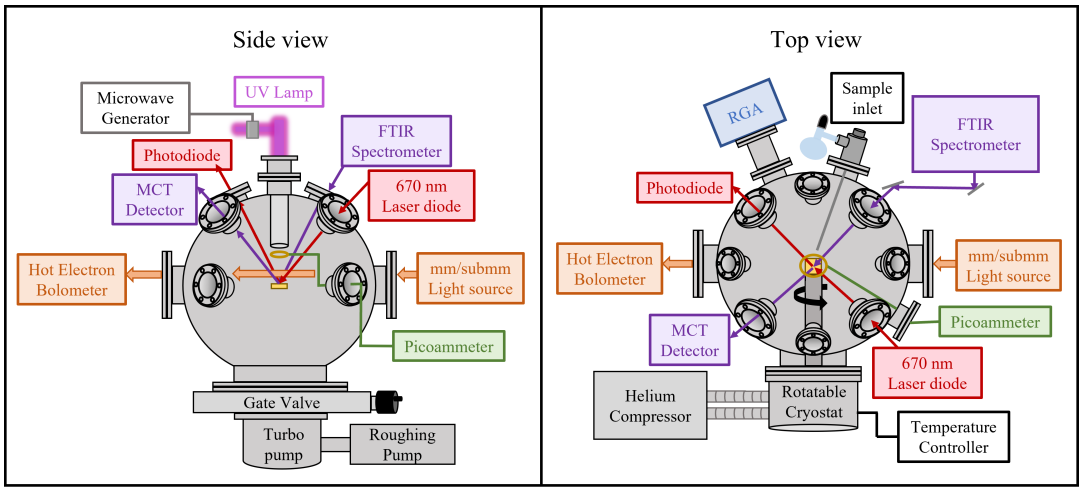

FIGURE 2.5: Schematic of experimental setup 3 located at NASA GSFC. Ice samples are formed on a cold substrate depicted at the center of the vacuum chamber.

(Advanced Research Systems, Inc., expander model DE210AB) is attached to a 6-inch CF port located on the front side of the chamber and connects to a helium compressor (Advanced Research Systems, Inc., ARS-10HW). Ice samples are formed by vapor-deposition on a reflective gold substrate (Advanced Research Systems, Inc., SHNO-1B) attached to the cold arm of the cryostat positioned at the center of the chamber and achieves a base temperature of ∼6 K. The cryostat and sample substrate can be fully rotated 360° while remaining under UHV conditions by a differentially pumped rotary seal (Thermionics Laboratory, Inc., RNN 400-FA). The sample vapor enters the chamber through a high-precision gas-dosing valve (Pfeiffer Vacuum, PF I52 035) and a capillary tube (Pfeiffer Vacuum, PT 418 976-T) that releases the vapor into the vacuum chamber ∼1 inch above the cold substrate. The ice sample thickness and deposition rate are monitored via the same laser interferometry technique used in experimental setup 2. This technique is described in Section 2.2.4. The temperature of the sample can be varied from ∼6 - 300 K using a temperature controller (Scientific Instruments, 9700) that measures the temperature with two silicon diodes (Lake Shore Cryotronics, DT-670B-SD) and heats the sample with a 50 Ω metallized heater (Lake Shore Cryotronics). The first temperature sensor is located on the tip of the cold arm and the readout is used to control the temperature of the sample. The second sensor is located on the sample substrate and the readout gives the sample temperature. A microwave-discharge hydrogen-flow lamp is connected

to the top port of the vacuum chamber to expose the ice sample to UV photons of similar energy as the solar and interstellar UV fields. The flux of the UV photolysis lamp is measured by the same photoelectron technique used in experimental setup 2. For more details of the UV photolysis lamp refer to Section 2.3.1. RAIRS spectra are collected of the ice sample with a FTIR spectrometer. See Section 2.2.2 for details about the IR technique. A custom designed direct-absorption mm/submm spectrometer with frequency ranges of 83-1100 GHz, 1.8-1.9 THz, and 2.5-2.6 THz is used to detect products that sublimate from the ice sample. The mm/submm spectrometer is described in detail in Section 2.2.1. Lastly, a quadrupole mass spectrometer is used in tandem for gas-phase analysis, and is described in Section 2.2.3. The combination of mm/submm spectroscopy and mass spectrometry allow for the unambiguous identification of the composition of complex gas mixtures that sublimate from processed ice samples.

2.2 Analytical Techniques

2.2.1 Millimeter/submillimeter Spectroscopy

The mm/submm spectroscopic technique used for these studies measures the direct absorption signals of pure rotational transitions of molecules and a detailed schematic of the spectrometer is shown in Figure 2.6. The spectrometer was custom designed and has frequency coverage of 70-1100 GHz, 1.8-1.9 THz, and 2.5-2.6 THz (wavelength coverage: 6.00-0.27 mm, 0.167-0.158 mm, and 0.120-0.115 mm). The mm/submm light source consists of a microwave analog signal generator (Keysight Technologies, E82-57D PSG; 250 kHz to 40 GHz), a mini modular signal generator extender (i.e., mm-wave multiplier) (Virginia Diodes, Inc., WR9.0M-SGX-M (85-125 GHz) and WR10X3 (70-110 GHz)), and Schottky diode frequency multipliers (Virginia Diodes, Inc., WR4.3X2, WR2.2X2, WR1.5X3, WR2.8X3, WR1.0X3; 170-1100 GHz). See Figure 2.7 for the specific frequency ranges of the Schottky diode combinations for the WR9.0 base unit.

For the mm/submm spectra presented herein the microwave signal from the Keysight signal generator was frequency modulated by a sine wave having a 0.2 kHz frequency and a modulation depth of 75 kHz. The signal is multiplied to

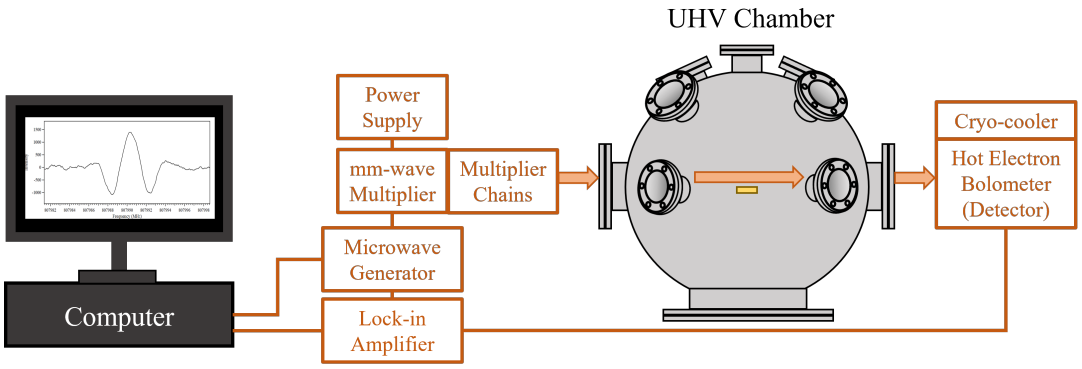

FIGURE 2.6: Schematic of the mm/submm spectrometer comprised of a microwave signal generator, mm-wave multiplier, multiplier chains (Schottky diodes), lock-in amplifier, and a cryo-cooled hot-electron bolometer.

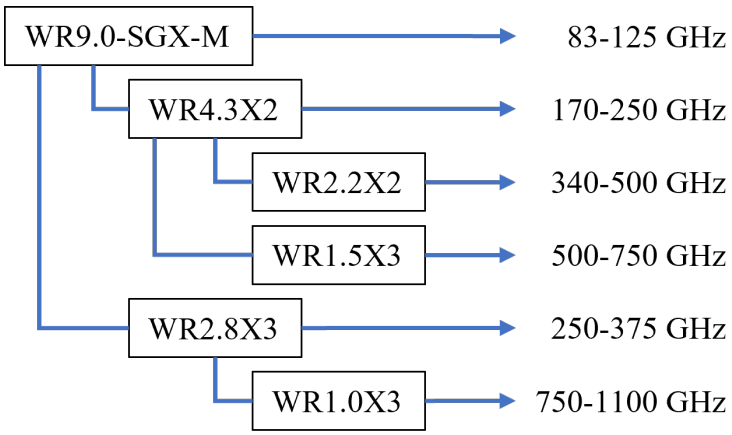

FIGURE 2.7: Schottky diode (i.e., multiplier chain) combinations and corresponding frequency outputs for the millimeter and submillimeter light source from 83-1100 GHz. Information from Virginia Diodes, Inc.

mm/submm wavelengths when passed through the mm-wave multiplier and the Schottky diode(s) (i.e., multiplier chains). The mm/submm light beam passed through the gas sample in the vacuum chamber ~2 cm above the ice sample. Next, the signal was detected by a hot-electron bolometer (QMC Instruments, QNbB/PTC) with a Niobium semiconductor cryo-cooled by an expander (Cryomech, Inc., PT803). The expander was supplied by a closed-cycle helium compressor (Cryomech, Inc.,

CP830), and the signal was demodulated via second harmonic detection with a lock-in amplifier (Stanford Research, SR830 DSP). The lock-in amplifier removes background spectral noise by destructively interfering with any signals that do not resonate with the second-harmonic frequency of the modulated signal. This phase-sensitive detection (PSD) technique results in second-derivative Gaussian line shapes as shown on the computer screen in Figure 2.6. A low-pass filter located at the PSD output removes the unwanted noise signals and the low-pass filter bandwidth was set by a time constant of 10 ms. Spectral scans were collected with 0.1 MHz resolution and the number of spectral averages varied based on the detection limit of the analyte and the time constraints of the individual studies.

Submillimeter Limits of Detection

The limit of detection (LOD) is an instrumental detection limit defined herein as the lowest gas density at which the spectrometer can detect specific rotational transitions with a signal-to-noise ratio (SNR) of at least 3; therefore, the LOD depends on the intensity of the specific transition probed and the specific experimental setup used for the measurement. In general, when determining the LOD for different analytes, five rotational transitions were tested by slowly increasing the analyte partial pressure using the high-precision gas-dosing valve and collecting mm/submm spectra at each pressure step. The rotational transition with the lowest SNR out of the five was used to determine the LOD. Knowing the LOD is important for calculating the plausibility of detecting specific analytes when performing UV-photolysis experiments.

An example of the LOD measurements for water (H_2O) at 556935.99 MHz are shown in Figure 2.8. For these measurements, the density of H_2O vapor was slowly increased in the vacuum chamber until a SNR of >3 was measured. Table 2.1 lists several LODs measured for all three experimental setups using the lock-in PSD technique. Furthermore, the feasibility of implementing a fast-sweep detection technique was explored and the fast-sweep detection limits of methanol (CH_3OH) and carbon monoxide (CO) are reported in Table 2.1.

The H_2O and CH_3OH LOD values in Table 2.1 can be used to compare the three experimental setups. The LOD of H_2O and CH_3OH were decreased by an order

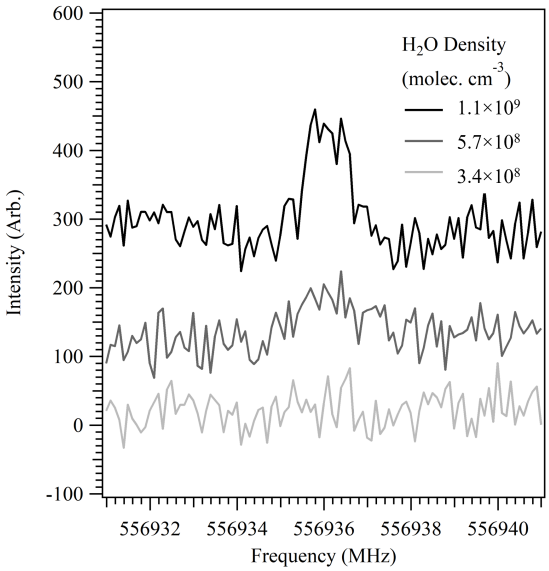

FIGURE 2.8: Submm spectra of the $1_{1,0} \leftarrow 1_{0,1}$ rotational transition of H_2O at 556935.99 MHz to determine the LOD. The spectra were collected while slowly increasing the density of H_2O vapor in the vacuum chamber. Each spectrum contains 30 spectral averages.

of magnitude after the 2018 rebuild. Furthermore, The LOD was remeasured for CH_3OH before (Table 2.1) and after the sapphire viewports were replaced with z-cut quartz viewports to determine if the LOD had improved. The LOD of CH_3OH measured with 30 spectral averages at 627170.48 MHz was 2.9×10^{10} molecules cm^{-3} with a SNR of 4.3.

The advantage of fast-sweep detection is the fast data acquisition speed which allows for thousands of spectral scans to be collected and averaged together. As demonstrated by the LODs of CH_3OH and CO in Table 2.1, lock-in PSD technique is more sensitive than fast-sweep detection. Another downside of fast-sweep detection is that the center frequencies of the transitions can appear shifted from their true value. For example, Figure 2.9 shows the fast-sweep detection of a CH_3OH transition with a center frequency of 627170.48 MHz, but the peak of the absorption signal was located at ~627171.24 MHz. The frequency shift becomes larger as the bandwidth of the scan is increased making the spectral assignment of complex mixtures challenging. The fast-sweep technique was only used for the LOD measurements reported in Table 2.1. The lock-in PSD technique was more sensitive and was used for all other experiments presented herein.

TABLE 2.1: Millimeter/submillimeter spectroscopic limits of detection (LOD)

Analyte	Setup	LOD (molecules cm^{-3})	Frequency (MHz)	Spectral Averages	SNR
H_2O	1	2.1×10^{10}	556935.99	30	4.3
H_2O	2	1.1×10^{9}	556935.99	30	5.6
H_2O	3	1.4×10^{9}	556935.99	30	3.4
D_2O	1	1.7×10^{9}	607349.44	30	3.8
CO	2	$>2.9\times10^{11}$	576267.93	60	2.6
CO	2*	1.3×10^{12}	576267.93	10000	5.5
CO	3	1.5×10^{11}	691473.08	30	4.0
CH_3OH	1	3.2×10^{11}	616979.87	10	3.0
CH_3OH	2	3.1×10^{10}	627170.48	30	8.3
CH_3OH	2*	1.9×10^{11}	627170.48	10000	3.1
CH_3OH	3	4.4×10^{10}	627170.48	30	3.3

*Fast-sweep detection

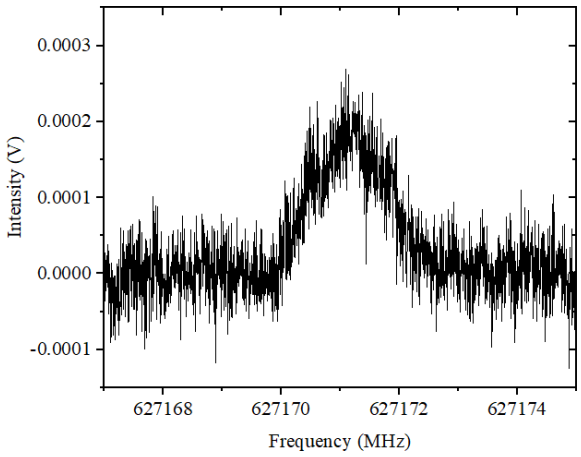

FIGURE 2.9: Fast-sweet detection of the $13_{-1,13} \leftarrow 12_{-1,12}$ rotational transition of CH_3OH centered at 627170.48 MHz to determine the LOD. The detected transition was slightly shifted in frequency to 627171.24 MHz due to the fast-sweep technique.

Optical Filter Tests

Optical bandpass filters can be used to reduce unwanted background noise detected in the mm/submm spectra and to improve the SNR. Several tests were conducted to assess the level of SNR improvement when using a metal mesh bandpass filter (Virginia Diodes, Inc.). These tests were conducted in the 600-700 GHz spectral range with a bandpass filter centered at 630 GHz and a bandwidth of 22.3%. Refer to Porterfield et al. (1994) for a description of the optical filter design.

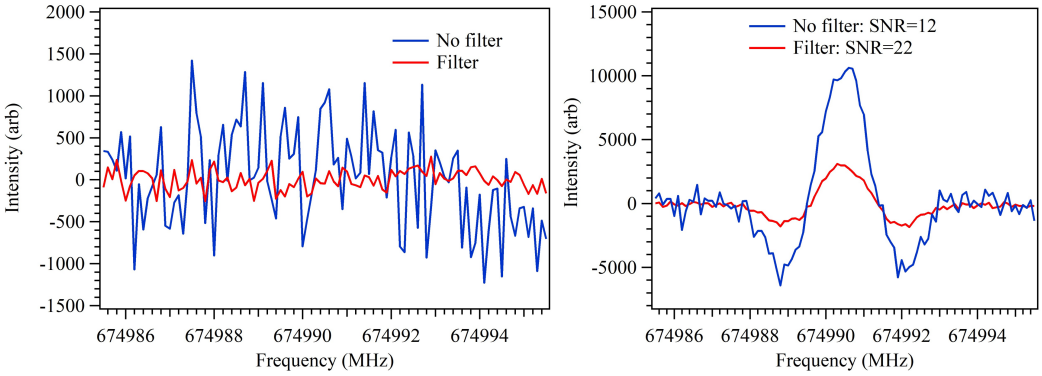

FIGURE 2.10: Left: Noise level comparison of spectra taken with no filter (blue) vs. filter (red). Standard deviation of the noise decreased from 592 to 119 when the filter was used. Right: Methanol SNR comparison of spectra taken with no filter (blue) vs. filter (red). The SNR increased from 12 to 22 when the filter was used. 15 spectral averages were collected for the four scans shown.

Figure 2.10 shows the noise reduction when the signal was passed through the optical filter compared to when no filter was used (left panel) and a comparison of the SNR of a methanol (CH_3OH) transition centered at 674.99 GHz with the filter and without (right panel). The standard deviation of the background noise level at these frequencies was decreased from 592 (no filter) to 119 (filter) and the SNR of the methanol signal increased from 12 (no filter) to 22 (filter). More filter vs. no filter comparisons were conducted for varying frequency ranges and transition intensities. In conclusion, the optical filter greatly improved the SNR when a low number of spectral averages were collected. Once the number of spectral averages surpassed $\sim$20 the filter only slightly improved the SNR. Therefore, the use of optical bandpass filters, such as a metal mesh filter, significantly improves SNR when the collection of a large number of spectral averages is not practical (e.g., broadband scans with frequency ranges of >50 MHz).

2.2.2 Infrared Spectroscopy

The experiment utilized FTIR spectroscopy to probe the chemical changes of an ice sample during energetic processing (i.e., heating and UV photolysis) via the RAIRS technique. The FTIR spectrometer (ThermoFisher Scientific, Nicolet™ iS50R) consists of a Polaris™ IR source, a step-scan and linear capable Vectra interferometer,

and an external mercury-cadmium-telluride (MCT) detector. The IR source emits radiation across 4000-500 cm^{-1} into the interferometer. The IR radiation exits the optical bench and is reflected and focused into the chamber by aluminum mirrors (Thorlabs, Inc., PF20-03-G01) and an off-axis parabolic mirror (Thorlabs, Inc., MPD399-M01). The focused IR light enters the vacuum chamber through a ZeSe viewport (Kurt J. Lesker Company, VPZL275UZC), travels through the ice sample, reflects on the gold sample substrate, exits the chamber via a second ZeSe viewport, and is reflected and focused into the liquid nitrogen cooled MCT detector by a second off-axis parabolic mirror (Thorlabs, Inc., MPD129-M01). The detector measures IR radiation over time and generates an interferogram. The signal is read by the computer and uses a Fast-Fourier transform to determine the intensities at each IR frequency that passed through the ice sample.

Molecules can be identified in the IR spectrum by their vibrational transitions, although many molecules have overlapping IR transitions due to possessing the same functional groups. The amount of IR overlaps increases as the composition of the ice sample becomes more complex and it becomes very challenging to distinguish each individual molecule in the ice sample. A remedy for the IR overlaps is to use the volatility of the molecule as a separation method. In other words, many molecules rapidly sublimate at different and specific temperatures and if the sublimation profiles are well characterized, then a slow sample warm up removes some of the IR features and molecules can be identified with more confidence. Although, again, as the composition becomes more complex the sublimation profiles can blend together and unique identification is still a challenge for many organic molecules. The coupling of a gas-phase analytical technique, such as mass spectrometry, is required to confirm the compositions of sublimated ice samples.

2.2.3 Mass Spectrometry

Mass spectrometry is commonly used in laboratory studies of cosmic ice chemistry and was incorporated to the setup for assisting the gas-phase analysis. Mass spectrometry is highly sensitive and is capable of quantifying gas-phase molecules even under UHV conditions ($< 10^{-8}$ Torr). It is also a useful tool for troubleshooting contamination and other vacuum issues. The mass spectrometer used in the

studies herein was a quadrupole residual gas analyzer (Stanford Research Systems, RGA300). In the mass spectrometer, molecules are ionized upon impact with electrons emitted from a hot filament. The molecular ion typically has a high internal energy that causes it to break into fragments and the fragments are separated in a quadrupole mass filter by their mass to charge ratio (m/z). The m/z of the parent ion is equal to the molecular mass of the compound. Mass spectra can be measured from 1 to 300 amu[2] with a resolution of 0.5 amu.

Mass spectrometry is highly useful for quantifying simple gas mixtures of molecules with different structural backbones, but when molecules of the same mass or very similar structures are present in a complex gas mixture, many times each individual component can not be uniquely quantified without a separation method such as chromatography, for example. In ice chemistry experiments, the volatility of the molecule can be used as a separation method, as previously mentioned in Section 2.2.2, but as the gas mixture becomes more complex the unique identification and quantification of all molecules present in the gas mixture becomes challenging due to the increasing amount of m/z overlaps in the spectra. SubLIME addresses this challenge by using IR spectroscopy, mass spectrometry, and the structure-specificity of pure rotational spectroscopy to unambiguously identify the components of the gas mixture, and is a highly complementary technique for the decades past of laboratory cosmic ice experiments.

2.2.4 Laser Interferometry

An interferometric technique (Tempelmeyer et al., 1968) was incorporated to the setup to measure ice sample thickness and deposition/sublimation rates. The ice sample thickness and deposition rate is monitored by a 670-nm red laser. The laser diode (Thorlabs, Inc., CPS670F) light enters the vacuum chamber through a fused silica window (Thorlabs, Inc., VPCH42-A), with a known incidence angle (experimental setup 2 = 29.4°; experimental setup 3 = 45°). The laser light beam reflects from the gold substrate, passes through a second fused-silica window, and is detected by a photodiode (Thorlabs, Inc., DET100A). As the ice sample thickens, the detected laser intensity oscillates due to constructive and destructive interference

[2] Atomic mass unit. 1 amu = 1.660540×10^{-27} kg

between the refracted and reflected light beams. The measured voltage creates an interference fringe pattern which is used to calculate the ice thickness by the Bragg equation:

$$d = \frac{m\lambda}{2\sqrt{n^2 - sin^2\theta}}, \tag{2.1}$$

where m is the number of oscillations, λ is the laser wavelength, n is the real part of the refractive index, and θ is the incidence angle of the laser. Figure 2.11 shows an example of ice deposition interference fringes measured during the formation of a water (H_2O) ice sample.

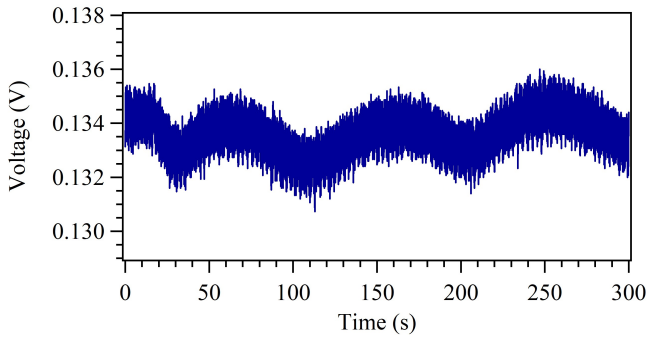

FIGURE 2.11: Ice deposition interference fringes measured during the deposition of a H_2O ice sample.

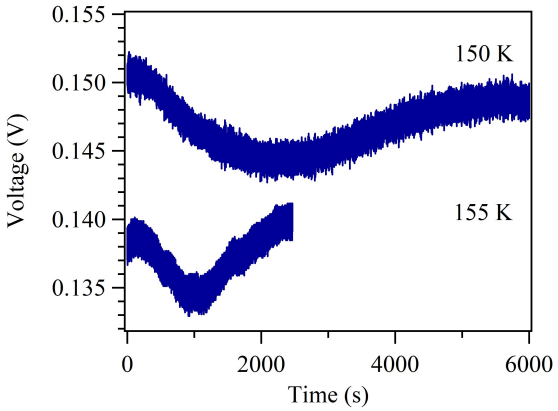

FIGURE 2.12: Ice sublimation interference fringes measured during the sublimation of a H_2O ice sample at 150 (top) and 155 K (bottom).

The technique can also be used to measure the ice deposition and sublimation rates. Figure 2.12 shows an example of interference fringes measured during the sublimation of a H_2O ice sample at 150 and 155 K, showing a significant rate increase

at 155 K. For more details about the thermal sublimation of H_2O ice sample refer to Chapter 3.

2.3 Energetic Processing of Ice Samples

2.3.1 UltraViolet (UV) Processing

The studies presented herein used a microwave-discharge hydrogen-flow lamp (MDHL) to simulate the UV field from the Sun and/or in an interstellar cloud. The photons entered the chamber through a MgF_2 viewport (Kurt J. Lesker Company, VPZL-275UMEU) and interact with the ice sample at the center of the vacuum chamber. In experimental designs 1 and 2, the lamp was positioned with an incidence angle of 13° at the surface of the ice sample. The lamp was constructed of quartz and had an F-type configuration. The microwave discharge was delivered to the lamp through an Evenson cavity powered by a microwave generator (Opthos Intrument Company, LLC, MPG-4 526). In the experimental design 3, the lamp was positioned perpendicular to the ice sample, had an F-type configuration, and was constructed of quartz. After the UV photons entered the chamber through the MgF_2 window, they traveled through a custom designed Pyrex waveguide (diameter = 1 inch, Kurt J. Lesker Company) to maximize the photon flux at the ice sample and to minimize photon collisions on the walls of the vacuum chamber. The microwave discharge was delivered to the lamp via a McCarroll cavity powered by a microwave generator (Opthos Instrument Company, LLC, MPG-4M 437). For a detailed description of MDHLs including the typical UV emission spectrum for these UV lamps refer to Chen et al. (2013).

UV Flux Characterization

The UV flux (photons cm^{-2} s^{-1}) of the photolysis lamp is the amount of UV photons that bombard the ice surface per second. Several experimental factors can affect the UV flux of the MDHL, therefore, an in situ measurement of the UV flux is required during day-to-day experiments to ensure reproducibility.

The photon flux of the UV lamp can be measured throughout the duration of an experiment via a photoelectron technique described by Fulvio et al. (2014), that

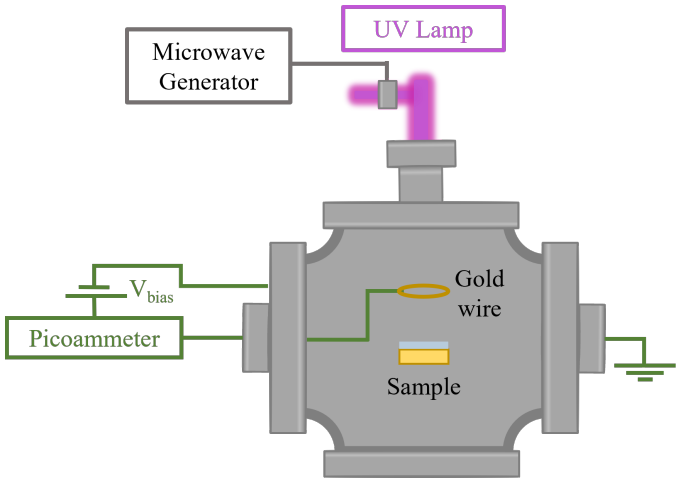

FIGURE 2.13: Electrical circuit for UV flux measurements.

utilizes the photoelectric effect of a gold wire suspended in the chamber about 1.5 inch above the ice sample. In these measurements, the chamber was incorporated into an electrical circuit and is shown in Figure 2.13.

When the photons collide with the gold wire (Surepure Chemetals, 99.99% gold, 0.040 inch diameter, 6 inch length) it displaces photoelectrons. The displaced electrons are collected by the chamber and replaced to the gold wire through the circuit. The circuit current is measured with a picoammeter (Keithley, 6485) and is then converted to flux via Equation 2.2 where F_λ is the photon flux, I is the measured current, e is the elementary charge, Y_λ is the photoelectric yield of gold, and A is the area of the gold surface.

$$F_\lambda = \frac{I}{e \times Y_\lambda \times A} \tag{2.2}$$

The measured current can become skewed from photoelectrons displaced from other vacuum chamber components and/or displaced electrons returning to the gold wire instead of being collected by the chamber. These effects can be minimized by the application of a bias voltage. When applying an increasing negative bias voltage to the gold wire the measured current reaches a maximum, or a "saturation current". When the current measurement reaches saturation this signals that all emitted photoelectrons are being collected by the chamber. The saturation current was measured for the experimental setup by plotting current vs. bias voltage and is shown in Figure 2.14. The saturation current was reached when -5 V bias was applied and

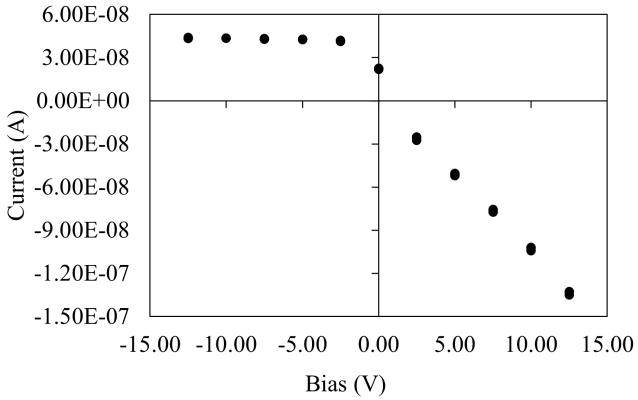

FIGURE 2.14: Measurements of current vs. bias voltage to determine the bias voltage required to achieve the saturation current.

matches the saturation current measured by Fulvio et al. (2014).

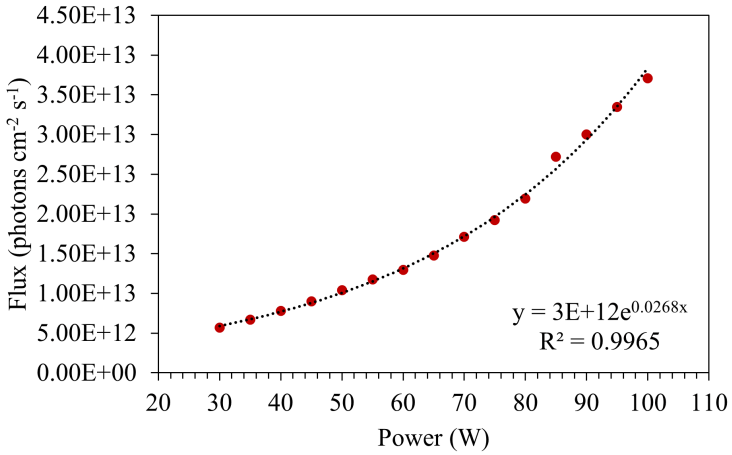

FIGURE 2.15: Relationship between UV flux and microwave power. The H_2 pressure in the flow lamp was 377 $\pm$ 2.0 mTorr for these measurements.

There are several factors that can affect the flux of the UV photons at the ice sample surface. Those factors include the microwave power of the discharge, the pressure of H_2 gas flowed through the lamp, and the distance from the lamp source to the sample. Several calibration tests were conducted to quantitatively determine how these factors affected the UV flux. First, the relationship between UV flux and microwave power was assessed (Figure 2.15). The UV flux was measured at a H_2 pressure of 377 $\pm$ 2.0 mTorr from 30-100 Watts. The flux of the lamp increased exponentially as the microwave power of the discharge increased. The cavity also heats

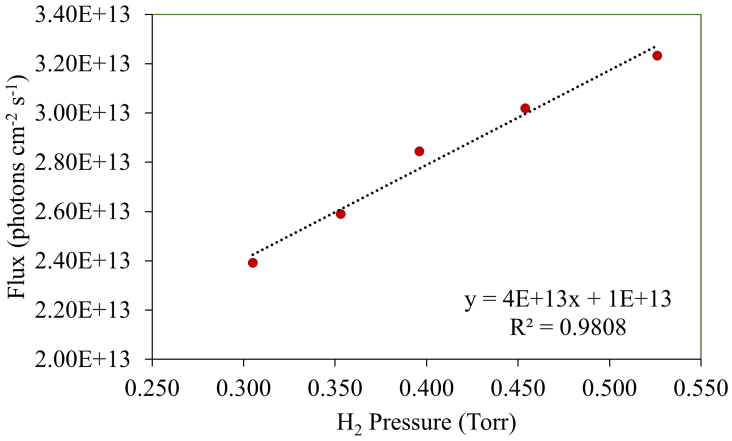

FIGURE 2.16: Relationship between UV flux and the pressure of H_2 in the flow lamp. The microwave power was set to 70 W for these measurements.

up significantly as the microwave power of the discharge increases. Although the cavity is cooled by a compressed air line, it can be risky to increase the microwave power above 100 W because if the lamp gets too hot it can melt the O-ring that seals the lamp or sometimes can even melt the quartz lamp body.

The dependence of the UV flux with respect to the H_2 flow pressure was also assessed (Figure 2.16). The UV flux was measured from ∼300-550 mTorr with the microwave power set to 70 W. The UV flux increased linearly as the H_2 flow pressure increased. For more details on how the UV flux can be affected refer to the study by Chen et al. (2013).

UV Photolysis and Photodesorption Experiments

Experiments that involve UV processing are photolysis and photodesorption experiments. UV photolysis experiments are focused on the chemical reactions that occur while an ice sample is exposed to UV photons for a certain amount of time (i.e., specific UV fluence). In general, the experiments are carried out as follows. First, an ice sample is formed at low temperature (∼10 K) via vapor (or gas) deposition. The ice sample is then photolyzed by exposing it to the UV lamp. The ice sample is monitored during photolysis by collecting IR spectra. Ice-phase photoproducts are then

identified by their IR vibrational transitions at specific stages of the photolysis process. After the photolysis time is complete, the lamp is turned off and the ice sample can be sublimated and the sublimated gas is then analyzed with mm/submm spectroscopy to identify and/or to confirm the detection of products proposed to be present in the IR spectra. Refer to Chapter 4 for an example of this category of experiment. As UV photons collide with the ice sample they also cause molecules to desorb via a nonthermal process referred to as UV photodesorption. During the UV processing the photodesorbed products are analyzed via mass spectrometry and mm/submm spectroscopy while the ice sample is held at low temperature (∼10-100 K). Refer to Chapter 5 for more details about UV photodesorption experiments.

2.3.2 Thermal Processing

Experiments that involve thermal processing of ice samples typically use a common surface-science technique called temperature programmed desorption (TPD). During a TPD experiment, the ice sample is heated with a constant heating rate and molecules are detected as they sublimate from the ice surface. The technique was originally designed for the detection of sublimated species via mass spectrometry where the mass spectrometer is set to the specific masses of the analytes and measured over time. TPD curves are then composed of the mass signal vs. time. The measured mass signal is proportional to the thermal desorption (or sublimation) rate of the analyte and TPD curves of thermal desorption rate vs. temperature can be used to calculate the surface binding energy of the analyte. This technique was adapted for experiments herein by detecting the sublimated species with mm/submm spectroscopy instead of mass spectrometry (Chapter 3). Thermal processing can also consist of a step-wise temperature warmup where the ice sample is held at a specific temperature(s) for a certain duration during the warmup process. Examples of this category of warmup are described in Chapter 3.

Chapter 3

Proof-of-Concept: Submillimeter Spectroscopic Detection of Sublimated Ice Samples

This chapter was reprinted, with minor adjustments, with permission from the authors of K.M. Yocum, H.H. Smith, E.W. Todd, L. Mora, P.A. Gerakines, S.N. Milam, S.L. Widicus Weaver. (2019) "Millimeter/Submillimeter Spectroscopic Detection of Desorbed Ices: A New Technique in Laboratory Astrochemistry." *J. Phys. Chem. A*, 123, 40, 8702–8708.

3.1 Introduction

Interstellar ice chemistry has been studied extensively through computational and laboratory studies, but after decades of research, we do not have fully-quantitative laboratory desorption data on species formed within icy dust grain mantles. The primary means of characterizing desorbed species is through mass spectrometry, and while this technique is extremely sensitive, it cannot be used to study most structural isomers or varying conformers of a given species due to mass overlaps. Many researchers use isotopic substitution to distinguish between isomers, but it has been shown that isotopologue desorption yields can differ significantly. For example, the laboratory study by Cruz-Diaz et al. (2017) reported a higher photodesorption yield for water (H_2O) at 8 K – (1.3±0.2) $\times$ 10^{-3} molecules photon^{-1} – than for deuterated water (D_2O) – (0.7±0.1) $\times$ 10^{-3} molecules photon^{-1}. Furthermore, in the case of

conformer analysis, even isotopic substitution will not be helpful in distinguishing various product channels. Isotopic substitution coupled with mass spectrometry is the most sensitive technique for determining compositions of ices desorbed during warm-up, but it is not always optimal when studying the chemical details of the photodesorption mechanism.

An in-situ laboratory technique that is capable of probing the thermal desorption of ices is molecular spectroscopy – specifically rotational spectroscopy, which is structure-specific and highly sensitive. Rotational spectroscopy is the primary method used in remote observations to study species desorbed from interstellar dust grains and cometary comae. Hence, laboratory-measured rotational spectra are directly comparable to those collected via ground- and space-based telescopes at these wavelengths. Although rotational spectroscopy has less-sensitive detection limits than mass spectrometry, gas-phase rotational spectroscopic techniques complement the results of more traditional laboratory approaches to studying interstellar and cometary ice analogs (e.g., mass spectrometry, IR spectroscopy). Remarkably, despite its prolific use in molecular identification for observational astronomy, to our knowledge there are no reported studies of laboratory spectroscopic detections of desorbed ice species in the millimeter and submillimeter (mm/submm) region. This work demonstrates an experimental technique designed for analyzing desorbed species from ices using mm/submm spectroscopy. The main goals of using this technique are (1) to aid in the distinction of structural isomers that desorb from laboratory ices and (2) to produce spectroscopic results that are directly comparable to observational data from mm/submm (including far-IR) telescopes. Herein the details of the experimental design and performance are described, and the results for thermally desorbed ices composed of water (H_2O and D_2O) or methanol (CH_3OH) are reported.

3.2 Background

3.2.1 Comparison of Laboratory Techniques

Traditional laboratory studies of interstellar ice chemistry have been conducted at IR wavelengths and are often complemented with mass spectrometry (Abplanalp et

al., 2019; Allamandola et al., 1988; Greenberg et al., 1972; Hudson et al., 1991; Öberg et al., 2009b). The IR-active vibrations of complex molecules show significant spectral overlap due to functional groups they have in common, making unique identifications difficult without complementary mass spectrometric (MS) results. Moreover, mass spectrometers are extremely sensitive, and they can measure trace species present under ultra-high-vacuum (UHV) conditions (P <10^{-8}). Even so, the coupling of IR and MS cannot decipher between some structural isomers. For example, glycolaldehyde ($HCOCH_2OH$) and methyl formate ($HCOOCH_3$), both with a mass of 60 amu. This method is also unable to distinguish between the methanol photodissociation products CH_3O and CH_2OH. As such, the traditional technique of coupling IR spectroscopy with mass spectrometry is not always sufficient to distinguish between all desorbed molecules of interest.

The technique presented in this work addresses this limitation of laboratory ice studies, because rotational spectroscopy is structure-specific and employs a high spectral resolution (0.1 MHz), enabling distinct identifications of each species from their unique, pure rotational spectrum, with no spectral or mass signal overlaps. Implementation of rotational spectroscopic analysis of desorbed ice species has the potential to significantly advance studies in laboratory astrochemistry and can provide a a greater understanding of the observed abundances of complex organic molecules throughout the universe.

3.2.2 Thermal Desorption of Water and Methanol Ice Samples

Water is the most abundant constituent of observed interstellar and cometary ices (Boogert et al., 2015; Gibb et al., 2004; Lecacheux et al., 2003; Öberg et al., 2011). Many laboratory studies of the thermal desorption of water ice have been reported and will be briefly discussed herein. Table 3.1 lists the kinetic parameters for the thermal desorption (i.e., sublimation) of water ice collected by temperature-programmed desorption (TPD) and quartz-crystal microbalance (QCM) methods as reported in previous studies. The substrate compositions, deposition temperatures, and heating rates are also listed.

The surface binding energies range from 0.41 to 0.60 eV, with most values lying closer to 0.41 eV. A thorough discussion of the differences in binding energies that

TABLE 3.1: An overview of the thermal desorption kinetic parameters of previous H_2O ice studies.

Surface Binding Energy (eV)	Desorption Order	Substrate	Deposition Temperature (K)	Heating Rate (K s^{-1})	Reference
0.48 ± 0.03	0 ± 0.25	HOPG*		0.25-2.0	Ulbricht et al., 2006
0.41 ± 0.01	0.26 ± 0.02	HOPG*	90	0.50 ± 0.01	Bolina et al., 2005b
0.60 ± 0.01	0	Ru(001)	160	Isothermal	Smith et al., 2003
0.50 ± 0.01	0	Gold	10	0.02	Fraser et al., 2001
0.5 ± 0.01	0	Ru(001)/Au(111)		0.6	Speedy et al., 1996
0.45 ± 0.03	0	Graphite(0001)	85	2.5	Chakarov et al., 1995
0.45 ± 0.03		Gold coated QCM	60	0.02	Sack et al., 1993
0.52	0	Sapphire		Isothermal	Haynes et al., 1992
0.44 ± 0.004	1	CsI	10	0.03	Sandford et al., 1988

*Highly Oriented Pyrolytic Graphite

results from different experimental techniques can be found in the review by Burke et al. (2010). In Section 3.4.1, we compare our results for H_2O using the mm/submm technique to those listed in Table 3.1.

Previous studies also have been performed for deuterated water (D_2O). Although the desorption processes for H_2O and D_2O are analogous, their parameters (i.e., binding energies, desorption yields) are not the same. Schmitz et al. (1987) were the first to show an isotope effect in water desorption when they examined the thermal desorptions of solid H_2O and D_2O from a Ru(001) surface. Other water isotopologues have been studied, including $D_2^{18}O$ (Chaix et al., 1998) and $H_2^{18}O$ (Smith et al., 2003). The work presented here focuses on $D_2^{16}O$ and demonstrates our ability to detect isotopologues at their distinct frequencies.

The work presented here also includes the thermal desorption of solid methanol (CH_3OH). The thermal desorption of CH_3OH has been studied extensively (Bolina et al., 2005a; Green et al., 2009; Nishimura et al., 1998; Sandford et al., 1993; Ulbricht et al., 2006; Wolff et al., 2007) and an in-depth discussion of these studies can be found in the review by Burke et al. (2010). Methanol is a significant molecule in astrochemistry because it is abundant in interstellar ices (Öberg et al., 2011) and is the chemical starting point for many larger organic molecules upon energetic processing (2021 and references therein).

The work presented here focused on benchmarking experiments on the thermal desorption of water (H_2O), given the extensive amount of existing literature related to H_2O desorption available for comparison. Measurements were also extended to include studies of solid D_2O and CH_3OH to provide a more complete proof-of-concept.

3.3 Experimental Methods

The studies reported in this chapter were performed in experimental setup 2 described in Chapter 2 Section 2.1.2 and a detailed schematic can be found in Figure 2.3. The gas-phase products of thermally desorbed ice samples were detected using the mm/submm spectrometer described in Chapter 2 Section 2.2.1 and a detailed schematic of the custom designed spectrometer is shown in Figure 2.6. A Teflon lens (Thorlabs^{TM}) collimated the light through a sapphire view-port. The mm/submm light passed ∼1-2 cm above the ice sample, exited the chamber through a second sapphire viewport, and was focused via a second Teflon lens into the cryo-cooled THz bolometer. Lastly, a lock-in amplifier was used to increase the signal-to-noise ratio. The input radiation was frequency-modulated at 0.2 kHz and a lock-in amplifier was used for phase-sensitive detection, resulting in second-derivative line shapes. Spectra were recorded with a resolution of 0.10 MHz and the spectrometer was controlled using a custom designed data acquisition software.

3.3.1 Thermal Desorption of Ice Samples

The experimental procedure for studying thermal desorption was analogous to a traditional TPD experiment, but with one difference: the desorbed species were detected with mm/submm spectroscopy instead of mass spectrometry. The ice samples were formed at 12 K by slowly leaking a vapor into the chamber at $\sim 5 \times 10^{-7}$ Torr. The vapor entered the chamber about 1 inch above the gold substrate through a capillary tube connected to a high-precision gas dosing valve. Next, the ice samples were heated from 12-200 K at a 1 K min^{-1} rate and the rotational absorption signal of the thermally-desorbed species were recorded as a function of time and temperature.

3.4 Results and Discussion

3.4.1 Thermal Desorption of H_2O, D_2O, and CH_3OH

Figure 3.1 shows the submm spectra for thermally desorbed H_2O, D_2O, and CH_3OH ice samples. Thermal desorption traces of desorption rate vs. temperature were

constructed for H_2O (see Figures 3.3 and 3.4). Thermal desorption traces for three different ice thicknesses are shown in Figure 3.3. These spectra were collected from 100 – 200 K at 5 K increments. A relative thermal desorption rate was obtained from the peak absorption of each rotational transition at a given temperature by the following method. The peak intensity, $I(T)$, of the rotational transition is directly proportional to the thermal desorption rate, R, and the loss of ice molecules over time, $-\frac{dN}{dt}$:

$$I(T) \propto R \propto -\frac{dN}{dt} \tag{3.1}$$

and

$$-\frac{dN}{dt} = NAexp(\frac{-E_{des}}{k_B T}) \tag{3.2}$$

where N is the number of molecules in the ice, A is the pre-exponential factor, E_{des} is the ice surface binding energy, k_B is the Boltzmann constant, T is the temperature in Kelvin, and a first-order desorption process was assumed. By plotting the relative thermal desorption rate obtained from the peak absorption signal versus inverse temperature, E_{des} can be calculated from an exponential fit (see Figure 3.5).

To verify the linear proportionality between absorption intensity, $I(T)$, and desorption rate, R, (Eq. 3.2), a quantitative thermal desorption rate was determined by isothermally desorbing 1.6 μm H_2O ice samples at 150, 155, 162, 165, 168, and 170 K. Interference fringes were measured using the 670-nm laser diode. The thermal desorption rate at each temperature was calculated in μm s^{-1}. The submm absorption intensities at these temperatures were then plotted against the μm s^{-1} desorption rates (see Figure 3.2). A linear best fit gave the calibration equation

$$I(T) = 1.264 \times 10^6 (R) + 126.5 \tag{3.3}$$

and an R^2 of 0.99.

For this new technique, it may be more useful to calibrate the thermal desorption rate with respect to the number density of the desorbed gas-phase products. For this calibration, the density of H_2O molecules was measured using a mass spectrometer

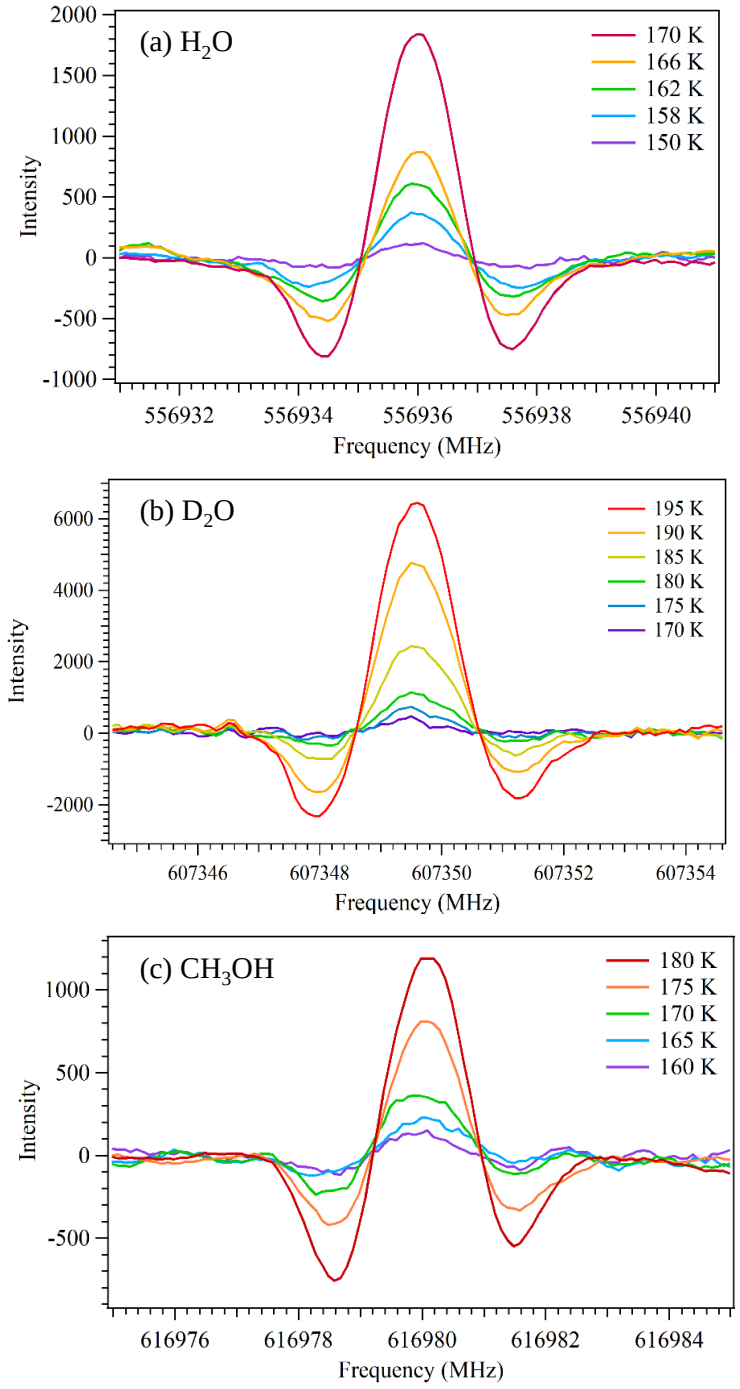

FIGURE 3.1: (a) Spectra of the $1_{1,0} \leftarrow 1_{0,1}$ rotational transition of thermally desorbed H_2O at 150-170 K. (b) Spectra of the $1_{1,1} \leftarrow 0_{0,0}$ rotational transition of thermally desorbed D_2O at 170-195 K. (c) Spectra of the $13_{-1,13} \leftarrow 12_{-1,12}$ rotational transition of thermally desorbed CH_3OH at 160-180 K.

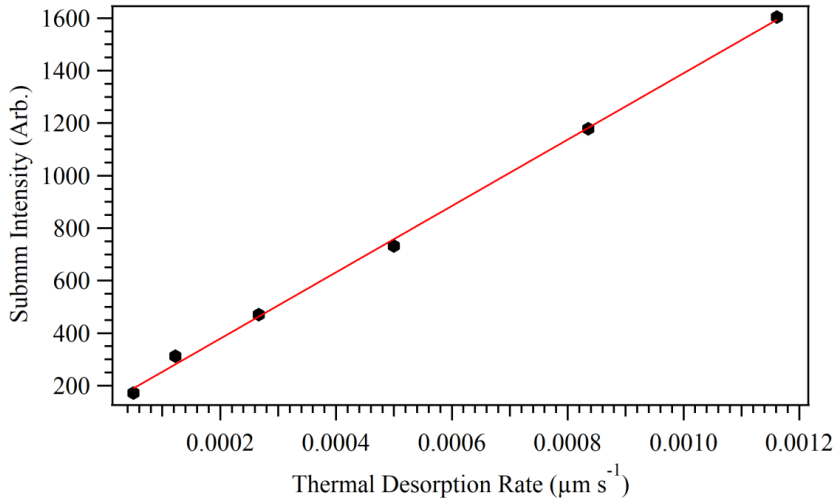

FIGURE 3.2: Linear relationship between the submm peak absorption intensity and the thermal desorption rate of a H_2O ice sample.

from 150 – 180 K. This calibration corrects for the effective pumping speed (EPS) of the chamber and the gas-phase species that recondense onto the cryostat. First, the density of H_2O (molecules cm^{-3}) was multiplied by the EPS (cm^3 s^{-1}) and divided by the volume of the chamber (cm^3). Next, the rate of which the cryostat removes H_2O from the chamber was added to the EPS calibrated thermal desorption rate (molecules cm^{-3} s^{-1}). The rate of which molecules condense onto the cryostat was measured by simply introducing a known density of H_2O vapor into the chamber with the gate valve closed, and the density of H_2O was measured over time with the mass spectrometer. These measurements were performed across the thermal desorption window of H_2O ice (145-180 K). The recondensation rate was the same across this temperature range. The submm absorption intensity, $I(T)$, was then plotted against R in molecules cm^{-3} s^{-1} to determine the desorption rate calibration function

$$I(T) = 3.04 \times 10^{-9}(R) - 4.37, \tag{3.4}$$

and a R^2 value of 0.99. The calibrations reported in Eq. 3.3 and 3.4 are necessary for future reports of quantitative values of desorbed species (e.g., gas-phase concentrations).

Since this is the first report of detecting thermally desorbed ice samples spectroscopically, no previously reported studies offered a direct comparison. The spectroscopic method used here differs from TPD experiments simply because it monitors the center frequency of a rotational transition instead of a mass signal. Nonetheless, the data were analyzed in a similar manner as TPD data to determine E_{des}. The binding energy reported here for H_2O matched those reported by several others within experimental error (see Table 3.1) (Chakarov et al., 1995; Fraser et al., 2001; Haynes et al., 1992; Sack et al., 1993; Speedy et al., 1996; Ulbricht et al., 2006).

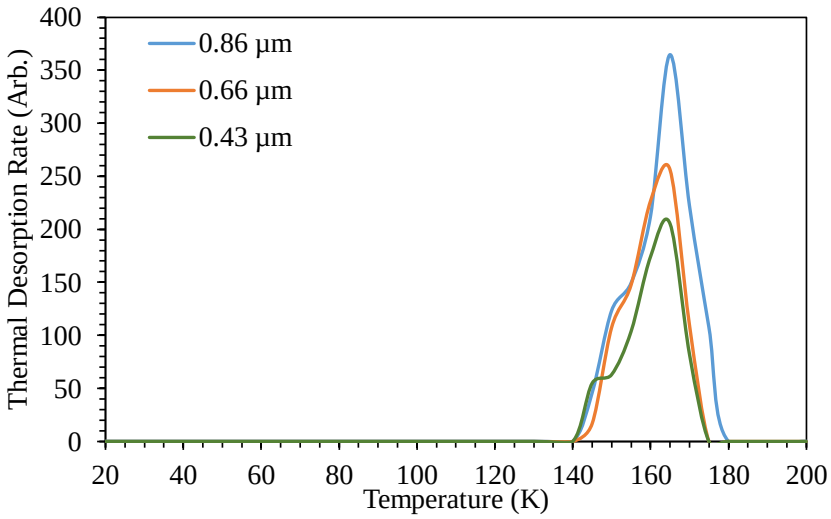

FIGURE 3.3: Thermal desorption curve of 0.86, 0.66, and 0.43 μm H_2O ice samples.

In Figure 3.3 the thermal desorption curves of the 0.86, 0.66, and 0.43 μm ice H_2O ice samples all peak at the same temperature, 165 K, suggesting first-order kinetics (Fraser et al., 2001). However, it has been shown that fractional-order kinetics better describes hydrogen-bonded systems including water (Bolina et al., 2005b; Smith et al., 1996) and alcohols including methanol (CH_3OH) and ethanol (CH_3CH_2OH) (Bolina et al., 2005a; Nishimura et al., 1998; Wu et al., 1993). Furthermore, a study by Green et al. (2009) showed that at low methanol coverages, thermal desorption demonstrates fractional order, and at high coverages the desorption follows zero-order kinetics. Here the desorption order was not quantitatively determined because the ice coverage was not quantified.

The thermal desorption curve of a thicker ice, 1.6 μm, is shown in Figure 3.4.

The thermal desorption curve shown in Figure 3.4 was produced using the same procedure as mentioned previously by monitoring the intensity of the $1_{1,0} \leftarrow 1_{0,1}$ rotational transition of thermally desorbed H_2O over time as the ice sample was heated from 12-190 K at a 1 K min^{-1} rate. The mass signal at 18 amu was simultaneously monitored with a mass spectrometer.

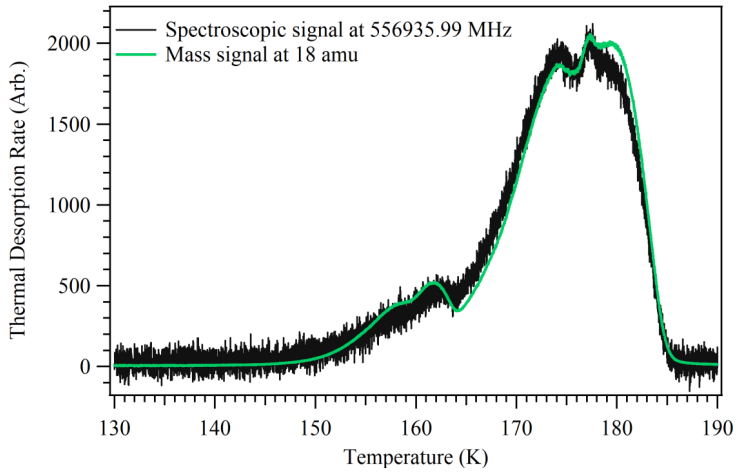

FIGURE 3.4: Thermal desorption curve of a 1.6 μm H_2O ice detected with the mm/submm spectrometer (black) and the mass spectrometer (green). The mass signal was multiplied by 10^{10} to be scaled to the intensity of the spectroscopic signal.

There are three noticeable features that appear in the thermal desorption curve in Figure 3.4 at ~160, 173, and 178 K. These features result from phase changes of the solid water ice sample. A peak at ~150-160 K has been reported several times in the literature as being present in water thermal desorption curves and corresponds to the phase change from amorphous solid water to cubic crystalline ice (Bolina et al., 2005b; Dohnlek et al., 1999; Smith et al., 1997; Smith et al., 1996; Speedy et al., 1996). A higher temperature phase transition at 175 K from cubic crystalline ice to hexagonal ice was seen in the desorption trace of the 0.86 μm ice in Figure 3.3 and at ~178 K in the 1.6 μm trace in Figure 3.4. Bolina et al. (2005b) were the first to observe this phase transition in their TPD studies of a thermally desorbed water ice sample from highly oriented pyrolytic graphite (HOPG). By 180-185 K, the 1.6 μm ice sample was completely sublimated. Figure 3.4 also displays a comparison to a thermal desorption curve measured with a mass spectrometer at 18 amu. The peak thermal desorption rates, phase transitions, and final and initial detections occur at the same

temperatures in both curves. Therefore, measuring thermally desorbed species with the mm/submm spectroscopy method put forth here is directly comparable to the well-established mass spectrometric TPD method. Furthermore, the surface binding energy (E_{des}) was calculated by plotting the relative thermal desorption rate versus inverse temperature. The exponential fit to these data yielded E_{des} (see Figure 3.5).

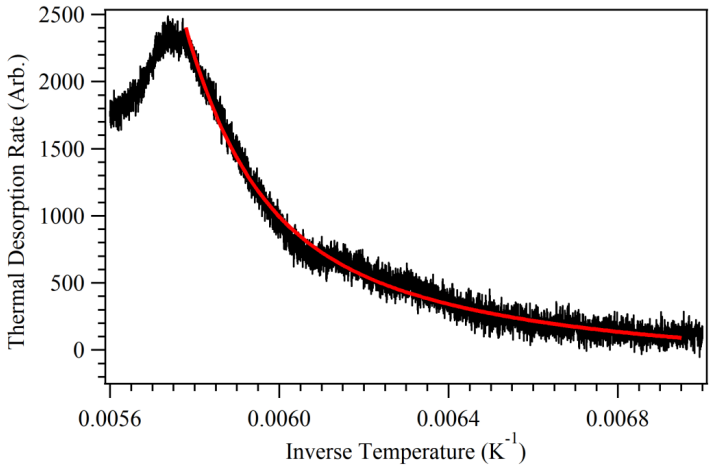

FIGURE 3.5: Thermal desorption rate versus inverse temperature for the 1.6 μm H_2O ice. The exponential fit to determine E_{des} is shown in red.

The binding energy calculated from the exponential fit in Figure 3.5 was 0.45 $\pm$ 0.06 eV. The average binding energy after repeating this experiment five times was 0.47 $\pm$ 0.02 eV.

This new technique can also be used to determine the sublimation enthalpy, ΔH, of ice samples over specific temperature ranges using the Clausius-Clapyron equation

$$P_V = e^{\frac{-\Delta G}{RT}}. \tag{3.5}$$

In Eq. 3.5, P_V is vapor pressure, ΔG is the free energy of sublimation, R is the ideal gas constant, T is temperature, and

$$\Delta G = \Delta H - T\Delta S, \tag{3.6}$$

where ΔH is the sublimation enthalpy and ΔS is the sublimation entropy. Rearrangement of Eq. 3.5 gives the linear form of the Clausius-Clapyron equation

$$ln(P_V) = -\frac{\Delta H}{RT} + \frac{\Delta S}{R}, \tag{3.7}$$

By plotting $ln(P_V)$ versus $1/T$ the sublimation enthalpy can be obtained from the slope, and the entropy from the y-intercept of the best fit line (see Figure 3.6). The Knudsen equation was used to derive the vapor pressure for temperatures of 145-175 K:

$$R = \frac{P_V}{\sqrt{2\pi M k_B T}}, \tag{3.8}$$

where R is the desorption rate and M is molecular mass. The linear fit in Figure 3.6 had an R^2 value of 0.99 and the sublimation enthalpy and entropy were 0.286 $\pm$ 0.006 eV and 0.00127 $\pm$ 0.00004 eV, respectively.

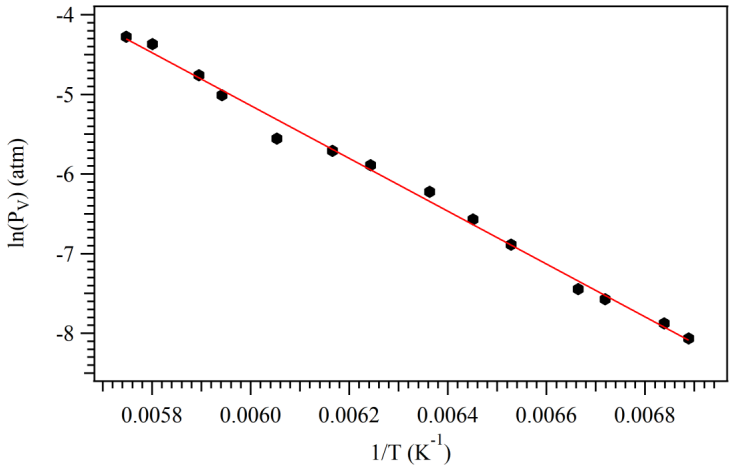

FIGURE 3.6: Clausius-Clapeyron relationship for a 1.6 μm H_2O ice from 145 - 175 K to determine ΔH and ΔS.

Although the results using this new technique matched literature values within experimental error, the detection limits of mass spectrometry are lower than submm spectroscopy. Therefore, using this technique for determining kinetic parameters is not recommended over mass spectrometry unless one is studying species of the same mass which cannot be distinguished. Nonetheless, the agreement between the two techniques shows that the new method provides a valuable path forward for studying interstellar and cometary ice chemistry when infrared and mass spectrometric analysis does not provide sufficient means for identifying products.

3.5 Conclusions and Future Work

This study presented a new laboratory technique for detecting thermally desorbed ice samples. This is the first known report of detecting sublimated molecules from laboratory ices spectroscopically at mm/submm wavelengths. This technique is powerful in that it is capable of distinguishing isomeric products that may form during the thermal desorption of ice samples, and the submm spectra are directly comparable to observational data from far-infrared and millimeter observatories. This work has shown proof-of-concept for analyzing thermally desorbed ice samples with mm/submm spectroscopy by presenting submm spectra of thermally desorbed H_2O, D_2O, and CH_3OH ice samples. Future efforts will focus on optimizing the detection of UV-photodesorbed products of H_2O and CH_3OH ice samples. The focus for these future experiments will be on the detection of the photodesorbed radicals including OH.

Chapter 4

Structure-Specific Identifications of Products of UV-photolyzed Methanol Ice with SubLIME

This chapter was reprinted, with minor adjustments, with permission from the authors of K.M. Yocum, S.N. Milam, P.A. Gerakines, S.L. Widicus Weaver. (2021) "Sublimation of Laboratory Ices Millimeter/Submillimeter Experiment (SubLIME): Structure-Specific Identifications of Products of UV-photolyzed Methanol Ice" *Astrophys. J.*, 913, 61.

4.1 Introduction

In cold dense interstellar clouds, icy dust grains are constantly bombarded with different forms of radiation that alter the molecules in the ice by ionizing them and/or breaking them down into radicals. Those species recombine in different configurations that in many cases result in more complex molecules than the original reactants. Those products can then be ejected into the gas phase by different physical processes, including, but not limited to, heating from nearby protostar formation, photodesorption caused by exposure to ultraviolet (UV) photons, reactive desorption, and sputtering from cosmic ray collisions. In this way, there exists a close connection between ice chemistry and the gas compositions of interstellar clouds, a relationship that remains only poorly understood. Furthermore, several volatile organics that have been detected in the interstellar medium (ISM) have also been

detected in comets, in some cases with similar abundance ratios (Bockelée-Morvan et al., 2000; Drozdovskaya et al., 2018; Rubin et al., 2019b), providing evidence for the preservation of organic species from the earliest stages of star formation to their incorporation in comets and other icy solar system bodies such as Kuiper Belt Objects (KBOs).

Laboratory studies have demonstrated the importance of ice surface chemistry for complex organic formation in the ISM by providing necessary information (e.g., reaction rate constants, surface binding energies, formation mechanisms, branching ratios) to improve the accuracy of computational models (Abplanalp et al., 2016; Bergantini et al., 2018; Paulive et al., 2020; Shingledecker et al., 2018a). Methanol (CH_3OH), plays an important role in this chemistry, because once dissociated it provides functional groups CH_3, OH, CH_3O, and CH_2OH that can be used to build larger organics, and it is abundant in both interstellar and cometary ices. Laboratory studies of the energetic processing (e.g., UV photolysis, electron and proton irradiation) of ices containing methanol have predicted formation pathways for larger organics such as ethanol (CH_3CH_2OH) (Abou Mrad et al., 2016; Henderson et al., 2015; Öberg et al., 2009a), dimethyl ether (CH_3OCH_3) (Abou Mrad et al., 2016; Öberg et al., 2009a), methyl formate ($HCOOCH_3$) (Abou Mrad et al., 2016; Gerakines et al., 1996; Henderson et al., 2015; Öberg et al., 2009a), glycolaldehyde ($HOCH_2CHO$) (Henderson et al., 2015; Öberg et al., 2009a), acetic acid (CH_3COOH) (Abou Mrad et al., 2016; Öberg et al., 2009a), and many more upon sample warm-up. Many of these products are structural isomers built from the key functional groups of methanol.

The most common laboratory technique for gas-phase detections following ice sublimation is electron-ionization mass spectrometry, but the similarities in chemical structures between these products results in crowded mass spectra riddled with overlapping features. Coupling with gas chromatography provides a potential resolution of this issue, but the components of the sample must be known in order to determine the appropriate separation conditions for analysis (Abou Mrad et al., 2014). Therefore, laboratory studies require structure-specific techniques to distinguish and quantify structural isomers (e.g., C_2H_6O and $C_2H_4O_2$) and to potentially uncover the carriers of as-yet-unassigned features of complex organic species in astronomical observations.

Rotational spectroscopy is a highly useful technique for measuring the compositions of complex gas mixtures. Gas-phase spectroscopy has been demonstrated as an in-situ detection method for desorbed laboratory ices at submillimeter/far-IR wavelengths (Yocum et al., 2019) and at microwave wavelengths (Theulé et al., 2020). Not only is this a non-invasive technique (i.e., the experimental and/or sample conditions are unaltered), but radio and far-IR spectroscopies are the most widely-used remote sensing techniques for probing the gas-phase compositions of interstellar clouds, cometary comae, and planetary atmospheres. The work presented here expands upon the submillimeter spectroscopic technique put forth by Yocum et al. (2019) by demonstrating the detection capabilities for sublimated UV photoproducts of methanol ice including the unique detections of the structural isomers C_2H_4O, C_2H_6O, and $C_2H_4O_2$. Secondly, the temperatures and densities of the detected photoproducts were determined via a rotation diagram analysis and compared to astronomical observations of complex organics detected in interstellar and cometary sources.

4.2 Experimental Techniques

All reported experiments were conducted in experimental setup 2 described in Chapter 2 Section 2.1.2. The experimental setup consists of an ultra-high vacuum (UHV) chamber with a base pressure of $\sim 1 \times 10^{-9}$ Torr. For the experiments performed here, ice samples were created at 12 K on a gold substrate attached to a closed-cycle helium cryostat and then were exposed to UV photons. After UV photolysis, the valves to the pumps were closed and the ices were heated slowly to 300 K in order to fully sublimate the sample and trap it in the vacuum chamber. The sublimated species were then detected with submillimeter/far-IR spectroscopy to identify chemical products. Furthermore, a rotation diagram analysis was performed for each individual product to determine the rotational temperatures and gas densities relative to the amount of methanol detected. Each of these steps are presented in detail in the following sections.

4.2.1 Ice Sample Creation

The methanol ice samples were formed by vapor deposition onto the cold substrate through a high-precision gas-dosing valve. The vapor enters the chamber approximately one inch above the substrate through a capillary tube (1/32-inch inner diameter) attached to the gas-dosing valve. The overall pressure of the chamber reached 1.0×10^{-7} Torr for 20 min. during deposition. The vapor was evaporated from 99.9% HPLC grade liquid methanol (Fisher Scientific, A452-4) that was degassed by three freeze-pump-thaw cycles. After an ice sample was formed, the chamber was pumped until the pressure returned to the base pressure at the start of the experiment.

4.2.2 UV Photolysis and Thermal Processing of Ice Samples

The ice samples were exposed to the output of a microwave-discharge hydrogen-flow lamp (MDHL) that simulated the UV radiation field present in an interstellar cloud. The photons enter the chamber through a MgF_2 ConFlat^{TM} viewport with an incidence angle of 13° at the surface of the ice. The MDHL has an F-type configuration and is constructed of quartz. Hydrogen gas was flowed through the lamp at pressures of $\sim$ 450 mTorr and an Evenson cavity was used to spark a microwave discharge across the quartz lamp body. For all experiments, the microwave generator (Opthos MPG-4 526) forward power was 100 Watts and reflected power was $\sim$ 0-2 Watts. For a detailed description of MDHLs including the typical UV emission spectra for these UV lamps refer to Chen et al. (2013). The average flux of the UV lamp was $6.0 \pm 1.0 \times 10^{13}$ photons cm^{-2} s^{-1}, as was measured throughout the duration of one experiment via the technique described by Fulvio et al. (2014), utilizing the photoelectric effect of a gold wire suspended in the chamber about one inch above the ice sample. The methanol ice sample was photolyzed for one hour, exposing the sample to a total fluence of $2.2 \pm 0.35 \times 10^{17}$ photons cm^{-2}.

After the methanol ice samples were photolyzed, the UV lamp was turned off, the valve to the pump was closed, and the sample was slowly heated from 12 to 300 K at 1 K min^{-1}. The cryostat was turned off during the sample warm-up to avoid recondensation. Infrared spectra of the ice samples were collected simultaneously

with mass spectra of the species that desorbed during the sample warm-up. These spectra were obtained in 10 K increments.

4.2.3 Infrared Spectra of Methanol Ices

The methanol ice samples were monitored using IR spectroscopy during the UV photolysis and the warm-up procedure. IR spectra were collected with a Thermo Scientific Nicolet^{TM} iS50 FTIR spectrometer via the reflection-absorption infrared spectroscopy (RAIRS) technique. The IR beam enters the chamber through a ZeSe viewport (Kurt J. Lesker) with a $\sim 77^{\circ}$ angle of incidence where it is reflected from the gold surface, exits the chamber through a second ZeSe viewport, and is detected by a liquid-nitrogen cooled mercury-cadmium-telluride (MCT) detector.

IR spectra were collected in 10-min intervals during photolysis from the MDHL. After being photolyzed, the ice samples were slowly heated to 300 K and IR spectra were collected every 10 K to determine the temperatures at which specific IR features changed and to ensure full sublimation of the ice sample.

4.2.4 Submillimeter/far-IR Spectra of Sublimated UV-Photolyzed Methanol Ices

A thorough description of the millimeter/submillimeter/far-IR spectrometer has been given in Chapter 2 Section 2.2.1. In brief, the spectral range covers 70-1000 GHz, 1.8-1.9 THz, and 2.5-2.6 THz. The setup uses lock-in amplification to improve signal-to-noise ratio. The input radiation was frequency-modulated at 0.2 kHz with a modulation depth of 75 kHz. This is a phase-sensitive detection technique which results in 2f spectral line shapes. All spectra were collected with 0.1-MHz resolution, and the number of spectral averages varied based on the experimental approach (broadband vs. targeted searches) and the detection limits of the molecules of interest.

Gas-phase direct-absorption submillimeter/far-IR spectra were collected for the molecules sublimated from the UV-photolyzed methanol ice samples. By closing the gate valve between the chamber and the turbomolecular pump, the sublimated products were trapped in the main vacuum chamber while spectra were measured.

While the system remained at $\sim$ 300 K, broadband spectra were collected between 758-926 GHz and any absorption peak with a signal-to-noise ratio $\geq$ 5 was considered a detection.

After identification of several photoproducts from the broadband submillimeter spectra, more sensitive, targeted searches were carried out to search for weaker species that may have been present. The targeted searches spanned $\sim$ 10 MHz-wide spectral windows with the specific transition frequency of a given species set at the center of the spectral window. The number of spectral averages varied for each targeted search, based on the spectral power at a given frequency, the intensity of the peaks of the specific species, and its relative abundance. Some detections only required 30 averages while others required up to 200 averages. The selected rotational transitions were determined based on a list of criteria: spectral power, reported intensity of the target transition, and lack of overlap with methanol or potential photoproducts. It is important to note that the spectrometer does not generate consistent power across the entire 70 - 1000 GHz range. There are several small regions where there was little to no power produced by the light source. The output spectral power was therefore the first criterion for potential detection, and only regions with sufficient power in this system were selected. Secondly, the detection limits of this technique in terms of peak intensity were determined throughout the project for each specific product. Lastly, complex mixtures have submillimeter spectra that can be crowded, causing blending between different transitions of varying products. With all three of these criteria in mind, the selected transitions correspond to the combination of highest spectral power + largest peak intensity + resolved transitions.

4.2.5 Standards and Background Tests

Molecular standards were used for spectral assignments in the solid-phase RAIRS spectra and in the gas-phase submillimeter/far-IR spectra. The IR spectra were assigned by comparison to reference FTIR spectra of acetaldehyde (Hudson et al., 2019), acetone (Hudson et al., 2018), acetic acid, dimethyl ether (Hudson et al., 2020), ethanol (Hudson, 2017), ethylene glycol (Hudson et al., 2005), formaldehyde (Gerakines et al., 1996), formic acid, glycolaldehyde (Hudson et al., 2005), and methyl

formate (Modica et al., 2010). The majority of the spectral assignments for the gas-phase spectra were aided by simulated spectra from online spectral databases including the JPL[1] and CDMS[2] catalogs. Molecular searches were also conducted through comparison with Splatalogue[3], which combines spectral catalog information from multiple spectral databases.

Gas-phase reference spectra were collected of acetaldehyde due to several missing transitions in the online databases and the large uncertainties of the transition frequencies that are reported. These reference spectra were collected by adding a small amount of acetaldehyde vapor into the chamber. The chamber was filled to $\sim$ 1.0 mTorr, and spectra were collected over all spectral windows to confirm that peaks assigned to other photoproducts were not those of acetaldehyde. Reference spectra were also collected for methanol, even though the spectral catalogs for methanol and its isotopologues are thoroughly studied. This was done to verify that no higher vibrational states of methanol and its isotopologues were present, considering the spectral catalogs were calculated for v = 2 and lower. Therefore, all detections reported were checked against methanol and acetaldehyde reference spectra.

Two submillimeter background tests were conducted to ensure that all of the detected transitions originated from species desorbed from the photolyzed methanol ice sample and not from residual gases in the vacuum chamber. The first test involved experiments that replicated the UV photolysis and warm-up procedure with no ice sample present to ensure all detected photoproducts came from the photolyzed ice. From this test, the only background contamination detected by the millimeter/submillimeter/far-IR spectrometer after warm-up was a small amount of carbon monoxide, CO. No CO was detected by the FTIR spectrometer at a substrate temperature of 12 K. The origin of background CO was likely due to outgassing of the chamber walls and other chamber components when the gate valve was closed to the pumps. The second background test was conducted to confirm that no photoproduct transitions were detected without exposure to UV radiation. These experiments replicated the ice deposition and warm-up procedures without running the UV lamp. The only background contamination, again, was a small amount of

[1] spec.jpl.nasa.gov
[2] cdms.astro.uni-koeln.de/classic
[3] splatalogue.online

CO. This background CO was quantified and subtracted from the experimental data presented here. Mass spectrometer background scans at the beginning of daily experiments showed trace amounts of H_2, H_2O, CO, and CO_2 (less than $\sim 3.2 \times 10^7$ molec. cm^{-3}).

4.3 Results and Analysis

Several photoproducts were produced in the 12 K ice sample after the one-hour UV-photolysis and were detected with the FTIR spectrometer. The submillimeter spectroscopic detection of additional photoproducts occurred after the ice warm-up to 300 K under static vacuum. In this section, the photoproducts detected in the ice at 12 K are presented in Section 4.3.1, changes in the IR spectra during ice warm-up from 12 to 300 K are presented in Section 4.3.2, all photoproducts detected after warm-up to 300 K are presented in Section 4.3.3, and their respective rotational-diagram analyses can be found in Section 4.3.4.

4.3.1 Low Temperature UV Photolysis at 12 K

Chemical changes of the methanol ice were captured in IR spectra every 10 min. as the ice sample was photolyzed for one hour. Figure 4.1 shows IR spectra of the background before ice deposition (No ice), methanol ice before (0 min), during (10-50 min), and after (60 min) the one-hour UV exposure.

In Figure 4.1, the large methanol peak at 1044 cm^{-1} decreased significantly as the UV fluence increased, confirming the photodestruction of methanol. Several IR features appeared as the UV fluence increased as well. Over the one-hour exposure, these features continually increased in absorbance. Figure 4.2 shows the spectrum of the methanol ice before and after photolysis in the 1400-800 cm^{-1} range to highlight IR features that arise primarily from larger organics. See Table 4.1 for a list of IR assignments.

Many of the features listed in Table 4.1 have more than one possible carrier and are indistinguishable without further studies, such as isotopic substitution for example. More products were identified upon ice warm-up, but it should be noted that

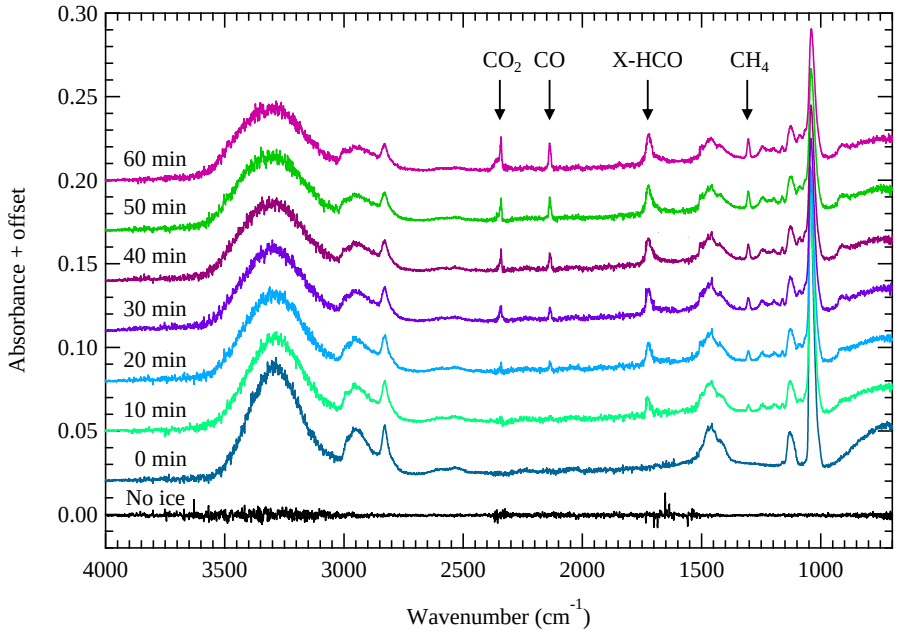

FIGURE 4.1: IR spectra of methanol ice exposed to UV photons at 12 K. The spectra are offset for clarity. IR assignments of species formed during photolysis are listed in Table 4.1.

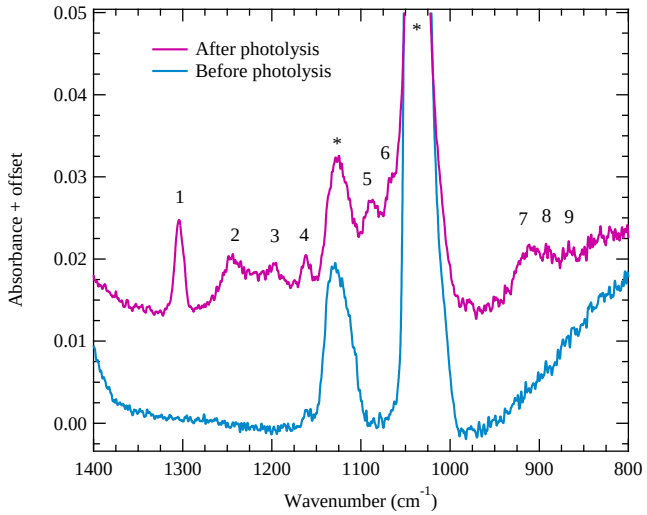

FIGURE 4.2: 1400-800 cm^{-1} IR spectrum of methanol ice at 12 K before (bottom) and after (top) UV photolysis for one hour. The numbers 1-9 label IR features that appeared after photolysis, and the vibrational transitions of methanol are labeled with asterisks. The nine IR features are assigned in Table 4.1 and include the bands listed from the methane peak at 1303 cm^{-1} to the ethylene glycol peak at 867 cm^{-1}.

this procedure cannot fully confirm all unique photoproducts that were present at 12 K.

TABLE 4.1: IR assignments in the spectrum of UV-photolyzed methanol ice at 12 K

Band Position (cm^{-1})	Chemical Formula	Chemical Name	Figure 4.2 Label	Reference
2341	CO_2	Carbon dioxide	-	1
2136	CO	Carbon monoxide	-	1
1722	H_2CO	Formaldehyde	-	2, 3, 4
	CH_3CHO	Acetaldehyde	-	2, 3, 4
	$HCOOCH_3$	Methyl formate	-	2, 3, 4
1303	CH_4	Methane	1	1
1245	H_2CO	Formaldehyde	2	2, 5
	CH_3OCH_3	Dimethyl ether	2	2, 5
1197	CH_2OH	Hydroxymethyl radical	3	6
1162	$HCOOCH_3$	Methyl formate	4	4, 5
	CH_3OCH_3	Dimethyl ether	4	4, 5
1091	CH_3OCH_3	Dimethyl ether	5	5, 7, 8
	$(CH_2OH)_2$	Ethylene glycol	5	5, 7, 8
	CH_3CH_2OH	Ethanol	5	5, 7, 8
1060	CH_3CH_2OH	Ethanol	6	8
919	CH_3OCH_3	Dimethyl ether	7	5
910	$HCOOCH_3$	Methyl formate	7	4
887	$(CH_2OH)_2$	Ethylene glycol	8	7, 8
	CH_3CH_2OH	Ethanol	8	7, 8
867	$(CH_2OH)_2$	Ethylene glycol	9	7

(1) Cruz-Diaz et al. (2016) (2) Gerakines et al. (1996), (3) Hudson et al. (2000), (4) Modica et al. (2010), (5) Hudson et al. (2020), (6) Öberg et al. (2009a), (7) Hudson et al. (2005), (8) Hudson (2017).

4.3.2 Heating from 12 to 300 K

The photolyzed methanol ice samples were heated from 12 to 300 K, and IR spectra were collected every 10 K to monitor the sublimation of photoproducts and to understand the reactions that occurred during this warm-up process. No additional features were detected that were not present at 12 K, but several of them increased in peak absorbance. First, the broad peak at $\sim$ 3300 cm^{-1} (the O-H stretching region) increased in absorbance between 12 and 125 K. The absorptions of the O-H stretching region disappeared above 125 K, which is consistent with the sublimation of methanol. The absorbance increase observed could be due to radical-radical recombination that produced water and alcohols (e.g. ethanol), from the rapid crystallization of methanol when heated above $\sim$ 100 K (Luna et al., 2018), or potentially the redeposition of gases within the chamber.

Figure 4.3 shows the change in the IR spectrum as the ice was heated. The left panel shows the increase in the O-H stretch from 12 to 45 K, 45 to 85 K, and 85 to 125 K. After 125 K the absorbance decreased as the ice sublimated. The right panel shows the change in absorbance for several peaks from 1350 to 800 cm^{-1} (see Table 4.1). The features of methane (1303 cm^{-1}) and the hydroxymethyl radical (CH_2OH, 1197 cm^{-1}) decreased above 12 K. Increases in absorbance were observed at 1091,

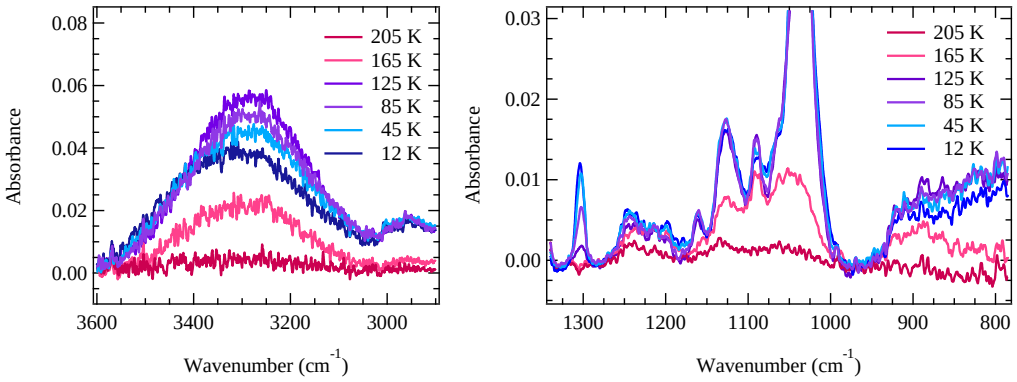

FIGURE 4.3: IR spectra of the UV photolyzed methanol ice warmed from 12 to 205 K. Left panel: 3600-2900 cm^{-1}. Right panel: 1350-800 cm^{-1}.

887, and 867 cm^{-1}, due to both ethanol and ethylene glycol (which could not be distinguished with this technique). Since ethanol and ethylene glycol form from radical recombination reactions involving the hydroxymethyl radical, this behavior of their IR features suggests that some ethanol and ethylene glycol was produced during warm-up. The peaks at 1245, 1162, and 910 cm^{-1}, assigned to dimethyl ether and methyl formate, did not increase as the ice was heated. Both products are formed via radical recombination reactions involving the methoxy radical (CH_3O), and these peaks decreased rapidly after the ice was heated above 125 K.

Mass spectra were also collected from m/z = 1 to 65 daltons in 10 K increments as the ice was warmed. Temperature-programmed desorption (TPD) curves were constructed from these data for the m/z of potential photoproducts that were not detectable by the submillimeter spectrometer (see Section 4.3.3).

4.3.3 Gas-phase Composition at 300 K

The composition of the gases from the UV-photolyzed methanol ice, after warm-up to 300 K, was determined using submillimeter/far-IR spectroscopy. First, broadband spectra were collected that focused on the detection of two of the main photoproducts of methanol ice photolysis: carbon monoxide (CO) and formaldehyde (H_2CO). From these broadband spectra, various rotational transitions were detected and were used to identify more photoproducts. After those identifications were made, targeted searches were carried out to confirm those initial broadband detections and

to search for even more products. All spectra presented in this section have been power corrected and the intensities are in units of voltage (mV) and/or temperature (K). Lastly, many of the center frequencies of the rotational transitions are labeled by dotted lines and with their respective quantum numbers as $J'_{Ka',Kc'} - J_{Ka,Kc}$.

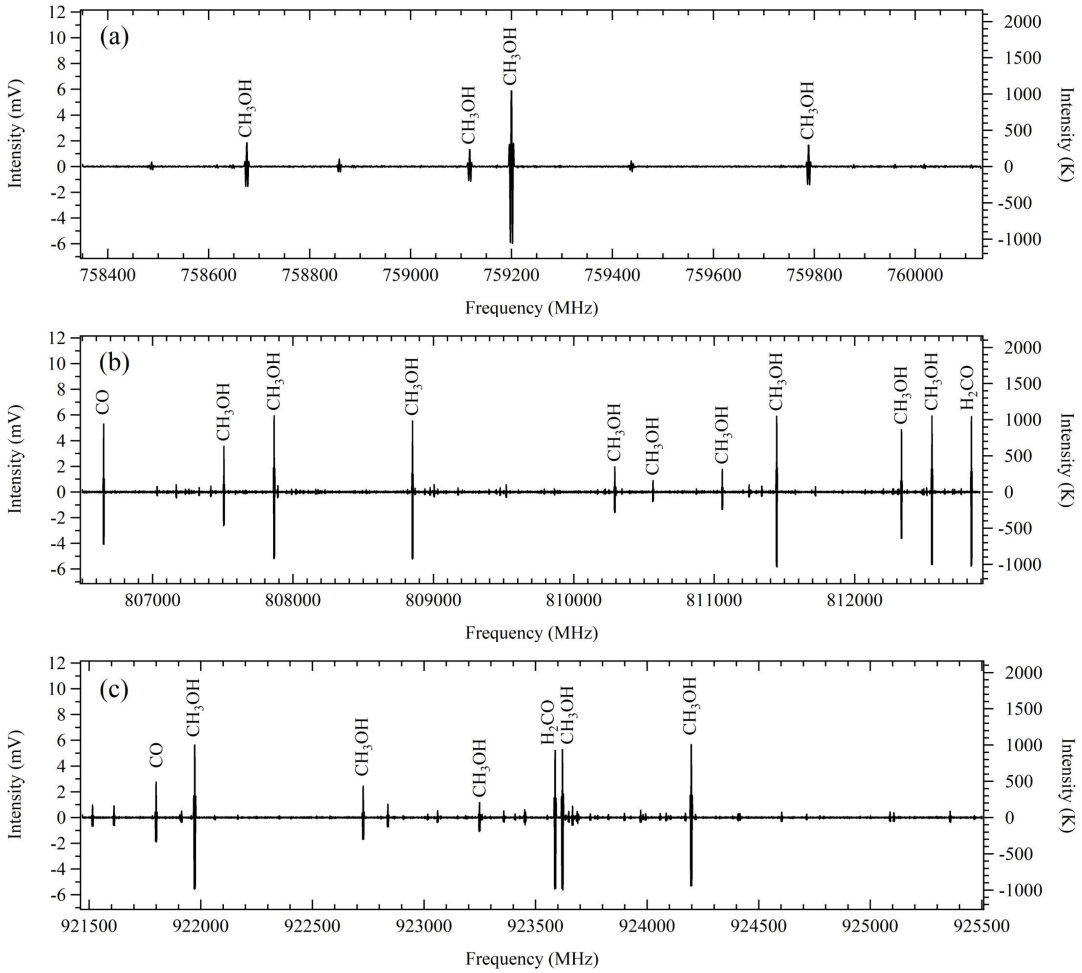

FIGURE 4.4: Broadband submillimeter/far-IR spectra at (a) 758350-760130 MHz, (b) 806500-812890 MHz, and (c) 921470-925500 MHz. Rotational transitions with an intensity greater than 1 mV are labeled with molecule name. Spectra were boxcar-smoothed with a window of 10 points to reduce noise.

Broadband spectra were collected in the ranges of 758350-760130 MHz, 806500-812890 MHz, and 921470-925500 MHz (Figure 4.4). See Appendix A.1 and Table A.1 for the assignment of the 806500-812890 MHz spectrum. These spectral windows were selected initially to detect CO and H_2CO and contained the highest power in this high-frequency submillimeter region of the spectrometer (700-1000 GHz). Two peaks were detected for CO at 806651.81 and 921799.83 MHz, and two peaks were

detected for H_2CO at 812831.41 and 923587.96 MHz.

After initial identifications were made for several molecules, spectra were then collected for targeted transitions in order to improve signal-to-noise ratio and to search for products with weaker transitions in these spectral regions. These results as well as reported photoproducts from the literature were used to make targeted searches for more molecules. In the following paragraphs, the complex organic molecules (COMs), which we define as molecules that contain two or more C-atoms, detected in the gas phase after ice warm-up are reported in order of increasing molecular weight.

Ketene C_2H_2O

Five spectral lines were detected for ketene (also referred to as ethenone), the simplest member of the ketene group. Ketene has relatively intense features at submillimeter wavelengths and was first observed in the 806500-812890 MHz broadband spectrum. All five peaks are shown in Figure 4.5.

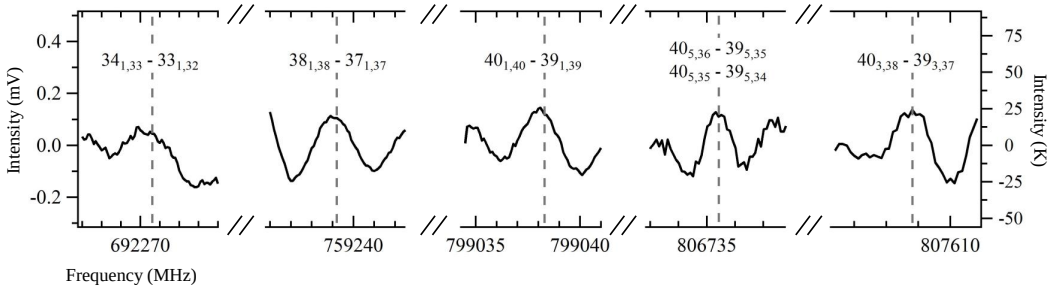

FIGURE 4.5: Five detections of ketene transitions including three peaks from the broadband scans and two additional targeted transitions. Rotational quantum numbers are labeled for each transition $J'_{Ka',Kc'}$ - $J_{Ka,Kc}$.

The C_2H_4O Isomers Acetaldehyde, Ethylene Oxide, and Vinyl Alcohol

Acetaldehyde has been previously reported as a UV photoproduct of methanol ice (Abou Mrad et al., 2016; Öberg et al., 2009a; Paardekooper et al., 2016a), but to our knowledge ethylene oxide and vinyl alcohol have not. In this study, all three of the C_2H_4O isomers were searched for and identified via detection of at least five unique rotational transitions.

Although several acetaldehyde detections were made in our broadband data, it initially was a complicated molecule to identify because many of the transition frequencies in the spectral catalog have very large uncertainties ($\geq$ 10 MHz). However, spectra were collected of an acetaldehyde standard to confirm and identify all acetaldehyde peaks in the broadband data.

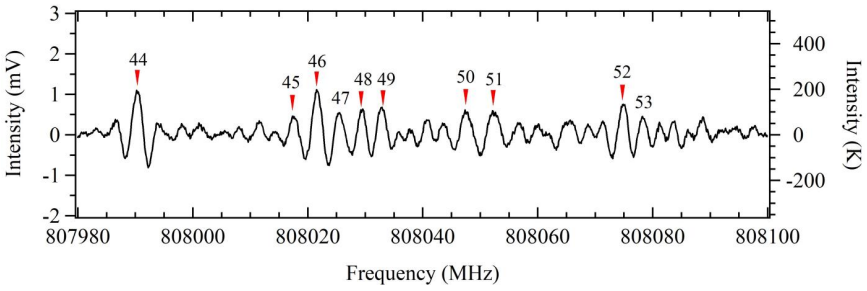

FIGURE 4.6: Eight acetaldehyde peaks from 807980 to 808100 MHz labeled with red arrows. The numbers correspond to Table A.1. For reference, the standard deviation of the noise for this spectrum was 0.1 mV making 5-σ = 0.5 mV.

A large portion of the detections for acetaldehyde were blended with neighboring peaks, and Figure 4.6 demonstrates how crowded these rotational spectra can be. Despite this, five peaks were uniquely resolved and were used for a rotational-diagram analysis to determine the temperature and density of the acetaldehyde gas present after warm-up (see Section 4.3.4).

Ethylene oxide has intense rotational features at high frequencies in the broadband scans, and a few transitions were detected that were not blended with other products. These features were then confirmed by collecting more spectral averages and searching for more transitions at other frequencies. In total, eight peaks were detected for *cis*-ethylene oxide and are shown in Figure 4.7.

The third C_2H_4O isomer is vinyl alcohol, which is considerably less stable than acetaldehyde and ethylene oxide under standard laboratory conditions. It exists in two conformational structures: *syn* and *anti*. The submillimeter/far-IR spectrum of the *anti* conformation possesses significantly stronger absorption signals than the *syn* conformer. The rotational spectrum of vinyl alcohol, in either conformation, has only been predicted below 720 GHz. Therefore, it could not be identified in the

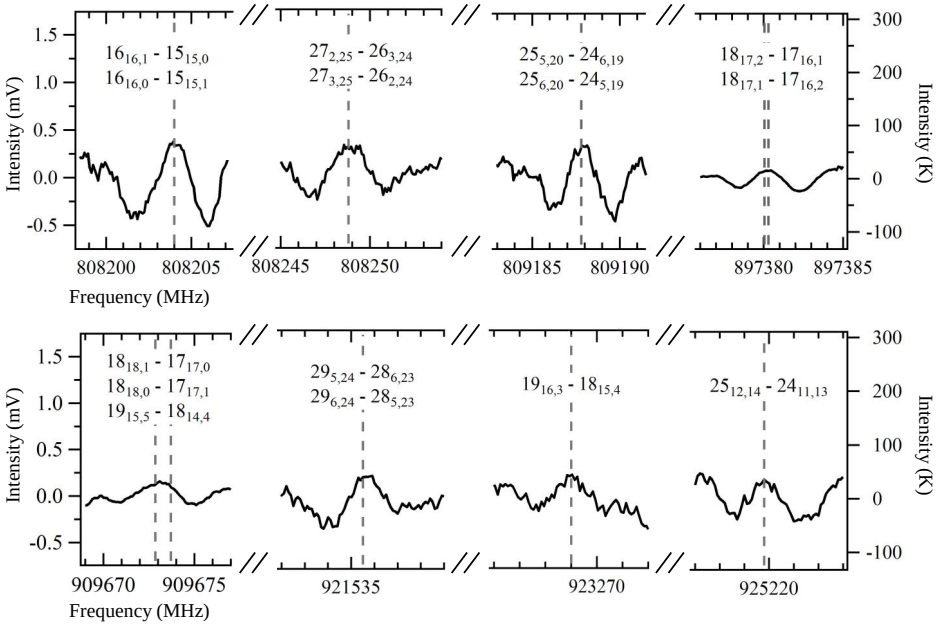

FIGURE 4.7: Eight detections of *cis*-ethylene oxide including six peaks in the broadband spectra and two targeted spectra. Rotational quantum numbers are labeled for each transition $J'_{Ka',Kc'}$ - $J_{Ka,Kc}$

broadband scans, but a targeted search was performed for five transitions of *anti*-vinyl alcohol which led to those shown in Figure 4.8.

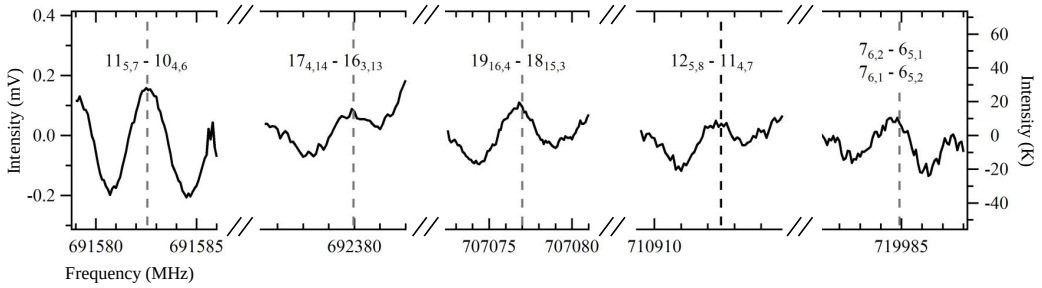

FIGURE 4.8: Five detections of *anti*-vinyl alcohol transitions from targeted submillimeter searches. Rotational quantum numbers are labeled for each transition $J'_{Ka',Kc'}$ - $J_{Ka,Kc}$.

The C_2H_6O Isomers Ethanol and Dimethyl Ether

The two C_2H_6O isomers ethanol and dimethyl ether have been reported previously as methanol ice photoproducts (Öberg et al., 2009a; Paardekooper et al., 2016a; Schneider et al., 2019). Both the *trans* and *gauche* forms of ethanol were prominent in the

broadband spectra measured here. Figure 4.9 shows ten transitions that were detected for *trans*-ethanol. The *trans*-conformation is the most stable configuration, and its rotational transitions are more intense than those of the *gauche*-conformation.

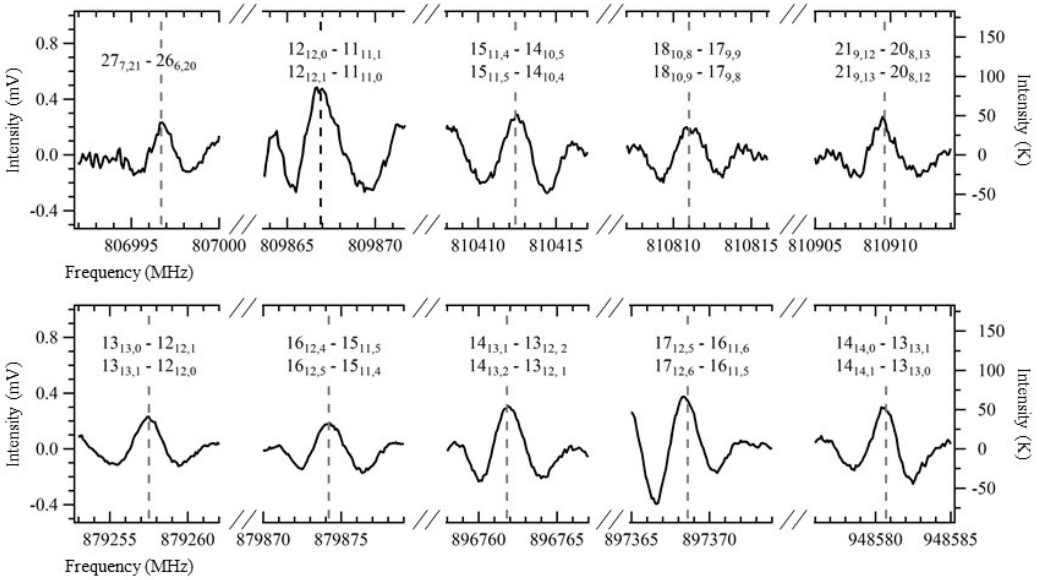

FIGURE 4.9: Ten detections of *trans*-ethanol transitions including five peaks from the 806500-812890 MHz scan (top row) and five separate targeted transitions (bottom row). Rotational quantum numbers are labeled for each transition $J'_{Ka',Kc'}$ - $J_{Ka,Kc}$.

It was not clear initially whether *gauche*-ethanol would be detected. After the notably significant abundance of *trans*-ethanol was observed, a search for *gauche*-ethanol was conducted, and nine non-blended detections were confirmed (Figure 4.10).

Searches were also conducted for the second C_2H_6O isomer, dimethyl ether. Five absorption signals were detected in the broadband scans (Figure 4.11). The structure of dimethyl ether contains two methyl rotors which results in transitions to be split into four substates (*EE*, *EA*, *AA*, and *AE*). Therefore, the rotation diagram analysis required determination of the separate components of the peak areas for each of these blended transitions. The individual peak areas were found by first integrating the 2f line shape twice to convert it to a Gaussian line shape, and then fitting individual Gaussian peaks for the blended transitions using the multipeak fitting function within the IGOR Pro software package. The rotation diagram analysis results are presented in Section 4.3.4.

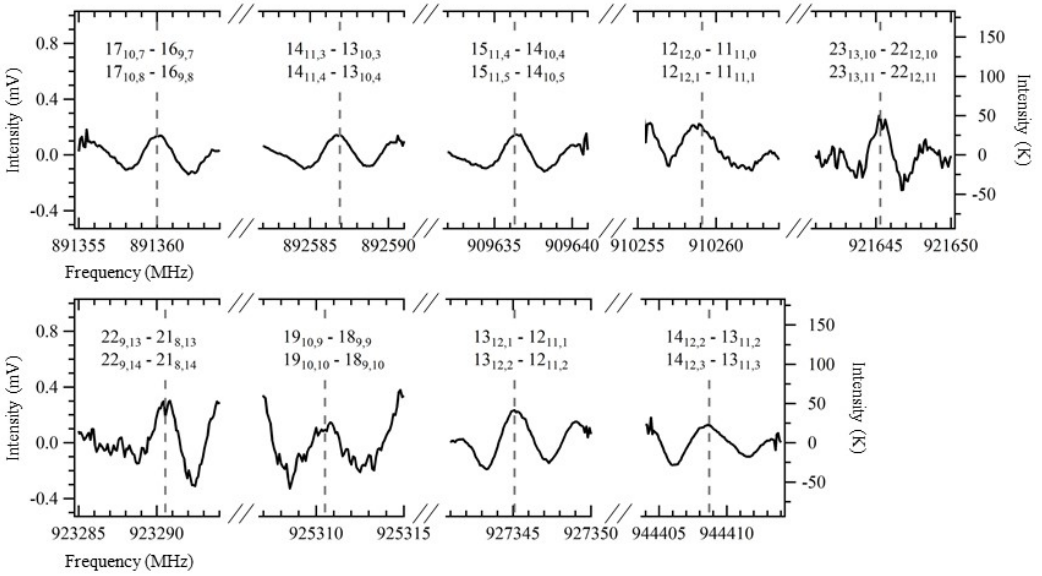

FIGURE 4.10: Nine detections of *gauche*-ethanol transitions including three peaks detected in the 921470-925500 MHz scan and six peaks from separate targeted searches. Rotational quantum numbers are labeled for each transition $J'_{Ka',Kc'}$ - $J_{Ka,Kc}$.

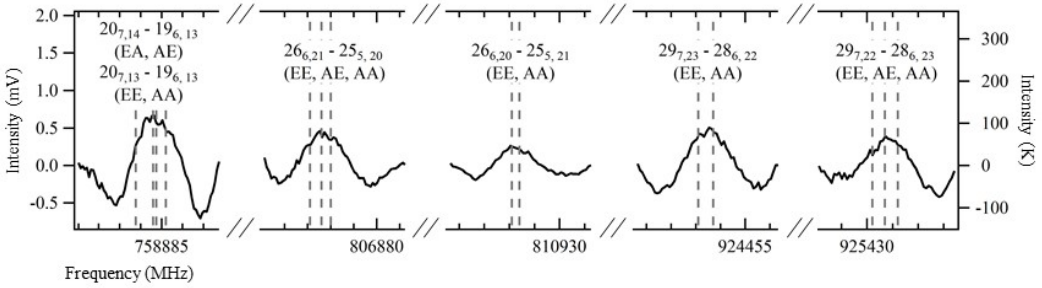

FIGURE 4.11: Five detections of dimethyl ether in the broadband scans. Rotational quantum numbers are labeled for each transition $J'_{Ka',Kc'}$ - $J_{Ka,Kc}$.

The $C_2H_4O_2$ Isomers Methyl Formate, Glycolaldehyde, and Acetic Acid

The $C_2H_4O_2$ isomers have been reported previously as UV photoproducts of methanol ices (Öberg et al., 2009a), but they cannot be uniquely identified in either IR or mass spectra because their signatures are too similar. Acetic acid and methyl formate have been reported as UV photoproducts of methanol ice by gas chromatography coupled with mass spectrometry, but glycolaldehyde could not be detected due to the analytical setup (Abou Mrad et al., 2016). These three isomers can be distinguished and quantified with the techniques implemented in this study, and searches for all three were successfully conducted.

Methyl formate has two conformations: *cis* and *trans*. The most stable conformation is *cis*, and six transitions were detected for *cis*-methyl formate from targeted searches (Figure 4.12). We were not able to search for the *trans*-conformer because the submillimeter spectrum of *trans*-methyl formate has yet to be measured experimentally.

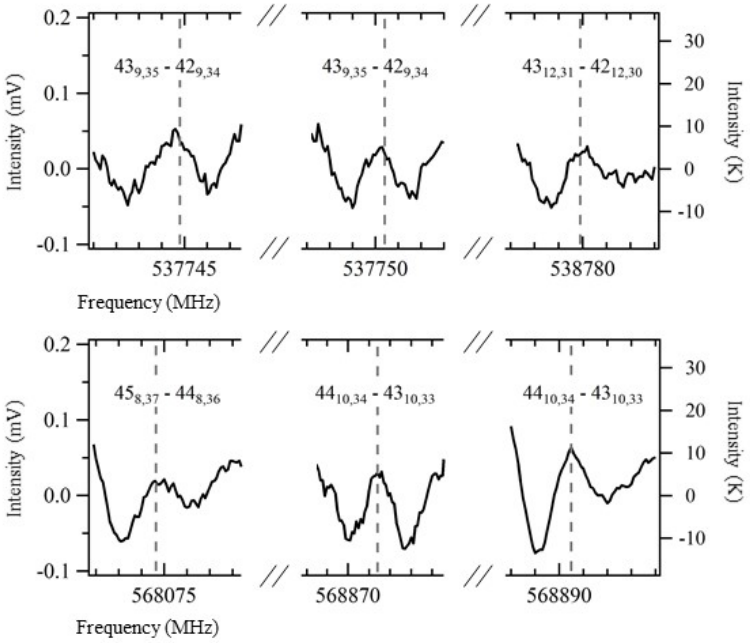

FIGURE 4.12: Six detections of *cis*-methyl formate from targeted searches. Rotational quantum numbers are labeled for each transition $J'_{Ka',Kc'}$ - $J_{Ka,Kc}$.

Nine transitions were detected for glycolaldehyde (Figure 4.13). Unlike methyl formate, glycolaldehyde has significantly stronger transitions within the broadband scan frequencies arising from its stronger dipole moment and lack of internal rotation.

Searches were also conducted for the third $C_2H_4O_2$ isomer, acetic acid. Four peaks were detected near the center frequencies of acetic acid at levels $\geq 5\ \sigma$, but three other peaks of similar intensity were not detected. The most intense transitions of acetic acid are even lower in intensity than those of methyl formate and significantly lower in intensity than those of glycolaldehyde. Consequently, the detection limit of acetic acid is higher than the detection limits of the other two isomers. A rotation diagram analysis was performed for the four detections, but gave unrealistic values for temperature and density. Therefore, acetic acid was not confirmed as a

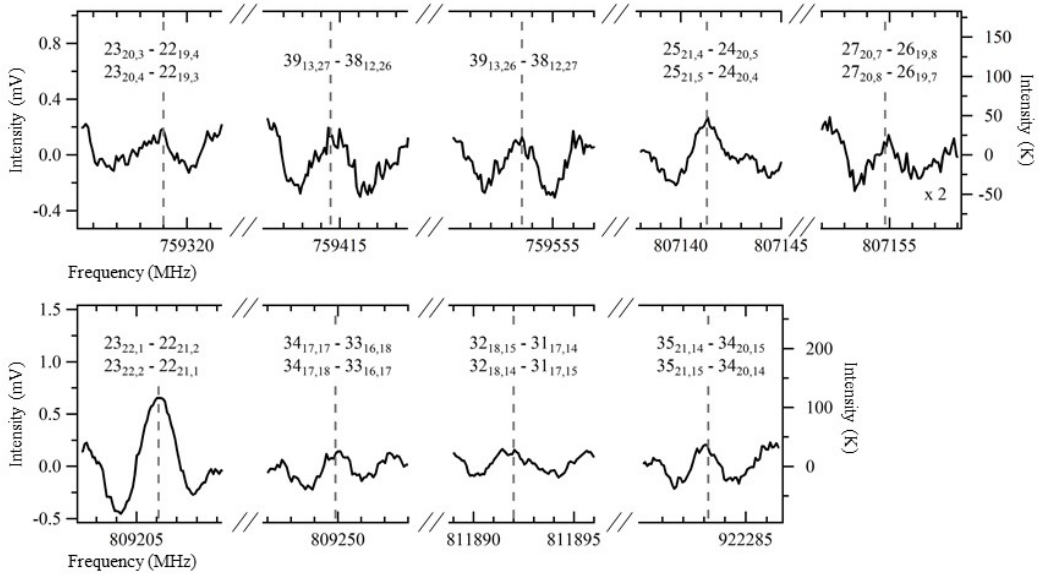

FIGURE 4.13: Nine detections of glycolaldehyde in the broadband submillimeter spectra. The intensity of the peak at 807155 MHz was multiplied by two for visibility. Rotational quantum numbers are labeled for each transition $J'_{Ka',Kc'}$ - $J_{Ka,Kc}$.

photoproduct. If it was present, then its concentration was below the detection limit of the spectrometer.

The $C_2H_6O_2$ Isomers Ethylene Glycol and Methoxymethanol

Two $C_2H_6O_2$ isomers, ethylene glycol and methoxymethanol, have both been reported previously as UV-photoproducts of methanol ice and were therefore considered in this study (Paardekooper et al., 2016a; Schneider et al., 2019). Furthermore, IR features that aligned with those of ethylene glycol were present in the FTIR spectra at 12 K (see Figure 4.2 and Table 4.1). The most stable conformation of ethylene glycol, *aGa'*, was targeted based on the recent submillimeter assignment published by Melosso et al. (2020). Searches for nine transitions were conducted in this study. Out of those nine transitions, only two clear detections were made. Four more peaks that were targeted showed significant blending with neighboring photoproduct transitions and were not individually resolved. The remaining three searches for transitions of similar intensities resulted in non-detections. Therefore, ethylene glycol could not be confirmed as a photoproduct in these experiments.

Methoxymethanol has a straightforward formation pathway from the recombination of the methoxy and hydroxymethyl radicals. Unfortunately, the detection limit for methoxymethanol at submillimeter wavelengths is quite high, and it was not detected in these experiments. Both $C_2H_6O_2$ isomers were searched for in the mass spectral data from TPD curves of m/z = 61 and 62. There were no signals present at these m/z at the appropriate desorption temperatures, $\sim$ 155 K for methoxymethanol (Schneider et al., 2019) and $\sim$ 185 K for ethylene glycol (Öberg et al., 2009a). The lack of production of these two COMs may be due to the differences in ice temperature during photolysis. The studies conducted by Schneider et al. and Öberg et al. reported one or both of these products at photolysis temperatures of 90 and 70 K, respectively.

Acetone $(CH_3)_2CO$

The molecule with the largest number of atoms that was detected in this study was acetone. The submillimeter spectrum of acetone has relatively weak absorption signals (due to its two methyl rotors that cause torsional splitting into four substates), resulting in a relatively high detection limit. Acetone has been reported by others as a radiation product of methanol ice (Abou Mrad et al., 2016; Henderson et al., 2015; Öberg et al., 2009a) and controversially as a non-product of proton-irradiated H_2O + CH_3OH ice (Hudson et al., 2000). Three non-blended detections were made for acetone in this study (Figure 4.14) while other transitions for which we searched were overwhelmed by intense, neighboring methanol transitions.

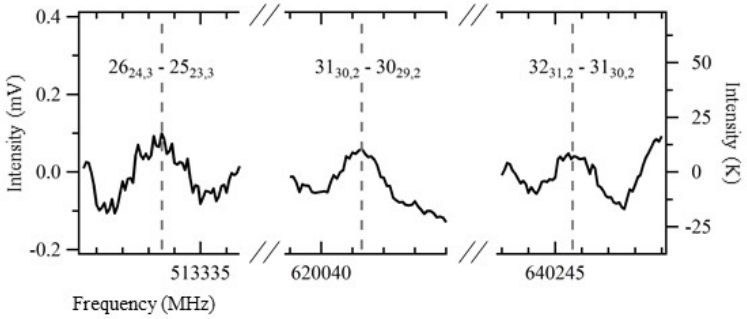

FIGURE 4.14: Three detections of acetone transitions from targeted searches. Rotational quantum numbers are labeled for each transition $J'_{Ka',Kc'}$ - $J_{Ka,Kc}$.

4.3.4 Rotation Diagram Analysis Procedure and Results

A rotation diagram analysis can be used to determine the rotational temperatures and densities of molecules from the integrated intensities of their respective rotational transitions. This process is also commonly referred to as Boltzmann analysis or population diagram analysis, which is described (along with the underlying physics) by Goldsmith et al. (1999) and references therein. This technique has been widely used by astronomers for determining temperature and density of molecules detected in observational data, and Laas et al. (2013) showed that it also could be adapted for use in laboratory absorption spectroscopy studies like those performed here. The application of the rotation diagram approach by Laas et al. only considered optically thin transitions and cannot be used to quantify all observed products in our experiments. In the present work, the Laas et al. technique was adapted to include the full treatment as laid forth by Goldsmith et al. using a Python3 program.

The rotation diagram analysis utilizes the following equation

$$\ln\left(\frac{8\pi k\nu^2}{hc^3 A_{ul}}\frac{W}{g_u}\right) = \ln\left(\frac{N}{Z}\right) - \frac{E_u}{kT} - \ln(C_\tau), \tag{4.1}$$

where W is the integrated intensity[4], ν is the center frequency of the transition, A_{ul} is the Einstein A-coefficient for the transition, g_u is the upper-state degeneracy, N is the total column density, Z is the partition function (i.e., the sum of densities of states), E_u is the upper-state energy, T is the rotational temperature, C_τ is an optical depth (τ) correction factor, k is Boltzmann's constant, h is Planck's constant, and c is the speed of light. For simplicity, we define γ to be equal to $8\pi k\nu^2/hc^3 A_{ul} g_u$. The best-fitting slope and y-intercept of a plot of $\ln(\gamma W C_\tau)$ vs. E_u can then be used to determine T and N according to equation 4.1.

The optical depth correction factor is given by

$$C_\tau = \frac{\tau}{1 - e^\tau} \tag{4.2}$$

[4]The integrated intensity, W, was determined using the composite Simpson's rule. The integration range was the frequency range that covered the 2f line shape, and the negative area of the side lobes was added to the positive area of the center peak.

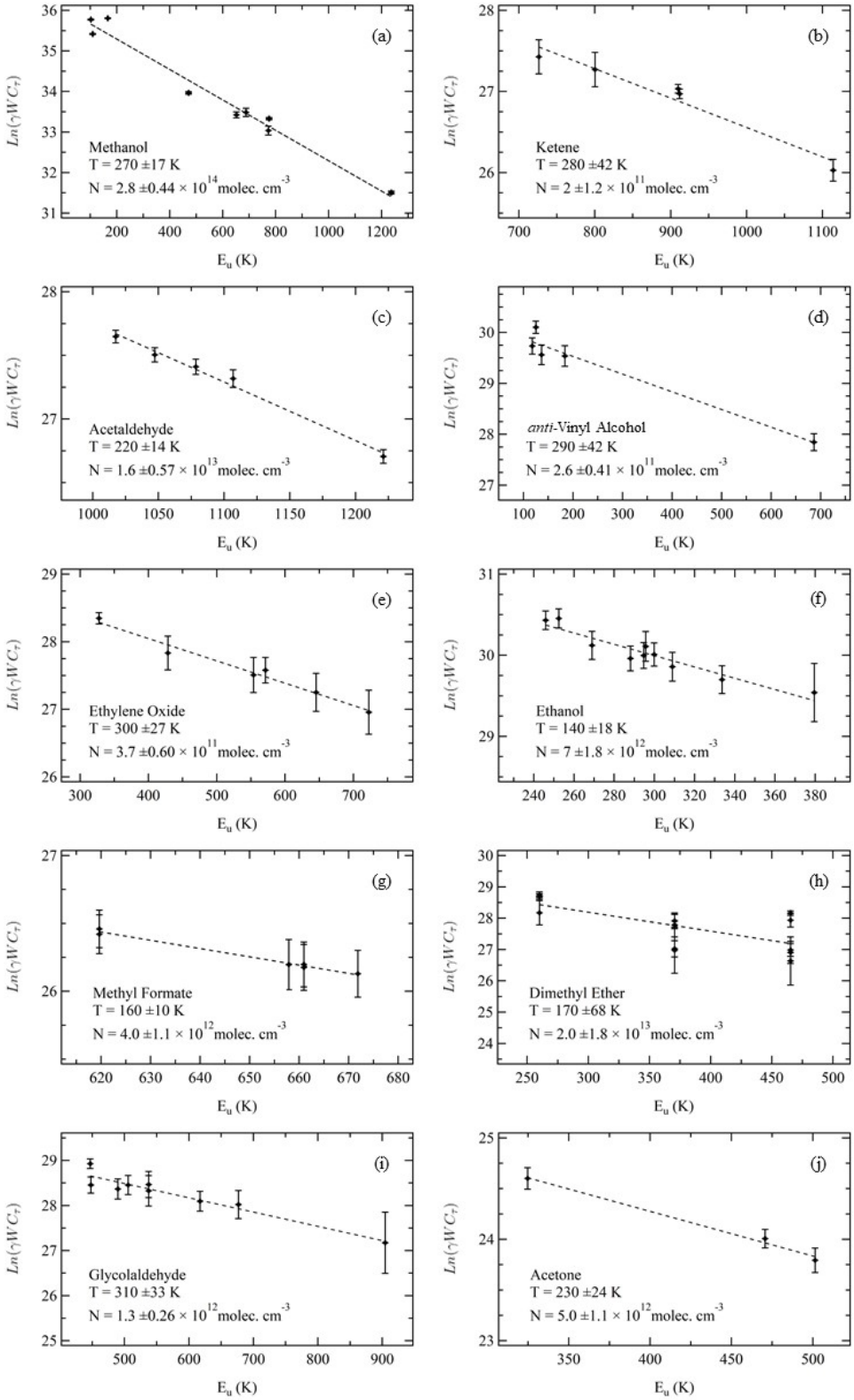

FIGURE 4.15: Rotation diagrams of (a) methanol, (b) ketene, (c) acetaldehyde, (d) ethylene oxide, (e) *anti*-vinyl alcohol, (f) ethanol, (g) dimethyl ether, (h) methyl formate, (i) glycolaldehyde, (j) acetone. Errors are described in Section 4.3.4.

$$\tau = \frac{h}{\Delta v} N_u B_{ul} \left(e^{\frac{hv}{kT}} - 1 \right) \tag{4.3}$$

$$N_u = \frac{N}{Z} g_u e^{\frac{-E_u}{kT}} \tag{4.4}$$

where Δv is the FWHM of the peak, N_u is the upper-state density, and B_{ul} is the Einstein B-coefficient calculated according to

$$B_{ul} = \frac{A_{ul} c^3}{8\pi h v^3}, \tag{4.5}$$

and for laboratory spectra, as presented herein, the Einstein A-coefficient is calculated from

$$A_{ul} = (2.7964 \times 10^{-16}) I_{cat}(T) v^2 \left(\frac{Z}{g_u} \right) \left(e^{\frac{-E_l}{kT}} - e^{\frac{-E_u}{kT}} \right)^{-1} \tag{4.6}$$

where $I_{cat}(T)$ is the temperature dependent catalog intensity value and E_l is the lower-state energy. The values needed for all calculations (i.e., $I_{cat}(T), E_l, E_u, g_u, Z$) can be found in the spectral catalog files for the molecule(s) of interest (e.g., JPL and/or CDMS catalogs).

A few conversions are needed to adapt the analysis for use with the laboratory spectra in this work. First, the peak intensity is converted from volts to Kelvin. This was achieved by converting the voltage output from the detector to Watts by dividing the voltage by the detector's optical responsivity (170 kV W^{-1}). The power was then converted to Kelvin by dividing power by the product of the detector bandwidth with Boltzmann's constant. Secondly, the peak width (Δv) refers to the FWHM of a Gaussian line shape in velocity units. Due to the 2f line shapes, a FWHM cannot be directly determined from the raw spectra, but it can be calculated because the line shape is simply the second derivative of a Gaussian line shape. Therefore, the respective peak widths are

$$w_{2f} = 2\sqrt{3} w \tag{4.7}$$

$$w_{FWHM} = 2\sqrt{2\ln(2)}w \tag{4.8}$$

where w_{2f} is the peak width of the 2f line shape between the side lobe minima, w is a line width factor, and w_{FWHM} is the FWHM of the Gaussian line shape. Next, the line width units were converted to velocity units by dividing w_{FWHM} by the center frequency, v, and multiplying by the speed of light, c.

The uncertainty of $\ln(\gamma WC_\tau)$ (i.e., the y-axis error bars) was determined based on the propagation of errors that considered the uncertainties of the peak area, center frequency, and the Einstein A-coefficient. The peak area uncertainty was calculated via error propagation using the values of the standard deviation of the noise and the uncertainty of the center frequency for each peak. The standard deviation of the noise was calculated for each line from the neighboring spectral baseline values, and the center frequency uncertainty was set to the spectral resolution, 0.1 MHz. The reported uncertainties on the temperatures derived from the analysis are calculated directly from the fits to the datasets. The uncertainty of the Einstein A-coefficient considered the uncertainties of center frequency and peak intensity. The rotation diagrams for methanol and the reported complex organic products are presented in Figure 4.15, which are labeled with the molecule's name and the calculated rotational temperature and gas density. A summary of the results can be found in Table 4.2 which includes the calculated temperatures, calculated densities, and abundance ratios of product normalized to methanol. See Appendix A.2 and Table A.2 for the parameters used for the rotation diagram analysis of each molecule.

Before the experiments were conducted, it was unclear whether the rotational temperatures would reflect room/chamber temperature ($\sim$ 298 K) or if they would be related to the volatilities of the individual molecules. The former case was observed, within experimental error, for four products: ketene, ethylene oxide, *anti*-vinyl alcohol, and glycolaldehyde. In fact, glycolaldehyde was the warmest product at 310 $\pm$ 42 K. The second-highest temperature belonged to ethylene oxide. Glycolaldehyde and ethylene oxide are known to sublimate rapidly at temperatures more than 100 K colder than their observed rotational temperatures. The coldest molecule was ethanol at 140 $\pm$ 18 K, followed by its structural isomer dimethyl ether at 170 $\pm$

TABLE 4.2: Summary of Rotation Diagram Analyses Results

Molecule	Temperature (K)	Density (10^{11} molec. cm^{-3})	Abundance Ratio
Methanol	270 ± 17	2800 ± 440	1.0000
Ketene	280 ± 42	2 ± 1.2	0.0007
Acetaldehyde	220 ± 14	160 ± 57	0.0571
Ethylene oxide	300 ± 27	3.7 ± 0.6	0.0013
anti-Vinyl alcohol	290 ± 42	2.6 ± 0.41	0.0009
Ethanol	140 ± 18	70 ± 18	0.0250
Dimethyl ether	170 ± 68	200 ± 180	0.0714
Methyl formate	160 ± 10	40 ± 11	0.0143
Glycolaldehyde	310 ± 42	13 ± 3.2	0.0046
Acetone	230 ± 24	50 ± 11	0.0179

Note: Abundance ratios are normalized to methanol. The methanol gas density includes non-irradiated methanol desorbed from the substrate, the cryostat shaft, and the chamber walls and any methanol that was reformed during the ice warm-up.

68 K. This rotational temperature agrees well with ethanol's known volatility, while the rotational temperature of dimethyl ether, 170 ± 68 K, was significantly higher than would be predicted based on volatility alone. Considering structural isomers, the rotational temperatures of ethylene oxide and *anti*-vinyl alcohol were within 10 K. The third C_2H_4O isomer, acetaldehyde, had a much lower rotational temperature. The rotational temperatures of the C_2H_6O isomers, ethanol and dimethyl ether, had a difference of 30 K with dimethyl ether being the warmer isomer. Lastly, the $C_2H_4O_2$ isomers, methyl formate and glycolaldehyde, had significantly different temperatures. Glycolaldehyde was almost twice as warm as methyl formate. No clear overall trends can be deduced from the temperatures derived in this work and further studies need to be conducted to reveal more information about rotational temperatures of species desorbed from ices.

The three most-abundant COMs were dimethyl ether, acetaldehyde, and ethanol, in order of decreasing abundance. Acetaldehyde was the most abundant C_2H_4O isomer and *anti*-vinyl alcohol was the least abundant, which follows observational trends (see Section 4.4.1). Dimethyl ether was the most abundant C_2H_6O isomer above ethanol. Lastly, methyl formate was the most abundant $C_2H_4O_2$ isomer followed by glycolaldehyde which also matches well with observations (see Section 4.4.1). The three least-abundant products that were within the detection limits of the spectrometer were ketene, *anti*-vinyl alcohol, and ethylene oxide. This was not a surprise considering these three species require multi-step formation mechanisms

beyond radical-radical recombination reactions (e.g., hydrogen abstraction(s) from ethanol). The following section contains a more in-depth discussion of the abundance ratios found in this study.

4.4 Discussion

4.4.1 The Benefits of Utilizing Submillimeter/far-IR Spectroscopy to Identify Products of Sublimated Astrophysical Ices

Submillimeter/far-IR spectroscopy is a powerful technique for identifying components of complex gas mixtures. The three main benefits that submillimeter/far-IR spectroscopy provides for laboratory ice experiments are (1) the direct comparison of laboratory spectra with submillimeter/far-IR spectra collected via telescopes, (2) the straightforward identification of structural isomers, conformers, and isotopologues, and (3) experimental quantification of uniquely identified COMs to compare to astrochemical models of the ISM and planetary atmospheres. A few limitations should be noted along with the benefits of this technique. Any gas-phase experiment within a vacuum chamber must deal with interactions with the chamber walls: (1) the detected gas densities are affected by adsorption onto the walls, and (2) the chamber walls can act as a catalytic surface for reactions that can modify the gas composition. It also should be noted that the species detected via submillimeter/far-IR spectroscopy cannot be directly distinguished as ice-phase photolysis products. The experiment focused on products detected after the warm-up of a photolyzed methanol ice. Despite these limitations, which apply to all laboratory studies of gases sublimated from ice analogs, rotational spectroscopy remains a very powerful tool in the identification of products of these photolyzed ice samples.

Direct Comparison to Submillimeter/Far-IR Telescope Data

The spectrometer that was built for this experiment covers the same regions of the electromagnetic spectrum as several millimeter/submillimeter/far-IR telescopes (e.g.,

ALMA, SOFIA, NOEMA, *Herschel*/HIFI). Figure 4.16 demonstrates how the laboratory spectra of gases sublimated from an ice sample can be compared to observational surveys such as that of Orion Kleinmann-Low (Orion-KL) collected with the HIFI instrument on the *Herschel Space Observatory*.

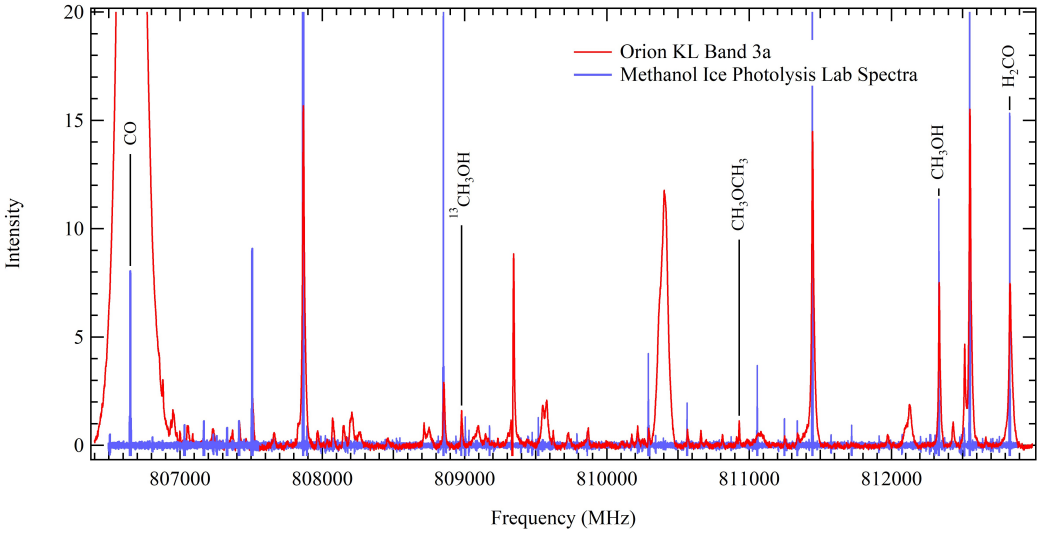

FIGURE 4.16: Overlaid spectra of the 806500-812890 MHz laboratory scan (blue) and a HIFI band 3a survey of Orion-KL (red). The intensities of the laboratory spectra were scaled down by three orders of magnitude for visual comparison. The Orion-KL spectral data were downloaded from the *Herschel* Science Archive and were first published by Crockett et al. (2014).

The red observational spectra in Figure 4.16 contain several transitions that overlap with the blue laboratory spectra of the gases desorbed from the UV-photolyzed methanol ice. Five emission features are labeled with their assigned molecules including methanol ($^{12}CH_3OH$ and the less abundant isotopologue $^{13}CH_3OH$), carbon monoxide (CO), dimethyl ether (CH_3OCH_3), and formaldehyde (H_2CO). The majority of the intense overlapping transitions present in Figure 4.16 were from $^{12}CH_3OH$. The agreement between these spectra demonstrates how laboratory ice experiments can be used to model formation mechanisms and physical parameters (e.g., temperature and density) of species detected in star-forming regions, such as Orion-KL, and other astrophysical/planetary environments.

Detection and Quantification of Structural Isomers, Conformational Isomers, and Isotopologues

The identification of structural isomers, conformational isomers (conformers), and isotopologues detected in a single gas mixture is straightforward when utilizing submillimeter/far-IR spectroscopy as the main detection method, and this study has demonstrated the unique direct detections of structural isomers, conformers, and isotopologues that were desorbed from a UV-photolyzed methanol ice. The structural isomers that were detected included three C_2H_4O isomers (acetaldehyde, ethylene oxide, and vinyl alcohol), two C_2H_6O isomers (ethanol and dimethyl ether), and two $C_2H_4O_2$ isomers (methyl formate and glycolaldehyde). The detection of the *trans* and *gauche*-conformers of ethanol demonstrated the ability to distinguish a single chemical component in two different conformations. Lastly, $^{13}CH_3OH$, the rarer isotopologue of methanol, was detected in the broadband spectra showing the capability for isotopologue detection. None of these isomers could be distinguished using mass spectrometry alone in the desorbed gas sample.

Not only does rotational spectroscopy provide an in-situ measurement featuring the unique rotational fingerprints of the molecules in a given gas mixture, those components can also be quantified in the sample directly through a rotation diagram analysis without the need for further chemical separation or manipulation. The quantification of structural isomers, conformers, and/or isotopologues can even be achieved from a single spectrum. In this study, unstable species such as the hydroxymethyl (CH_2OH) and methoxy (CH_3O) radicals are not present after warm-up because they immediately recombine to form stable products. However, future studies will aim to determine the yields of unstable products that photodesorb from the ice surface at low temperatures (10-20 K) such as those found in various astrophysical environments such as cold dense clouds.

4.4.2 Methanol Branching Ratio Implications

The photodissociation branching ratios of methanol are still unknown and are key to understanding COM formation on and within icy objects. Nonetheless, a few

assumptions can be inferred from the relative abundances of the complex organics detected in this study. First, the most abundant product was dimethyl ether, CH_3OCH_3, which may form from the radical-radical recombination of CH_3 + OCH_3, while its structural isomer, ethanol CH_3CH_2OH, likely forms from the radical-radical recombination of CH_3 + CH_2OH. Dimethyl ether had a much higher density than ethanol after ice warm-up, which implies that the H + CH_3O radicals are formed in larger quantity than the H + CH_2OH radicals. The larger abundance of methyl formate ($HCOOCH_3$) versus glycolaldehyde ($HOCH_2CHO$) provides further evidence for this claim as methyl formate requires the CH_3O radical and glycolaldehyde requires the CH_2OH radical for formation. Even more evidence for CH_3O being the dominant methanol photoproduct is provided by the non-detection of ethylene glycol, $(CH_2OH)_2$, which requires two CH_2OH radicals for formation. The computational study by Laas et al. (2011) showed the dependence of the $C_2H_4O_2$ isomer abundances on methanol ice photolysis branching ratios. Their results showed that to reproduce methyl formate abundances detected in Sagittarius B2(N), the H + CH_3O pathway must be favored over the H + CH_2OH pathway, consistent with the findings of this work. Furthermore, the branching ratios that had the worst agreement with the observed abundances of methyl formate, glycolaldehyde, and acetic acid were those which favored the H + CH_2OH pathway. The details of these reaction mechanisms are still a work in progress and will require additional experiments with isotopic labeling and confirmation of radicals from sublimation. Although the results in this study seem to support theoretical claims, this is in contradiction to the previous experimental study by Öberg et al. (2009a) which determined the formation of H + CH_2OH to be five times that of H + CH_3O. This previous experimental work relied on IR spectra of the ices and mass spectrometric analysis of the gas phase material during warm-up. Further studies both experimentally and theoretically are needed to verify the actual mechanisms at work. Regardless, this highlights the complementary strength brought to laboratory ice experiments by combining standard techniques with rotational spectroscopy.

4.4.3 Astrophysical Implications

All products reported herein originated from the UV photolysis and subsequent warm-up of a methanol ice. Those products included carbon monoxide, carbon dioxide (detected by FTIR spectroscopy), methane (detected by FTIR spectroscopy), formaldehyde, ketene, acetaldehyde, ethylene oxide, vinyl alcohol, ethanol, dimethyl ether, methyl formate, glycolaldehyde, and acetone. To our knowledge, this is the first study that reports ketene, ethylene oxide, and vinyl alcohol as products of a methanol ice photolysis and sublimation experiment. The production of these species should therefore be considered in computational astrochemical models of star formation and planetary atmospheres. Ketene has been reported previously by Maity et al. (2015) as a product from ion-processing of methanol ice, and vinyl alcohol was reported as a tentative detection in the same study. Future studies are required to determine probable formation mechanisms for these three species from the UV-photolysis of methanol.

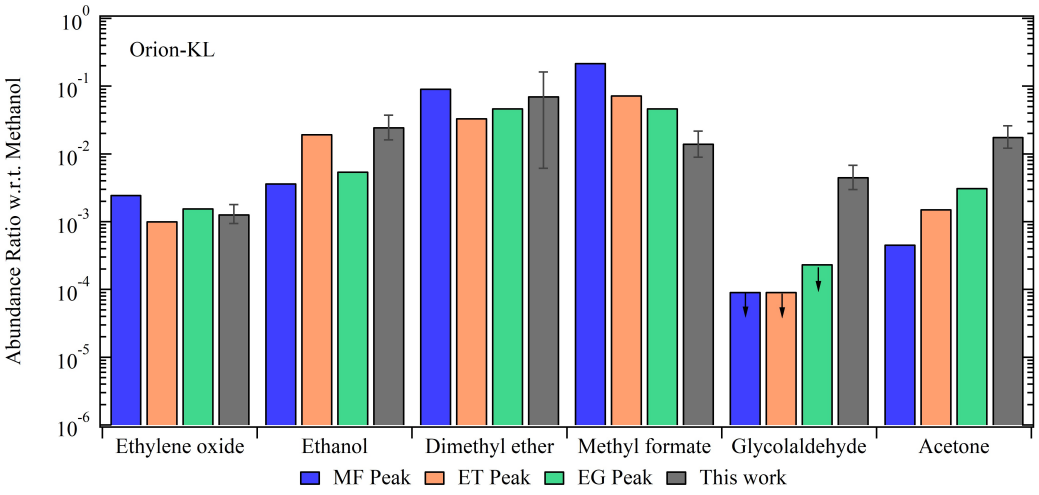

FIGURE 4.17: Abundance ratios of COMs relative to methanol as detected toward the high-mass protostar Orion-KL in three regions (MF peak, ET peak, and EG peak) compared to the laboratory results from this study. Observations from Tercero et al. (2018).

The abundance ratios of the detected photoproducts with respect to methanol were compared to those detected in a high-mass protostar Orion-KL (Tercero et al., 2018), low-mass protostar IRAS 16293-2422(B) (Drozdovskaya et al., 2019), Sagittarius B2 (N) (Belloche et al., 2013), comet C/2014 Q2 (Lovejoy), hereafter Lovejoy, (Biver et al., 2019), and comet 67P/Churyumov-Gerasimenko, hereafter 67P/CG

(Rubin et al., 2019a). Several trends were noticed between these abundance ratios in the various astronomical sources. Figure 4.17 shows abundance ratios of ethylene oxide, ethanol, dimethyl ether, methyl formate, glycolaldehyde, and acetone normalized to methanol as detected in Orion-KL in three different regions. The methyl formate peak (MF peak), ethanol peak (ET peak), and ethylene glycol peak (EG peak) regions were described and mapped by Tercero et al. (2018). The MF peak is located in the compact ridge and the ET and EG peaks are located closer to the hot core. The abundance ratios of these three regions were similar across all molecules. The laboratory results from this study are compared to these observational findings and are shown in gray in Figure 4.17. The abundance ratios from this study appear to be most similar to the EG peak abundances, thus simulate the chemistry occurring closer to the hot core where thermal reactions play a large role, and are less similar to the compact ridge where it is colder. The laboratory results over-produced glycolaldehyde and acetone, and under-produced methyl formate. There are various details that can be further studied to help explain this, but most likely there is inconsistency for these species due to ice composition, photolysis timescales, and other energetic processes that were not considered in this study. Further experiments are required to constrain these details, though this initial work is very intriguing.

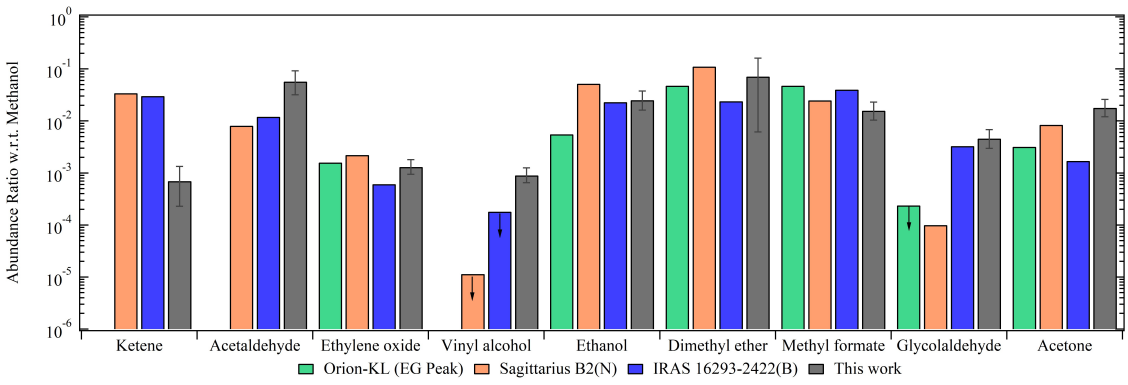

FIGURE 4.18: Abundance ratios of COMs relative to methanol as detected towards hot cores Orion-KL (EG peak), Sagittarius B2(N), IRAS 16293-2422(B) compared to the laboratory results from this study. Observations from Belloche et al. (2013) and Tercero et al. (2018), and Drozdovskaya et al. (2019). Arrows denote upper limit detections.

Figure 4.18 shows the abundance ratios of ketene, acetaldehyde, ethylene oxide, vinyl alcohol, ethanol, dimethyl ether, methyl formate, glycolaldehyde, and acetone

normalized to methanol as detected in high-mass protostar Orion-KL (EG peak), protocluster Sagittarius B2(N), and low-mass protostar IRAS 16293-2422(B). The laboratory abundance ratios from this work are shown in gray. Overall, the laboratory results appear most similar to the abundance ratios found in the low-mass protostar IRAS 16293-2422(B). This could be because the warm-up rate and UV fluence of these experiments better models a low-mass protostar than a high-mass protostar. Secondly, there are several gas-phase destruction pathways that further alter the abundances during the longer warm-up timescales of high-mass protostars. For example, the cosmic ray ionization rates (Bonfand et al., 2019) are likely an important factor that is not included in the current study.

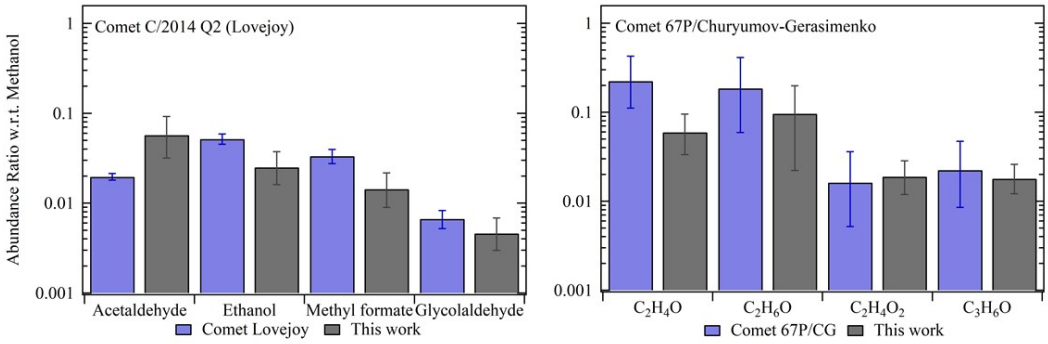

FIGURE 4.19: Abundance ratios of COMs relative to methanol as remotely detected towards Comet C/2014 Q2 (Lovejoy) (left, Biver et al. (2019)) and through the ROSINA mass spectrometer on the Rosetta mission in Comet 67P/Churyumov-Gerasimenko (right, Rubin et al. (2019a)) compared to the laboratory results from this study.

A comparison of the abundance ratios for acetaldehyde, ethanol, methyl formate, and glycolaldehyde as detected in Comet Lovejoy and this study can be found in Figure 4.19 (left panel). Similar trends for all molecules are observed. The exception is acetaldehyde, which was over-produced in the laboratory results of this study. The right panel of Figure 4.19 shows a comparison of isomer abundance ratios detected in Comet 67P/CG and those from this study. The abundance ratios for Comet 67P/CG were compared by the total isomer abundances because the Rosetta Spectrometer for Ion and Neutral Analysis (ROSINA) separates by mass and could not uniquely quantify structural isomers of these organics. Therefore, the C_2H_4O isomers included, but were not limited to: acetaldehyde, ethylene oxide, and vinyl

alcohol; the C_2H_6O isomers included ethanol and dimethyl ether; the $C_2H_4O_2$ isomers included methyl formate, glycolaldehyde, and acetic acid; the C_3H_6O isomers included acetone, propanal, and propylene oxide. Comet 67P/CG showed similar relative abundance ratios for the C_2H_4O and the C_2H_6O isomers as well as for the C_2H_4O and C_2H_6O isomers, which was also the case in this study. Secondly, the abundance ratios of the larger $C_2H_4O_2$ and C_3H_6O isomers were similar in Comet 67P/CG as well as in this study.

These two comets span a range of cometary organics with 67P/CG having more processed ices, while Lovejoy is a new dynamic Oort cloud comet with few perihelion passages. The more processed object, 67P/CG, appears to reflect abundances comparable to older interstellar objects such as Sagittarius B2(N), while Lovejoy is more comparable to the low-mass object IRAS 16293-2422(B). Both objects are in fairly good agreement within the experimental findings. This may be representative of the pristine nature of cometary volatiles being derived from simple ices recondensed in the protosolar disk, or perhaps preserved from the protosolar nebula. While these results are speculative, it suggests additional experimental studies with variation of radiation and ice composition are needed as well as more observational studies of Jupiter Family Comets (JFCs) and Oort Cloud comets.

Of all of the trends observed here, the most striking is the over-production of glycolaldehyde as compared to the observational studies of older star-forming regions. Astrochemical models similarly over-produce glycolaldehyde in these regions (see Garrod et al. (2008) for a detailed discussion). It is the low-mass hot core, IRAS 16298-2422(B), that most closely matches the laboratory results for all molecules, and in the case of glycolaldehyde the similarity as compared to older star-forming regions is evident. This offers intriguing insight into the possible chemical implications for these findings. As mentioned above, perhaps the laboratory study presented here better simulates the low-mass hot core scenario, which has shorter timescales for ice irradiation, warm-up, and subsequent gas-phase processing. This indicates that in high-mass hot cores there is an additional gas-phase destruction mechanism for glycolaldehyde that is not currently included in the models, nor simulated in these experiments. Again, additional experiments that explore UV fluence and warm-up timescales are warranted. Likewise, studies into potential gas-phase

destruction pathways for glycolaldehyde are necessary.

4.5 Conclusions

Methanol ice is a potential source for complex organic molecules in interstellar clouds and possibly in comets. Here we present the UV photolysis and subsequent warm-up of a methanol ice with analysis via FTIR spectroscopy, mass spectrometry, and submillimeter/far-IR rotational spectroscopy. Nine products, all organic molecules containing more than one carbon atom, were detected in this work. In order of decreasing abundance, those photoproducts included dimethyl ether, acetaldehyde, ethanol, acetone, methyl formate, glycolaldehyde, ethylene oxide, vinyl alcohol, and ketene. The relative abundances provide evidence that the H + CH_3O photodissociation pathway is favored over the H + CH_2OH pathway under these experimental conditions. A technique for determining gas densities and rotational temperatures of each photoproduct was presented via a rotation diagram analysis procedure adapted for the laboratory spectroscopic technique of using lock-in detection with millimeter/submillimeter/far-IR spectroscopy. This technique provides an in-depth analysis of species that desorb from laboratory ices which allows for the determination of the rotational temperature and relative gas densities. Future studies may lead to a connection between temperature and the formation mechanisms of complex organics. Lastly, the results of this laboratory work were compared to the abundance ratios of several complex organics detected in high-mass protostar Orion-KL, low-mass protostar IRAS 16293-2422(B), protocluster Sagittarius B2(N), and in comets Lovejoy and 67P/CG. Similar abundance ratios with respect to methanol were detected for many of the organics of the hot cores (specifically ethylene oxide, ethanol, methyl formate, and dimethyl ether) while the abundance ratios best matched with the low-mass protostar observations of IRAS 16293-2422(B) and comet Lovejoy.

Chapter 5

UV Photodesorption Studies of Water, Methanol, and Carbon Monoxide Ices

5.1 Introduction

The gas-grain connection in the interstellar medium (ISM) is far from simple. Molecules that form on the surface of low temperature icy grains can sublimate to the gas phase via several processes which can be thermal or nonthermal in nature. Thermal desorption occurs when the temperature of the surrounding environment warms; for example, when a young star forms inside of a molecular interstellar cloud. Examples of nonthermal desorption processes include UV photodesorption, cosmic-ray sputtering, and chemical desorption. The list continues to grow as we gain a deeper understanding of the physical and chemical mechanisms at play in these environments. Nonthermal desorption mechanisms are required to explain the chemical abundances in cold dense cores where the temperature is $\sim$ 10 K, but yet the gas-phase composition is complex despite the temperature being significantly lower than the deposition temperatures of the detected gas-phase molecules. Among these nonthermal processes, UV photodesorption is the most studied to date, and more recently cosmic-ray sputtering has gained a lot of attention. These nonthermal desorption processes remain a mystery, although some studies are finally beginning to reveal key information about their efficiencies. Until recently, the most efficient nonthermal desorption process was thought to be UV photodesorption. However, as

computational models improve there is a growing amount of evidence that cosmic-ray sputtering may be the most efficient nonthermal desorption mechanism in cold dense cores (Wakelam et al., 2021) when compared with the efficiencies of photodesorption and chemical desorption. Nonetheless, UV photodesorption is still a nonthermal desorption mechanism at play in cold environments. In the ISM, UV photodesorption prevents the formation of icy grains in diffuse molecular clouds (Price et al., 2003) and is a nonthermal desorption mechanism in cold dense cores where the UV field is induced from cosmic ray collisions with H_2 molecules (Gredel et al., 1989; Prasad et al., 1983). In comets, the photodesorption of OH radicals by the solar UV field can affect the ice and gas-phase chemistry during their formation in a protoplanetary disk (Chaparro Molano, G. et al., 2012). Thus it is important to characterize the UV photodesorption behavior of important molecules (e.g., H_2O, CH_3OH, and CO) under various conditions relevant for star and planet formation.

Water is the most abundant molecule detected in interstellar ices and comets (Boogert et al., 2015; Gibb et al., 2004; Lecacheux et al., 2003; Öberg et al., 2011) and has proven to be an important molecule for the formation of planets due to its high sticking coefficient during collisions (Blum et al., 2008). Water also plays an important role in astrochemistry because it is a source of highly reactive OH radicals which affect the formation and destruction of many COMs in star-forming regions (Ishibashi et al., 2021) and planetary systems (Davila et al., 2008). As such, it is crucial to understand the life cycle of water in various environments of space. The UV photodesorption of water ice is an important nonthermal desorption mechanism that affects the ice-to-gas abundance ratios in cold cores (Fillion et al., 2021) and the location of the water snowline of protoplanetary disks (Oka et al., 2011; Terada et al., 2017). As such, the photodesorption yield of water is an important parameter to characterize and to include in astrochemical models of star and planet formation.

The UV photodesorption of H_2O has been studied through computational simulations (Andersson, S. et al., 2008; Arasa et al., 2010; Arasa et al., 2015) and laboratory experiments (Cruz-Diaz et al., 2017; Fillion et al., 2021; Mitchell et al., 2013; Öberg et al., 2009b; Westley et al., 1995a; Westley et al., 1995b). Among these studies, the reported photodesorption yields vary. This variation is likely a result of slight

variation in the physical conditions and analytical techniques. The H_2O photodesorption yield is difficult to quantify in laboratory experiments because the measurement is dependent on a long list of experimental considerations. When these experiments are performed the photodesorption yield is affected by (1) the analytical technique, (2) the background pressure of the chamber, (3) sample temperature, (5) sample structure, and (4) the UV light source. A highly sensitive analytical technique is required to detect photodesorbed products; therefore, mass spectrometry is typically used. When utilizing mass spectrometry to quantify photodesorbed products one must account for several factors including the mass sensitivity of analyte fragments, ionization cross section, incident electron energy, the fraction of ionized molecules, and mass overlaps. If these parameters are not well characterized and calibrated, then the measured photodesorption yields will be skewed. Mass overlaps are very difficult to account for in these experiments. For example, H_2O cannot be distinguished from OD because both have a $m/z = 18$. Furthermore, the photodesorption yield of OH measured at $m/z = 17$ also has small contributions from OH fragments of H_2O created in the mass spectrometer. The use of mm/submm spectroscopy can address these analytical challenges by detecting unique rotational transitions of photodesorbed H_2O, its photofragment OH, and isotopologues D_2O, OD, and HDO without ambiguity. This provides good reason to explore the feasibility of the mm/submm spectroscopic detection of UV-photodesorbed products of laboratory ices.

The implementation of mm/submm spectroscopy to quantify photodesorption yield still does not address the hardship of background water contamination. Photodesorption experiments require a very clean vacuum chamber because photodesorption of water absorbed on the walls and other surfaces of the vacuum chamber affect the H_2O signal. Therefore, it is very important to collect control measurements to quantify the background water. However, this is difficult because even very small deviations from day to day will affect the water signal. For example, to form an ice sample, water vapor is purposefully flowed through the chamber and deposited on a cold substrate, but at the same time the vacuum chamber walls and components are coated with a fresh layer of H_2O molecules. Most previous laboratory studies of photodesorption quantify the background contamination before the ice sample is

formed and do not account for the contamination provided during sample formation. This problem has been explored in the studies presented in this chapter and is discussed further in Section 5.3.3. To alleviate the challenges of quantifying the varying background H_2O contamination, UV photodesorption studies were performed herein for methanol (CH_3OH) ice to establish important control procedures to assess background contamination after ice sample formation.

The photodeosprtion of methanol ice has been previously studied in the laboratory (Bertin et al., 2016; Cruz-Diaz et al., 2016; Martín-Doménech et al., 2016; Öberg et al., 2009a) although the physical conditions vary. Öberg et al. (2009a) was the first to report a methanol UV photodesorption yield of $\sim 10^{-3}$ molecules photon^{-1} measured indirectly through IR spectroscopy of the ice sample. The studies by Bertin et al. (2016) directly measured the UV photodesorption yield of CH_3OH from a methanol ice sample with mass spectrometry and found a significantly lower yield of $\sim 10^{-5}$ molecules photon^{-1}; here the light source was different from the studies by Öberg et al. (2009a). Cruz-Diaz et al. (2016) reported no detection of photodesorbed CH_3OH, but derived an upper-limit of 3×10^{-5} molecules photon^{-1}, using a similar light source as Öberg et al. (2009a). Both Bertin et al. (2016) and Cruz-Diaz et al. (2016) attribute the low yield and non-detection of photodesorbed CH_3OH to the efficient photodissociation and report detections of photofragments. Bertin et al. (2016) detected photodesorbed CO, H_2CO, CH_3, and OH while Cruz-Diaz et al. (2016) detected photodesorbed H_2, CO, and CH_4. Martín-Doménech et al. (2016) measured the photodesorption of CH_3OH after its formation in a H_2O + CH_4 ice sample and reported that no photodesorbed methanol was detected. The methanol photodesorption studies presented in the current work focused on measuring an increase in mass signals of photofragments H_2, CH_3, CH_4, CO, CH_2OH and CH_3O, and CO_2 upon UV-irradiation of a methanol ice sample at low temperature (12 K) to develop an appropriate procedure for quantifying background contamination present after ice sample formation. The results of these experiments are presented in Section 5.3.3.

The background procedures that were established for methanol photodesorption experiments were then applied to another chemical system to measure the photodesorption of carbon monoxide (CO) ice and to provide a proof-of-concept for detecting

photodesorbed products with mm/submm spectroscopy. Carbon monoxide was chosen because it has been thouroughly studied through laboratory experiments (Bertin et al., 2012; Bertin et al., 2013; Carrascosa et al., 2021a; Chen et al., 2014; Fayolle et al., 2011; González Díaz et al., 2019; Muñoz Caro et al., 2016; Muñoz Caro et al., 2010; Öberg et al., 2009c; Öberg, K. I. et al., 2007; Paardekooper et al., 2016c) and the photodesorption yield is higher than its photodissociation. These studies have discovered various physical factors that affect the photodesorption yield of CO such as UV wavelength dependence (Fayolle et al., 2011), ice formation temperature (Muñoz Caro et al., 2016; Muñoz Caro et al., 2010; Öberg et al., 2009c), photon penetration depth (Chen et al., 2014; Fayolle et al., 2011; Muñoz Caro et al., 2010), and ice composition (Bertin et al., 2012; Bertin et al., 2013). A variety of photodesorption yields have been reported due to slight variations in experimental conditions (Paardekooper et al., 2016b), but overall these studies have provided a sufficient amount of information to improve computational models. Since CO photodesorption has been widely studied it served as a good candidate to assess the possibility of using mm/submm spectroscopy to detect photodesorbed products of laboratory ice samples and the results are presented in Section 5.3.4.

5.2 Experimental Methods

The photodesorption products of water, methanol, and carbon monoxide ice were measured by mass spectrometry at low temperature (∼10-12 K) to assess the feasibility of using mm/submm spectroscopy to detect photodesorbed products of laboratory ice samples. The water and methanol experiments were conducted in experimental setup 2 described in Chapter 2 Section 2.1.2 and the carbon monoxide experiments took place in experimental setup 3 described in Chapter 2 Section 2.1.3. UV photodesorption measurements are very sensitive to background contamination of the vacuum chamber and a procedure was developed to quantify background contributions after the vapor/gas deposition of an ice sample. This procedure is referred to as "no ice background" tests henceforth. The no ice background tests involve replication of the ice deposition while the sample substrate was held at high temperature to ensure no ice sample was deposited. The UV lamp was then turned

on and mass spectra were collected when no ice sample was present to quantify the photodesorption of contaminants from the chamber walls and other components inside the vacuum chamber. The experimental details for the water, methanol, and carbon monoxide experiments are presented in the following sections.

5.2.1 Water

The water photodesorption experiments were performed in the experimental setup 2 described in Chapter 2 Section 2.1.2. First, the cryostat was cooled to the base temperature of 12 K and the base pressure of the chamber was 2.2 $\times$ 10^{-9} Torr. The sample substrate was then heated to 160 K and the ice formation process was replicated by flowing 5.0 $\times$ 10^{-7} Torr of water vapor in the chamber for 25 minutes. The sample substrate was then heated to 200 K to ensure any condensed molecules were fully sublimated. The substrate was then cooled to 12 K and the gate valve was closed to isolate the chamber from the pumps. Mass spectra were collected with the lamp off and when the lamp was turned on every 5 minutes for 20 minutes. The chamber pressure increased from 2.8 $\times$ 10^{-9} to 1.2 $\times$ 10^{-8} Torr when the UV lamp was turned on. Next, a $\sim$1.5 μm water ice sample was formed at 12 K by leaking 5.0 $\times$ 10^{-7} Torr of water vapor in the chamber for 25 minutes from a liquid Milli-Q water sample that was freeze-pump-thawed three times to remove dissolved gases. After the ice sample was formed the chamber was pumped back to 2.2 $\times$ 10^{-9} Torr. Then the gate valve was closed and mass spectra were collected with the UV lamp off and on in 5 minute intervals for 25 minutes. The results are presented in Section 5.3.2.

5.2.2 Methanol

The methanol photodesorption experiments were performed in experimental setup 2 described in Chapter 2 Section 2.1.3 and followed similar procedures as described in Section 5.2.1 for water photodesorption with some minor differences. First, the cryostat was cooled to 12 K and the base pressure of the chamber was 2.4 $\times$ 10^{-9} Torr. The sample substrate was then heated to 150 K and the ice formation process was replicated. Two sample thicknesses were assessed, referred to herein as "thin"

and "thick". The thin ice sample was ∼0.5 μm and the thick sample was ∼1 μm. The ice samples were formed by vapor deposition from 99.9% HPLC grade liquid methanol (Fisher Scientific, A452-4) that was degassed by three freeze-pump-thaw cycles. After the ice formation was replicated the sample substrate was heated to 200 K to rapidly sublimate any condensed contaminants. The substrate was then cooled to 12 K and mass spectra were collected with the UV lamp off and on in 5 minute intervals for 25 minutes (no ice background) and 45 minutes (ice sample). When the UV lamp was turned on during the thin ice experiment, the chamber pressure increased to 2.5 $\times$ 10^{-8} Torr during the no ice background tests and 2.2 $\times$ 10^{-8} Torr when the ice sample was present. When the UV lamp was turned on during the thick ice experiment, the chamber pressure increased to 1.9 $\times$ 10^{-8} Torr during the no ice background tests and 2.7 $\times$ 10^{-8} Torr when the ice sample was present.

5.2.3 Carbon Monoxide

The carbon monoxide photodesorption experiments took place in experimental setup 3 described in Chapter 2 Section 2.1.3 and followed similar procedures as those described for water and methanol photodesorption experiments. There are three experimental differences from the water and methanol photodesorption experiments due to changes to the UV light source: (1) the lamp is positioned perpendicular to the ice sample, (2) a McCarrol microwave cavity was used to excite the H_2 gas, and (3) a UV waveguide was placed between the light source and the ice sample to prevent photodesorption from the chamber walls and components. The rest of the experimental details are as follows. First, the cryostat was cooled to 10 K and the base pressure of the chamber was 3.0 $\times$ 10^{-9} Torr. The substrate was then heated to 150 K and the ice sample deposition was replicated by leaking 5.0 $\times$ 10^{-7} Torr of CO gas in the chamber for 10 minutes. The substrate was then heated to 200 K to remove any condensed contaminants. Next, the substrate was cooled to 10 K and mass spectra were collected with the UV lamp off and then on in 5 minute intervals for 30 minutes. The chamber pressure increased to 3.3 $\times$ 10^{-9} Torr when the UV lamp was turned on. Next, two CO ice samples were formed at 10 K by leaking CO gas in the chamber at 5.0 $\times$ 10^{-7} Torr for 10 minutes. A "thick" CO ice sample formed on the top side of the substrate and a "thin" ice sample was formed on the reverse

side of the substrate. The exact thickness of the samples were not directly measured. The photodesorption signal of CO and CO_2 was measured for the thin ice sample by rotating the cryostat 180°. Mass spectra were collected with the UV lamp off and then on in 5 minute intervals for 30 minutes. The chamber pressure increased to 3.3 $\times$ 10^{-9} Torr when the UV lamp was turned on. The cryostat was then rotated 180° to measure the photodesorption signals of the thick ice sample. The same procedure was followed as performed for the no ice background test and the thin ice sample. The chamber pressure increased to 3.4 $\times$ 10^{-9} Torr while the UV lamp was on. The results are shown in Figure 5.8 for the no ice background tests (orange), the thin ice sample (green), and the thick ice sample (blue). IR spectra were collected at the same time as the mass spectra, every 5 minutes for 30 minutes, and are shown in Figure 5.7.

5.3 Results and Discussion

The results from three photodesorption studies are presented in this section for water, methanol, and carbon monoxide ice samples at low temperature (10-12 K). The aim of these experiments were to assess the feasibility of using mm/submm spectroscopy to detect photodesorbed species that cannot be distinguished with mass spectrometry. The photodesorption signals were measured for H_2O, CH_3OH, and CO along with several photofragments and photoproducts.

5.3.1 Preliminary Tests

A preliminary gas-phase photolysis test was performed before the ice photodesorption experiments took place. The UV photolysis of water vapor was measured to confirm UV photons were entering the vacuum chamber. The absorption signal of H_2O was measured at the $1_{1,0} \leftarrow 1_{0,1}$ rotational transition at ~556936 MHz when the UV lamp was off and after it was turned on. The "lamp on" measurement showed a depletion in the absorption signal confirming some of the water vapor was photolyzed to H and OH. These submm spectra are shown in Figure 5.1.

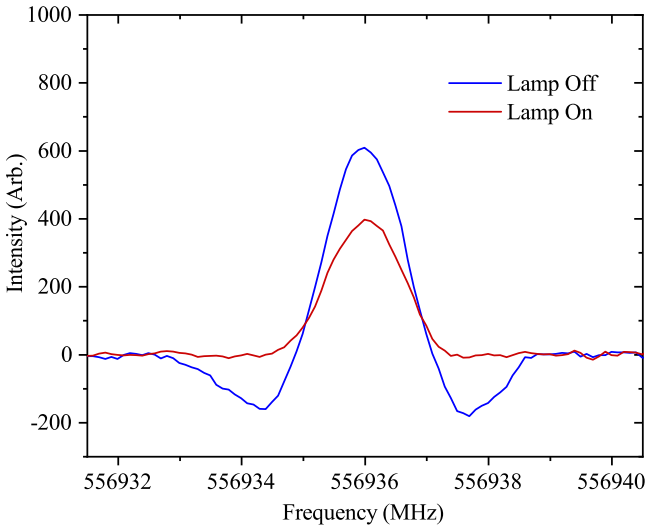

FIGURE 5.1: Depletion of water vapor signal when the UV lamp was turned on (red) vs. off (blue).

5.3.2 Water Photodesorption

The photodesorption signals of H_2O and OH are shown in Figure 5.2 from a 12 K H_2O ice in blue and the no ice background test in orange. The data were background subtracted by the partial pressures measured with the lamp off, and the lamp off measurement is plotted at 0 minutes. The partial pressure of H_2O and OH were

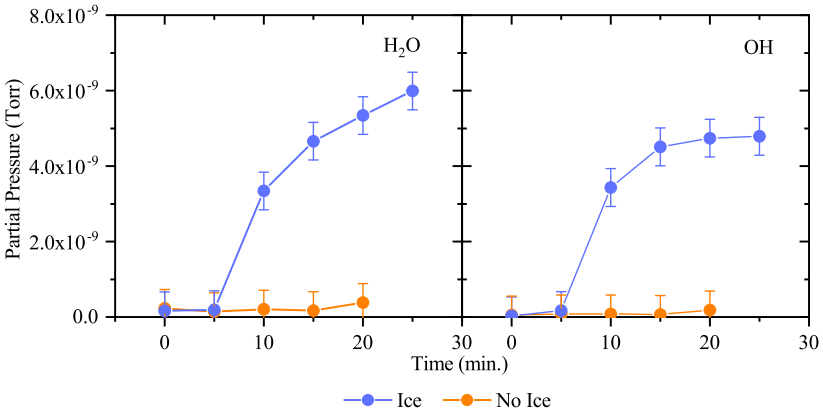

FIGURE 5.2: Photodesorption measurements of water (m/z = 18) and OH (m/z = 17) when no ice sample was present (orange) and when a water ice sample was present (blue). The partial pressure of H_2O and OH increased when the UV lamp was turned on. The y-axis error bars were calculated from the noise standard deviation of the mass spectrometer signal.

measured with the mass spectrometer at m/z = 18 and 17, respectively. The partial pressure of H_2O noticeably increased after 5 minutes of UV-exposure. The gas density of photodesorbed H_2O was $\sim 10^8$ molecules cm^{-3}. This gas density is an order of magnitude below the detection limit of the current mm/submm spectrometer which is 1.1×10^9 molecules cm^{-3}. Therefore, the current mm/submm spectroscopic technique is not sensitive enough to detect photodesorbed H_2O molecules from a water ice sample and experimental adaptations such as increasing the spectral path length would need to be implemented to detect photodesorbed H_2O.

5.3.3 Methanol Photodesorption

The photodesorption signals of intact methanol and the photofragments and photoproducts of methanol were measured for a thin and thick methanol ice sample. These measurements are presented in Figure 5.3 and 5.4. The data were background subtracted by the partial pressures measured with the lamp off, and the lamp off measurement is plotted at 0 minutes.

Photodesorption signals were measured for CH_3 at m/z = 15, CH_4 at m/z = 16, OH at m/z = 17, CO at m/z = 28, CH_2OH and CH_3O at m/z = 31, and CO_2 at m/z = 44 when a methanol ice was present (blue) and when no methanol ice was present (orange). The photodesorption signal was also measured for H_2 at m/z = 2 for both the thin and thick methanol ice samples and the results are shown in Figure 5.5. A large increase at m/z = 2 was detected when the UV lamp was turned on and H_2 had the highest partial pressure increase in these experiments. This was also observed in the studies by Cruz-Diaz et al. (2016). The thin ice sample showed similar H_2 partial pressures to the no ice background tests, but the thick ice sample showed a larger H_2 partial pressure increase than the no ice background test as seen in the right panel of Figure 5.5. All other measurements presented in Figures 5.3 and 5.4 showed the same partial pressures as the no ice background tests. Therefore, there is no evidence that these molecules were photodesorbed from the ice sample and were likely photodesorbed from other surfaces in the vacuum, with the two largest surfaces being the chamber walls and the cold arm of the cryostat. The second largest partial pressure increase was measured for CH_3 and CH_4 for both the thin and thick ice samples, followed by CO_2 and CO. The photodesorption signal was

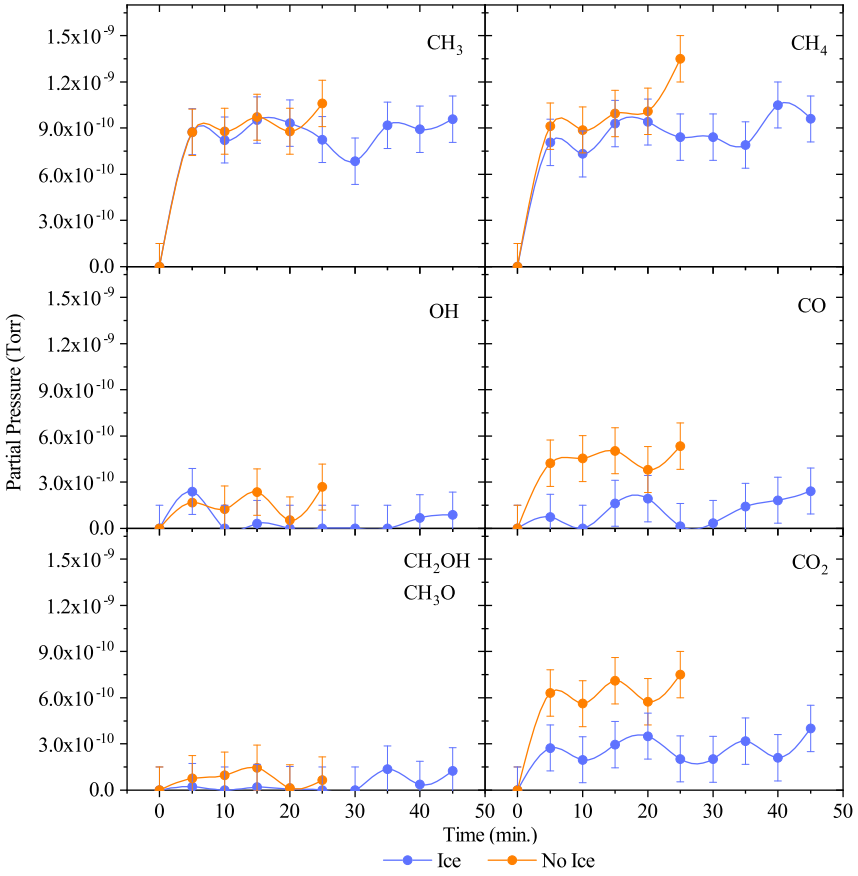

FIGURE 5.3: Photodesorption measurements of CH_3 (m/z = 15), CH_4 (m/z = 16), OH (m/z = 17), CO (m/z = 28), CH_2OH + CH_3O (m/z = 31), and CO_2 (m/z = 44) from a $\sim$ 0.5 μm methanol ice sample (blue) and no ice sample (orange) background tests. The y-axis error bars were calculated from the noise standard deviation of the mass spectrometer signal.

also measured for intact CH_3OH at m/z = 32, but no increase was measured when the UV lamp was turned on. Bertin et al. (2016) and Cruz-Diaz et al. (2016) measured little or no signal for photodesorbed CH_3OH and the most abundant photoproduct (excluding H_2) was CO in both studies. The similar signals between the ice and no ice measurements demonstrate how important it is to conduct these experiments in ultrahigh vacuum conditions and to use a UV waveguide to prevent UV photons from colliding with the surfaces inside of the vacuum chamber other than the ice sample.

The addition of mm/submm spectroscopy to a methanol photodesorption experiment would allow for the determination of the abundance ratio between CH_3O

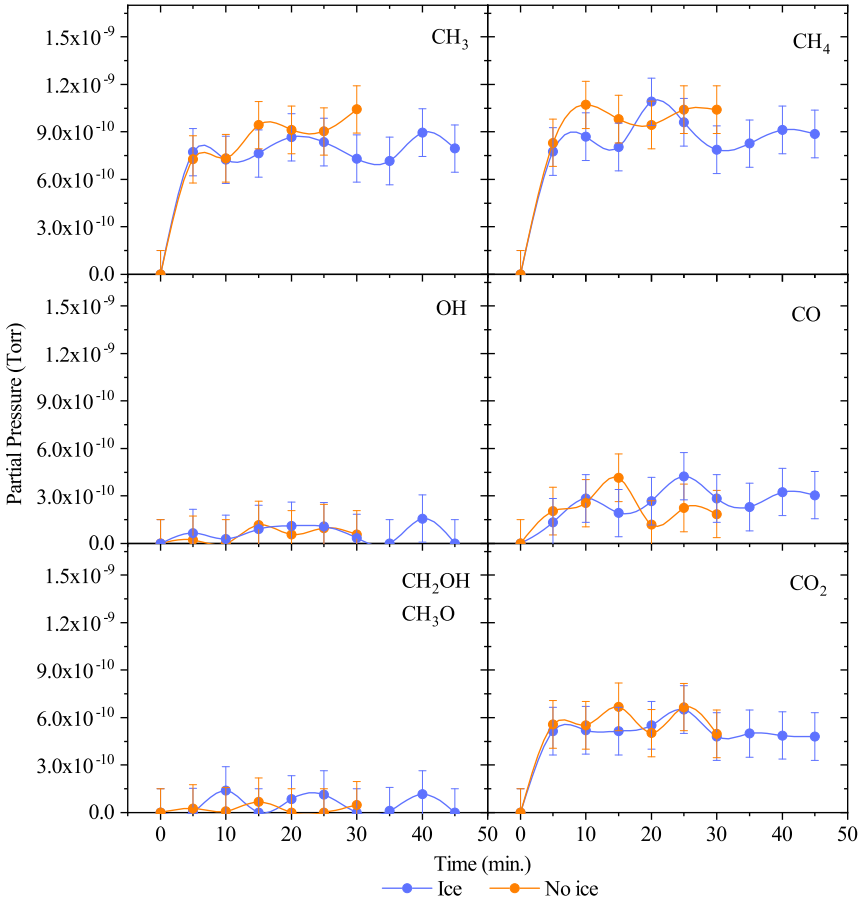

FIGURE 5.4: Photodesorption measurements of CH_3 (m/z = 15), CH_4 (m/z = 16), OH (m/z = 17), CO (m/z = 28), CH_2OH + CH_3O (m/z = 31), and CO_2 (m/z = 44) from a $\sim$ 1 μm methanol ice sample (blue) and no ice sample (orange) background tests. The y-axis error bars were calculated from the noise standard deviation of the mass spectrometer signal.

and CH_2OH radicals which cannot be distinguished via mass spectrometry, but previous studies have shown that the photodesorption of these radicals is negligible. Therefore, mm/submm spectroscopy would not provide anymore information to methanol photodesorption studies.

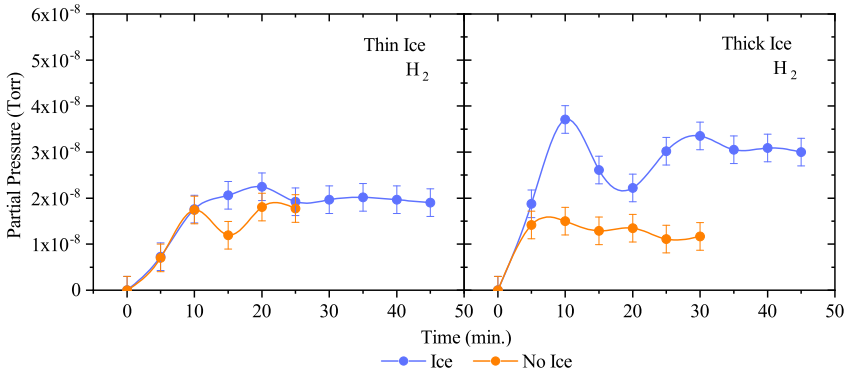

FIGURE 5.5: Photodesorption measurements of H_2 (m/z = 2) from a $\sim$ 1μm methanol ice sample (right) and a $\sim$ 0.5μm methanol ice sample (left) are shown in blue and the no ice sample background scans are shown in orange. The y-axis error bars are calculated from the noise standard deviation of the mass spectrometer signal.

5.3.4 Carbon Monoxide Photodesorption

The photodesorption of CO was measured for a thin and thick CO ice sample to assess the feasibility of using mm/submm spectroscopy to detect photodesorbed products of laboratory ice samples. Figure 5.6 shows the C≡O stretch of the thin ice sample in red and the thick ice sample in blue to compare the relative ice thicknesses.

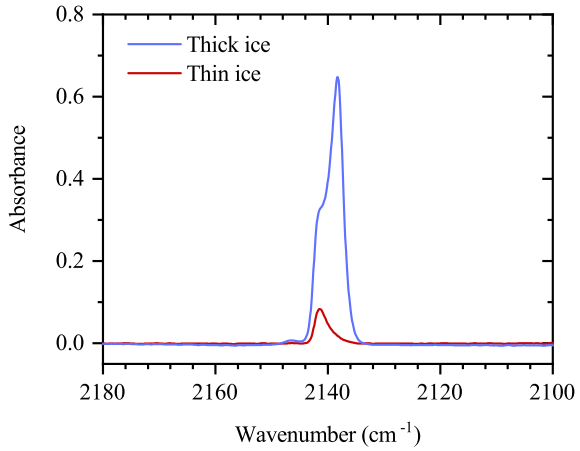

FIGURE 5.6: IR spectra of the thin (red) and thick (blue) CO ice samples to compare relative sample thickness.

Both ice samples were exposed to the UV lamp for 30 min. IR spectra were collected of the thick ice sample during the 30 minute exposure and are shown in Figure 5.7. The peak located at $\sim$2138 cm^{-1} is the C≡O stretch of carbon monoxide and the

peak area decreased over the 30 minute UV exposure due to photolysis. This is confirmed by the appearance of a new IR peak at ~2345 cm^{-1} assigned to the C=O stretch of carbon dioxide (CO_2).

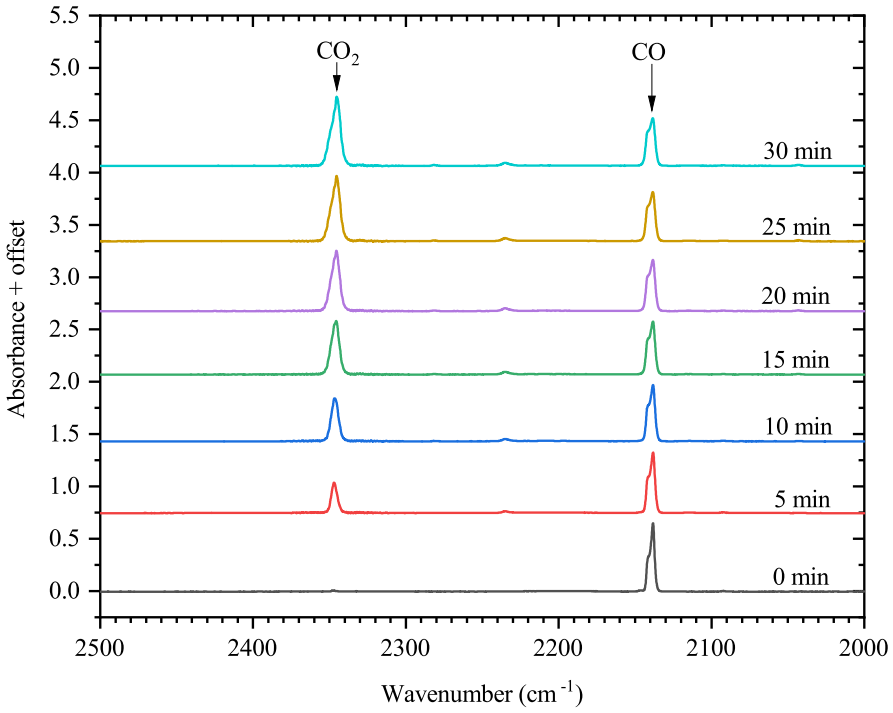

FIGURE 5.7: IR spectra of the thick CO ice exposed to UV photons for 30 minutes at 10 K. The peak area of the CO peak decreases and the CO_2 peak area increases with increased UV exposure. The spectra are offset for clarity.

The photodesorption signals of CO and CO_2 were measured for the thick and thin ice samples by collecting mass spectra during the 30 minute UV exposure in 5 minute intervals. The mass signals of CO at m/z = 28 and CO_2 at m/z = 44 are shown in Figure 5.8 for the thick ice in blue, the thin ice in green, and the no ice background measurements in orange. The data in Figure 5.8 were background subtracted by the partial pressures measured with the lamp off, and the lamp off measurement is plotted at 0 minutes. The next data point shows the partial pressure measured after the sample was exposed to the UV lamp for 5 minutes. A small increase in CO partial pressure was measured for the thick, thin, and no ice background tests with the largest increase detected for the thick CO ice sample. The y-axis error bars show

the noise standard deviation of the mass spectrometer. The CO_2 signal did not increase when the lamp was turned on and Figure 5.8 shows that all three tests showed the sample partial pressures within experimental error, therefore no photodesorbed CO_2 was detected. The photodesorption signal of CO could likely be increased by improving the vacuum level of the chamber to less than 10^{-10} Torr since the current turbo pump does not achieve this. In any case, these upper limit measurements have demonstrated that the current mm/submm spectroscopic technique is not sensitive enough to detect photodesorbed CO.

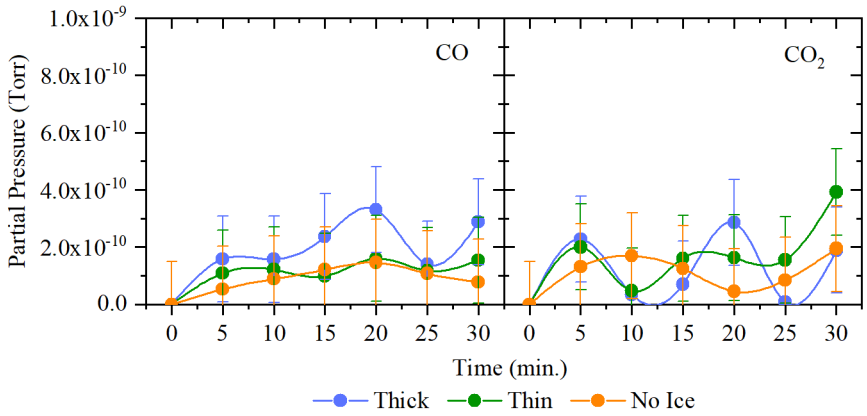

FIGURE 5.8: Photodesorption measurements of CO (m/z = 28, left) and CO_2 (m/z = 44, right) from a thick CO ice sample (blue), a thin CO ice sample (green), and the no ice sample background measurement (orange). The y-axis error bars are calculated from the noise standard deviation of the mass spectrometer signal.

5.3.5 Limitations of SubLIME for Photodesorption Experiments

Photodesorption experiments are very challenging and require an extremely sensitive analytical technique and an extremely clean vacuum chamber. The small amount of desorbed molecules can also quickly redeposit on the cold arm of the cryostat which can reach temperatures as low as ∼15 K. The cold arm is also covered by a stainless steel radiation shield which reaches temperatures as low as ∼25 K. Therefore, when molecules desorb from the ice sample, many of them quickly redeposit on the cold arm and radiation shield. This process has proven to be very challenging and frustrating for these experiments. Deposition onto the cold arm and radiation shield also occurs when an ice sample is formed which contributes to the no ice background measurements. When an ice sample is formed, the majority of

the molecules are deposited onto the substrate from a capillary tube positioned with the opening towards the substrate, but a large amount of molecules also deposit onto the cold arm of the cryostat. Implementation of a new experimental design that separates the sample from the cold arm of the cryostat would be very beneficial. However, this approach would be difficult to implement because it would require isolation of the cold arm without adding an extra thermal load. Lastly, the current detection limits of the mm/submm spectrometer will not allow for the detection of photodesorbed species. A few adaptations could be implemented to address this limitation. First, the pathlength of the gas cell could be increased by incorporating a multipass or cavity-enhanced technique. A multipass system could have been applied to experimental setup 2, but was never pursued because the available optics were too large to fit inside of the vacuum chamber. An external multipass setup could be designed for experimental setup 3 because the spectral power of the light source is very high as compared to the one used in experimental setup 2. However, considering the very low gas density produced during a photodesorption experiment, cavity enhancement is the better option. Second, the gas density of photodesorbed products could be increased by designing a larger surface area of the ice sample. This would require a larger substrate and more UV light sources to cover the entire sample, but these changes are likely less costly than a new spectrometer.

5.4 Conclusions

The studies presented in this chapter explored the feasibility of using mm/submm spectroscopy to detect photodesorbed products of laboratory ice samples in interstellar conditions. The water ice photodesorption experiments measured a higher partial pressure of H_2O and OH when a water ice was present versus those pressures measured during the no ice background measurements, showing that molecules were photodesorbed from the ice sample and not just from the walls of the chamber. Unfortunately, the density of photodesorbed water was less than 1.9×10^8 molecules cm^{-3} which is an order of magnitude below the detection limit of the mm/submm spectrometer, 1.1×10^9 molecules cm^{-3}. Therefore, to detect photodesorbed water with mm/submm spectroscopy, the sensitivity needs to be improved and/or

experimental changes need to be implemented to increase the gas density of photodesorbed water. For the methanol photodesorption experiments, the amount of background contamination from the ice sample formation process (i.e., vapor/gas deposition) was assessed by performing no ice background tests. The same partial pressures were measured during the no ice background tests and when the methanol ice was present, except for photodesorbed H_2 from the thick ice sample. This means that all the detected molecules photodesorbed from other surfaces in the chamber such as the stainless steel walls and the cold arm of the cryostat. This provided sufficient evidence that several precautions need to be considered for these experiments including the tedious quantification of background contamination after ice deposition (not just before) and the use of an UV waveguide to direct the photons to the ice sample and to prevent photons from hitting other surfaces of the chamber. An UV waveguide was implemented for the carbon monoxide photodesorption experiments and the partial pressures detected upon UV exposure decreased significantly as compared to the methanol photodesorption experiments. This provided evidence that the signal arising from molecules photodesorbed from the walls and other chamber components was greatly minimized by the UV waveguide. A very small increase in the partial pressure of CO was measured by mass spectrometry and was within the experimental error of the partial pressure measured during the no ice background tests. Therefore, the vacuum level of the chamber needs to be improved to detect a reliable signal of photodesorbed CO. Nonetheless, these measurements provide an upper limit which is still significantly below the detection limit of the current mm/submm spectrometer.

In conclusion, the current mm/submm spectroscopic technique is not sensitive enough to detect UV-photodesorbed products. The detection limits are orders of magnitude above the density of photodesorbed products. For example, less than 10^7 molecules cm^{-3} of CO photodesorbed from the CO ice sample while the mm/submm detection limit is on the order of 10^{11} molecules cm^{-3}. In order to detect UV-photodesorbed products with mm/submm spectroscopy a cavity-enhanced spectroscopic technique is required. The photodesorption signal would likely also need to be enhanced by designing a substrate capable of increasing the surface area of the ice sample. The traditional experimental approach of ice photodesorption experiments (e.g., Bertin

et al. (2016) and Cruz-Diaz et al. (2017)) is not suitable for detection by mm/submm spectroscopy. Future studies should consider the yield of molecules desorbed as a result of cosmic-ray impact by protons and electrons since computational results provide motivation for the experimental characterization of this nonthermal process. SubLIME could contribute to this effort by identifying the abundance ratios of molecules and radicals that cannot be distinguished with mass spectrometry including H_2O and OD and CH_2OH and CH_3O from water-rich methanol ice samples. The results of computational studies also provide evidence that cosmic-ray sputtering increases the gas-phase abundances of large molecules such as methyl formate ($HCOOCH_3$) (Shingledecker et al., 2018b) and SubLIME could be used to fully quantify the abundance ratios of desorbed structural isomers methyl formate ($HCOOCH_3$) and glycolaldehyde ($HOCH_2CHO$) which cannot be distinguished by electron ionization mass spectrometry (EI-MS).

Chapter 6

Conclusions and Future Directions

6.1 Conclusions

The focus of this dissertation involved the development of a new technique for laboratory astrochemistry studies of cosmic ice chemistry. The Sublimation of Laboratory Ices Millimeter/submillimeter Experiment (SubLIME) combines the traditional analytical approaches of cosmic ice experiments (FTIR spectroscopy and mass spectrometry) with the structure-specificity of rotational spectroscopy to unambiguously identify products of energetically processed ice samples and to provide high-resolution spectra that can be directly compared to telescope data of interstellar clouds and comets. Procedures were developed for determining surface binding energy, sublimation enthalpy, rotational temperature, and gas density for their use in astrochemical computational models.

Chapter 1 introduced the astrochemistry background and motivation for this work. Chapter 2 described the experimental design of SubLIME, the millimeter and submillimeter spectroscopic detection limits, and the experimental procedures for energetic processing of ice sample with heat and UV photons. Chapter 3 presented proof-of-concept results for detecting sublimated ice samples of water (H_2O and D_2O) and methanol (CH_3OH) with millimeter and submillimeter spectroscopy, and techniques for using rotational spectroscopy to determine surface binding energy and sublimation enthalpy. Chapter 4 presented results of the first study to use rotational spectroscopy to identify and quantify complex organic products of a UV-photolyzed methanol ice sample. Eleven sublimed photoproducts were uniquely

identified: carbon monoxide (CO), formaldehyde (H_2CO), ketene (C_2H_2O), acetaldehyde (CH_3CHO), ethylene oxide (CH_2OCH_2), vinyl alcohol (CH_2CHOH), ethanol (CH_3CH_2OH), dimethyl ether (CH_3OCH_3), methyl formate ($HCOOCH_3$), glycolaldehyde ($HOCH_2CHO$), and acetone ($(CH_3)_2CO$). The rotational temperatures and gas densities were calculated for the organics containing two or more C-atoms via a rotational diagram analysis. The abundance ratios of the sublimated species (normalized to methanol) were compared to those observed in hot cores (Orion-KL, Sagittarius B2(N), and IRAS 16293-2422(B)) and in comets C/2014 Q2 (Lovejoy) and 67P/Chury-umov–Gerasimenko. Chapter 5 examined the feasibility of using direct-absorption millimeter and submillimeter spectroscopy to detect UV-photodesorbed products of laboratory ice samples of water (H_2O), methanol (CH_3OH), and carbon monoxide (CO). This work determined that the gas density of photodesorbed species is below the detection limit of the spectrometer and a cavity-enhanced spectroscopic technique is likely required along with a new sample design to increase the yield of photodesorbed products. The work presented herein was just an introduction to the capabilities of this new technique, and the list of future work continues to grow.

6.2 Future Directions of SubLIME

6.2.1 Spectroscopic Techniques

The work of this dissertation demonstrated the benefits of the current millimeter and submillimeter spectroscopic technique along with its limitations (see Chapter 4 Section 4.4 and Chapter 5 Section 5.3.5). The limitations can be summed up to the following: (1) gas-density limit of detection and (2) slow data acquisition speed. Thus, there are improvements that can be implemented. The first limitation can be addressed by increasing the path length of the gas cell and by increasing the number of spectral averages. To reach the detection limits required to detect UV-photodesorbed products would require both the pathlength and number of spectral averages to increase by several orders of magnitude, which can only be achieved by a cavity Fourier-Transform-millimeter (FT-mm) technique similar to the one published by Drouin et al. (2016). This technique uses a semi-confocal Fabry-Perot cavity

and has demonstrated a detection limit of 2.5 $\times$ 10^{12} molecules cm^{-3} for a nitrous oxide (N_2O) transitions at 100491 MHz measured in just 100 ms. Nitrous oxide has a very weak dipole moment (0.16 D) and the detection limits of other molecules with stronger dipoles will be lower. Despite the improved sensitivity, this technique does have some noteable limitations including low frequency spectral coverage (92-105 GHz), the narrow bandwidth of the cavity (20 MHz), and the difficulty of incorporating the spectrometer in the experimental setups described in Chapter 2. Unfortunately, the intensities of the rotational transitions in the 90-100 GHz region are orders of magnitude lower than those at higher frequencies ($\sim$300 GHz - 1 THz) because this is where the Boltzmann peak appears for most molecules of focus at 300 K. This is why the detection limits of the spectroscopic technique used for the studies presented in this dissertation (see Chapter 2 Table 2.1) are similar to that reported for the FT-mm technique by Drouin et al. (2016). For example, the detection limit of carbon monoxide at 691473.08 MHz (1.5 $\times$ 10^{11} molecules cm^{-3}) measured by direct-absorption phase-sensitive detection is lower than the detection limit of nitrous oxide at 100491 MHz (2.5 $\times$ 10^{12} molecules cm^{-3}) measured with FT-mm spectroscopy. If a FT-mm instrument was designed to cover higher frequencies it would surpass the detection limits of the current SubLIME spectroscopic technique, but this is limited by technology development and cost. Secondly, the frequency coverage does not compare to the broadband capabilities of the current technique (70 - 1100 GHz). Custom designed FT-mm instruments would need to be produced for detecting water and carbon monoxide because the rotational transitions of these molecules are so widely spread. This type of setup would rapidly become extremely costly.

A broadband heterodyne or chirped-pulse spectrometer would immensely increase the data aquisition speed and number of spectral averages and would provide similar detection limits as the current technique. Gerecht et al. (2011) report the detection limit of water (H_2O) is 2 $\times$ 10^{10} molecules cm^{-3} at 566.9 GHz with a chirped-pulse THz spectrometer (530-620 GHz). This water signal was measured in a 10 GHz bandwidth spectrum (along with several other molecules) consisting of 80,000 spectral averages in just 30 seconds. It would take the current SubLIME spectrometer 5 years to collect a spectrum of the same resolution and bandwidth. While

the detection limits are similar, those of the current technique are still slightly lower, but the data aquisition speed alone provides motivation to pursue a broadband heterodyne or chirped-pulse submillimeter technique.

6.2.2 Conformational and Structural Isomer Analysis of Important Prebiotic Molecules

The structure specificity of SubLIME allows for the unambiguous identification and quantification of isomers. This was demonstrated in the methanol photolysis studies presented in Chapter 4 where both structural (e.g., methyl formate and glycolaldehyde) and conformational (e.g., trans and gauche ethanol) isomers were detected by their individual pure rotational transitions, although the abundance ratios between conformational isomers were not explored. This begs the question: What are the abundance ratios of conformers that sublimate from icy grains? This question is particularly important for the interstellar detection of the prebiotic molecule glycine. The lowest energy conformers of glycine (I and II) have very different submillimeter signatures and thus astronomers need to know which conformer is predicted to be more abundant. Furthermore, the abundance ratios of $C_2H_5NO_2$ structural isomers, methylcarbamic acid ($CH_3NHCOOH$), methyl carbamate (NH_2COCH_3O), and glycolamide (NH_2COCH_2OH), also need to be quantified. Previous laboratory ice studies report the detection of glycine from the low temperature energetic processing of interstellar ice analogs, but these isomers could not be distinguished with electron-ionization mass spectrometry. As such, the reported glycine column densities may be overestimated. Future experiments could determine the abundance ratios of glycine conformers I/II and the $C_2H_5NO_2$ structural isomers to predict the feasibility of the interstellar detection of glycine.

Appendix A

Additional Details on Spectral Analysis

A.1 Submillimeter Spectral Assingment

The broadband submillimeter spectrum collected from 806500 to 812890 MHz was assigned for 5-σ peaks and can be found in the online data for 2021. An example table of the first five entries is shown in Table A.1. Table A.1 includes the center frequency, molecule, chemical formula, and rotational quantum numbers: *J'(Ka',Kc') - J(Ka,Kc)*. Peaks marked with '?' belong to unknown features. Peaks labeled 'U' refer to transitions that are unassigned in their respective spectral catalog, but were confirmed from spectra of chemical standards.

TABLE A.1: Submillimeter Spectral Assignment from 806500 to 812890 MHz

Peak #	Frequency (MHz)	Molecule	Formula	Transition
1	806651.41	Carbon monoxide	CO	7 - 6
2	806699.95	Ketene	C_2H_2O	40(2,39) - 39(2,38)
3	806735.82	Ketene	C_2H_2O	40(5,36) - 39(5,35); 40(5,35) - 39(5,34)
4	806877.12	Dimethyl ether	CH_3OCH_3	26(6,21) - 25(5,20) EE
4	806877.61	Dimethyl ether	CH_3OCH_3	26(6,21) - 25(5,20) AE
4	806878.01	Dimethyl ether	CH_3OCH_3	26(6,21) - 25(5,20) AA
5	806997.05	Trans-ethanol	CH_3CH_2OH	27(7,21) - 26(6,20)

Example table.

A.2 Rotation Diagram Analyses Parameters

The calculated parameters for the rotation diagram analyses can be found in the online data of 2021. An example of the first nine entries are shown in Table A.2. The entries are ordered by molecule name starting with methanol. Table A.2 includes

the molecule name, the catalog frequency in MHz, the rotational quantum numbers: *J'(Ka',Kc') - J(Ka,Kc)*, peak area, upper state energy (E_u) in K, y-values ($\ln(\gamma W C_\tau)$), and whether the transition is reported as predicted or experimentally measured in various spectral catalogs (e.g., CDMS or JPL).

TABLE A.2: Rotation Diagram Parameters

Molecule	Frequency (MHz)	Transition	Peak Area (K·MHz)	E_u (K)	y-value	P/E
Methanol	807508.194	13(7,6) - 14(6,8)	1972.013820	471.3191798	33.96321778	P
Methanol	807865.958	11(1,11) - 10(0,10)	76342.16587	166.3768396	35.80335572	P
Methanol	810291.478	19(8,11) - 20(7,14)	2089.324759	775.6054123	33.32670335	P
Methanol	810563.957	14(9,5) - 15(8,7)	842.4299628	652.311804	33.42394847	P
Methanol	811057.169	28(2,27) - 27(1,27)	1650.767186	1236.670497	31.50657567	P
Methanol	811247.845	12(6,6) - 11(7,4)	539.8764583	772.7872594	33.03504547	P
Methanol	811338.308	23(3,21) - 23(0,23)	585.1569982	688.4398919	33.48377331	P
Methanol	811444.546	8(2,6) - 7(1,7)	22750.39239	109.4996825	35.41524752	P
Methanol	812550.291	7(2,6) - 6(1,5)	29866.44381	102.7084283	35.76983897	P

Example table. P/E refers to Predicted or Experimental.

Bibliography

(2008). *Astrophys. J.* https://doi.org/10.1086/528947

(2021). *Astrophys. J.* https://doi.org/10.3847/1538-4357/abf14e

Abou Mrad, N., Duvernay, F., Chiavassa, T., & Danger, G. (2016). Methanol ice VUV photoprocessing: GC-MS analysis of volatile organic compounds. *Mon. Not. R. Astron. Soc.*, *458*(2), 1234–1241. https://doi.org/10.1093/mnras/stw346

Abou Mrad, N., Duvernay, F., Theulé, P., Chiavassa, T., & Danger, G. (2014). Development and optimization of an analytical system for volatile organic compound analysis coming from the heating of interstellar/cometary ice analogues [PMID: 25025518]. *Anal. Chem.*, *86*(16), 8391–8399. https://doi.org/10.1021/ac501974c

Abplanalp, M. J., Gozem, S., Krylov, A. I., Shingledecker, C. N., Herbst, E., & Kaiser, R. I. (2016). A study of interstellar aldehydes and enols as tracers of a cosmic ray-driven nonequilibrium synthesis of complex organic molecules. *PNAS*, *113*(28), 7727–7732. https://doi.org/10.1073/pnas.1604426113

Abplanalp, M. J., Góbi, S., & Kaiser, R. I. (2019). On the formation and the isomer specific detection of methylacetylene (CH_3CCH), propene (CH_3CHCH_2), cyclopropane (c-C_3H_6), vinylacetylene (CH_2CHCCH), and 1,3-butadiene ($CH_2CHCHCH_2$) from interstellar methane ice analogues. *Phys. Chem. Chem. Phys.*, *21*, 5378–5393. https://doi.org/10.1039/C8CP03921F

Allamandola, L., Sandford, S., & Valero, G. (1988). Photochemical and thermal evolution of interstellar/precometary ice analogs. *Icarus*, *76*(2), 225–252. https://doi.org/https://doi.org/10.1016/0019-1035(88)90070-X

Andersson, S., & van Dishoeck, E. F. (2008). Photodesorption of water ice - a molecular dynamics study. *Astron. Astrophys.*, *491*(3), 907–916. https://doi.org/10.1051/0004-6361:200810374

Arasa, C., Andersson, S., Cuppen, H. M., van Dishoeck, E. F., & Kroes, G.-J. (2010). Molecular dynamics simulations of the ice temperature dependence of water ice photodesorption. *J. Chem. Phys.*, *132*(18), 184510. https://doi.org/10.1063/1.3422213

Arasa, C., Koning, J., Kroes, G.-J., Walsh, C., & van Dishoeck, E. F. (2015). Photodesorption of H_2O, HDO, and D_2O ice and its impact on fractionation. *Astron. Astrophys.*, *575*, A121. https://doi.org/10.1051/0004-6361/201322695

Belloche, A., Menten, K. M., Comito, C., Müller, H. S. P., Schilke, P., Ott, J., Thorwirth, S., & Hieret, C. (2008). Detection of amino acetonitrile in Sgr B2(N). *Astron. Astrophys.*, *482*(1), 179–196. https://doi.org/10.1051/0004-6361:20079203

Belloche, A., Müller, H. S. P., Menten, K. M., Schilke, P., & Comito, C. (2013). Complex organic molecules in the interstellar medium: IRAM 30 m line survey of Sagittarius B2(N) and (M). *Astron. Astrophys.*, *559*, A47. https://doi.org/10.1051/0004-6361/201321096

Bergantini, A., Abplanalp, M. J., Pokhilko, P., Krylov, A. I., Shingledecker, C. N., Herbst, E., & Kaiser, R. I. (2018). A combined experimental and theoretical study on the formation of interstellar propylene oxide (CH_3CHCH_2O)—a chiral molecule. *Astrophys. J.*, *860*(2), 108. https://doi.org/10.3847/1538-4357/aac383

Bertin, M., Romanzin, C., Doronin, M., Philippe, L., Jeseck, P., Ligterink, N., Linnartz, H., Michaut, X., & Fillion, J.-H. (2016). UV photodesorption of methanol in pure and CO–rich ices: Desorption rates of the intact molecule and of the photofragments. *Astrophys. J., Lett.*, *817*(2), L12. https://doi.org/10.3847/2041-8205/817/2/l12

Bertin, M., Fayolle, E. C., Romanzin, C., Öberg, K. I., Michaut, X., Moudens, A., Philippe, L., Jeseck, P., Linnartz, H., & Fillion, J.-H. (2012). UV photodesorption of interstellar CO ice analogues: from subsurface excitation to surface desorption. *Phys. Chem. Chem. Phys.*, *14*(28), 9929. https://doi.org/10.1039/C2CP41177F

Bertin, M., Fayolle, E. C., Romanzin, C., Poderoso, H. A. M., Michaut, X., Philippe, L., Jeseck, P., Öberg, K. I., Linnartz, H., & Fillion, J.-H. (2013). Indirect Ultraviolet

Photodesorption from CO:N_2 Binary Ices — an Efficient Grain-gas Process. *Astrophys. J.*, *779*(2), 120. https://doi.org/10.1088/0004-637X/779/2/120

Biver, N., & Bockelée-Morvan, D. (2019). Complex organic molecules in comets from remote-sensing observations at millimeter wavelengths. *ACS Earth Space Chem.*, *3*(8), 1550–1555. https://doi.org/10.1021/acsearthspacechem.9b00130

Blum, J., & Wurm, G. (2008). The growth mechanisms of macroscopic bodies in protoplanetary disks. *Annu. Rev. Astron. Astrophys.*, *46*(1), 21–56. https://doi.org/10.1146/annurev.astro.46.060407.145152

Bockelée-Morvan, D., Lis, D. C., Wink, J. E., Despois, D., & Crovisier, J. e. a. (2000). New molecules found in comet C/1995 O1 (Hale-Bopp). *Astron. Astrophys.*, *353*, 1101–1114.

Bolina, A. S., Wolff, A. J., & Brown, W. A. (2005a). Reflection absorption infrared spectroscopy and temperature programmed desorption investigations of the interaction of methanol with a graphite surface. *J. Chem. Phys.*, *122*(4), 044713. https://doi.org/10.1063/1.1839554

Bolina, A. S., Wolff, A. J., & Brown, W. A. (2005b). Reflection absorption infrared spectroscopy and temperature-programmed desorption studies of the adsorption and desorption of amorphous and crystalline water on a graphite surface [PMID: 16853142]. *J. Phys. Chem. B*, *109*(35), 16836–16845. https://doi.org/10.1021/jp0528111

Bonfand, M., Belloche, A., Garrod, R. T., Menten, K. M., Willis, E., Stéphan, G., & Müller, H. S. P. (2019). The complex chemistry of hot cores in Sgr B2(N): Influence of cosmic-ray ionization and thermal history. *Astron. Astrophys.*, *628*, A27. https://doi.org/10.1051/0004-6361/201935523

Boogert, A. A., Gerakines, P. A., & Whittet, D. C. (2015). Observations of the icy universe. *Ann. Rev. Astron. Astrophys.*, *53*(1), 541–581. https://doi.org/10.1146/annurev-astro-082214-122348

Buhl, D., & Snyder, L. E. (1970). Unidentified Interstellar Microwave Line. *Nature*, *228*(5268), 267–269. https://doi.org/10.1038/228267a0

Burke, D. J., & Brown, W. A. (2010). Ice in space: Surface science investigations of the thermal desorption of model interstellar ices on dust grain analogue surfaces. *Phys. Chem. Chem. Phys.*, *12*, 5947–5969. https://doi.org/10.1039/B917005G

Burkhardt, A. M., Lee, K. L. K., Changala, P. B., Shingledecker, C. N., Cooke, I. R., Loomis, R. A., Wei, H., Charnley, S. B., Herbst, E., McCarthy, M. C., & McGuire, B. A. (2021). Discovery of the pure polycyclic aromatic hydrocarbon indene (c-C_9H_8) with GOTHAM observations of TMC-1. *Astrophys. J., Lett.*, *913*(2), L18. https://doi.org/10.3847/2041-8213/abfd3a

Butscher, T., Duvernay, F., Danger, G., & Chiavassa, T. (2016). Radical-induced chemistry from VUV photolysis of interstellar ice analogues containing formaldehyde. *Astron. Astrophys.*, *593*, A60. https://doi.org/10.1051/0004-6361/201628258

Cami, J., Bernard-Salas, J., Peeters, E., & Malek, S. E. (2010). Detection of C_{60} and C_{70} in a young planetary nebula. *Science*, *329*(5996), 1180–1182. https://doi.org/10.1126/science.1192035

Carrascosa, H., Caro, G. M. M., González-díaz, C., Suevos, J., & Chen, Y.-J. (2021a). The intriguing behavior of ultraviolet photodesorption and color temperature of astrophysical CO ice analogs: A possible indication of molecular disorder. *Astrophys. J.*, *916*(1), 1. https://doi.org/10.3847/1538-4357/ac0a7a

Carrascosa, H, Gonzalez Diaz, C, Muñoz *Caro*, *G.M.*, Gomez, P. C., & Sanz, M. L. (2021b). Synthesis of the first nitrogen-heterocycles in interstellar ice analogues containing methylamine (CH_3NH_2) exposed to UV radiation: formation of trimethylentriamine (TMT, c-(-CH_2-NH)$_3$) and hexamethylentetramine (HMT, $(CH_2)_6N_4$). *Mon. Not. R. Astron. Soc.*, *506*(1), 791–805. https://doi.org/10.1093/mnras/stab1710

Chaix, L., van den Bergh, H., & Rossi, M. J. (1998). Real-time kinetic measurements of the condensation and evaporation of D_2O molecules on ice at 140 K >T>220 K. *J. Phys. Chem. A*, *102*(50), 10300–10309. https://doi.org/10.1021/jp983050n

Chakarov, D., Österlund, L, & Kasemo, B. (1995). Water adsorption on graphite (0001). *Vacuum*, *46*(8), 1109–1112. https://doi.org/https://doi.org/10.1016/0042-207X(95)00117-4

Chaparro Molano, G., & Kamp, I. (2012). The role of OH in the chemical evolution of protoplanetary disks - I. The comet-forming region. *Astron. Astrophys.*, *537*, A138. https://doi.org/10.1051/0004-6361/201015868

Chen, Y.-J., Chuang, K.-J., Caro, G. M. M., Nuevo, M., Chu, C.-C., Yih, T.-S., Ip, W.-H., & Wu, C.-Y. R. (2013). Vacuum ultraviolet emission spectrum measurement of a microwave-discharge hydrogen-flow lamp in several configurations: Application to photodesorption of CO ice. *Astrophys. J.*, *781*(1), 15. https://doi.org/10.1088/0004-637x/781/1/15

Chen, Y. J., Chuang, K. J., Muñoz Caro, G. M., Nuevo, M., Chu, C. C., Yih, T. S., Ip, W. H., & Wu, C. Y. R. (2014). Vacuum Ultraviolet Emission Spectrum Measurement of a Microwave-discharge Hydrogen-flow Lamp in Several Configurations: Application to Photodesorption of CO Ice. *Astrophys. J.*, *781*(1), Article 15, 15. https://doi.org/10.1088/0004-637X/781/1/15

Cochran, A. L., Levasseur-Regourd, A.-C., Cordiner, M., Hadamcik, E., Lasue, J., Gicquel, A., Schleicher, D. G., Charnley, S. B., Mumma, M. J., Paganini, L., Bockelée-Morvan, D., Biver, N., & Kuan, Y.-J. (2015). The composition of comets. *Space Sci. Rev.*, *197*(1), 9–46. https://doi.org/10.1007/s11214-015-0183-6

Crockett, N. R., Bergin, E. A., Wang, S., Lis, D. C., Bell, T. A., Blake, G. A., Boogert, A., Bumble, B., Cabrit, S., Caux, E., Ceccarelli, C., Cernicharo, J., Comito, C., Daniel, F., Dubernet, M.-L., Emprechtinger, M., Encrenaz, P., Falgarone, E., Gerin, M., … Zmuidzinas, J. (2010). Herschel observations of extra-ordinary sources (HEXOS): The terahertz spectrum of Orion KL seen at high spectral resolution*. *Astron. Astrophys.*, *521*, L21. https://doi.org/10.1051/0004-6361/201015116

Crockett, N. R., Bergin, E. A., Neill, J. L., Favre, C., Schilke, P., Lis, D. C., Bell, T. A., Blake, G., Cernicharo, J., Emprechtinger, M., Esplugues, G. B., Gupta, H., Kleshcheva, M., Lord, S., Marcelino, N., McGuire, B. A., Pearson, J., Phillips, T. G., Plume, R., … Yu, S. (2014). Herschel observations of extraordinary sources: Analysis of the HIFI 1.2 THz wide spectral survey toward Orion KL. I. Methods. *Astrophys. J.*, *787*(2), 112. https://doi.org/10.1088/0004-637x/787/2/112

Cruz-Diaz, G. A., Martín-Doménech, R., Muñoz Caro, G. M., & Chen, Y.-J. (2016). Negligible photodesorption of methanol ice and active photon-induced desorption of its irradiation products. *Astron. Astrophys.*, *592*, A68. https://doi.org/10.1051/0004-6361/201526761

Cruz-Diaz, G. A., Martín-Doménech, R., Moreno, E., Muñoz Caro, G. M., & Chen, Y.-J. (2017). New measurements on water ice photodesorption and product formation under ultraviolet irradiation. *Mon. Not. R. Astron. Soc.*, *474*(3), 3080–3089. https://doi.org/10.1093/mnras/stx2966

Davila, A. F., Fairén, A. G., Gago-Duport, L., Stoker, C., Amils, R., Bonaccorsi, R., Zavaleta, J., Lim, D., Schulze-Makuch, D., & McKay, C. P. (2008). Subsurface formation of oxidants on Mars and implications for the preservation of organic biosignatures. *Earth Planet. Sci. Lett.*, *272*(1), 456–463. https://doi.org/https://doi.org/10.1016/j.epsl.2008.05.015

Dohnlek, Z., Ciolli, R. L., Kimmel, G. A., Stevenson, K. P., Smith, R. S., & Kay, B. D. (1999). Substrate induced crystallization of amorphous solid water at low temperatures. *J. Chem. Phys.*, *110*(12), 5489–5492. https://doi.org/10.1063/1.478446

Drouin, B. J., Tang, A., Schlecht, E., Brageot, E., Gu, Q. J., Ye, Y., Shu, R., Frank Chang, M.-c., & Kim, Y. (2016). A CMOS millimeter-wave transceiver embedded in a semi-confocal Fabry-Perot cavity for molecular spectroscopy. *J. Chem. Phys.*, *145*(7), 074201. https://doi.org/10.1063/1.4961020

Drozdovskaya, M. N., van Dishoeck, E. F., Jørgensen, J. K., Calmonte, U., van der Wiel, M. H. D., Coutens, A., Calcutt, H., Müller, H. S. P., Bjerkeli, P., Persson, M. V., Wampfler, S. F., & Altwegg, K. (2018). The ALMA-PILS survey: the sulphur connection between protostars and comets: IRAS 16293–2422 B and 67P/Churyumov–Gerasimenko. *Mon. Not. R. Astron. Soc.*, *476*(4), 4949–4964. https://doi.org/10.1093/mnras/sty462

Drozdovskaya, M. N., van Dishoeck, E. F., Rubin, M., Jørgensen, J. K., & Altwegg, K. (2019). Ingredients for solar-like systems: protostar IRAS 16293-2422 B versus comet 67P/Churyumov–Gerasimenko. *Mon. Not. R. Astron. Soc.*, *490*(1), 50–79. https://doi.org/10.1093/mnras/stz2430

Dulieu, F., Amiaud, L., Congiu, E., Fillion, J.-H., Matar, E., Momeni, A., Pirronello, V., & Lemaire, J. L. (2010). Experimental evidence for water formation on interstellar dust grains by hydrogen and oxygen atoms. *Astron. Astrophys.*, *512*, A30. https://doi.org/10.1051/0004-6361/200912079

Fayolle, E. C., Bertin, M., Romanzin, C., Michaut, X., Öberg, K. I., Linnartz, H., & Fillion, J.-H. (2011). CO Ice Photodesorption: A Wavelength-dependent Study. *Astrophys. J., Lett.*, *739*(2), Article L36, L36. https://doi.org/10.1088/2041-8205/739/2/L36

Fedoseev, G., Ioppolo, S., Zhao, D., Lamberts, T., & Linnartz, H. (2014). Low-temperature surface formation of NH_3 and HNCO: hydrogenation of nitrogen atoms in CO-rich interstellar ice analogues. *Mon. Not. R. Astron. Soc.*, *446*(1), 439–448. https://doi.org/10.1093/mnras/stu2028

Fillion, J.-H., Dupuy, R., Féraud, G., Romanzin, C., Philippe, L., Putaud, T., Baglin, V., Cimino, R., Marie-Jeanne, P., Jeseck, P., Michaut, X., & Bertin, M. (2021). Vacuum-UV photodesorption from compact Amorphous Solid Water : photon energy, isotopic and temperature effects. *arXiv e-prints*, Article arXiv:2103.15435, arXiv:2103.15435.

Fraser, H. J., Collings, M. P., McCoustra, M. R. S., & Williams, D. A. (2001). Thermal desorption of water ice in the interstellar medium. *Mon. Not. R. Astron. Soc.*, *327*(4), 1165–1172. https://doi.org/10.1046/j.1365-8711.2001.04835.x

Fulvio, D., Brieva, A. C., Cuylle, S. H., Linnartz, H., Jäger, C., & Henning, T. (2014). A straightforward method for vacuum-ultraviolet flux measurements: The case of the hydrogen discharge lamp and implications for solid-phase actinometry. *Appl. Phys. Lett.*, *105*(1), 014105. https://doi.org/10.1063/1.4887067

Garrod, R. T., Weaver, S. L. W., & Herbst, E. (2008). Complex chemistry in star-forming regions: An expanded gas-grain warm-up chemical model. *Astrophys. J.*, *682*(1), 283–302. https://doi.org/10.1086/588035

Gerakines, P., Moore, M., & Hudson, R. (2004). Ultraviolet photolysis and proton irradiation of astrophysical ice analogs containing hydrogen cyanide. *Icarus*, *170*(1), 202–213. https://doi.org/https://doi.org/10.1016/j.icarus.2004.02.005

Gerakines, P., Schutte, W. A., & Ehrenfreund, P. (1996). Ultraviolet processing of interstellar ice analogs. I. Pure ices. *Astron. Astrophys.*, *312*, 289–305.

Gerecht, E., Douglass, K. O., & Plusquellic, D. F. (2011). Chirped-pulse terahertz spectroscopy for broadband trace gas sensing. *Opt. Express*, *19*(9), 8973–8984. https://doi.org/10.1364/OE.19.008973

Gibb, E. L., Whittet, D. C. B., Boogert, A. C. A., & Tielens, A. G. G. M. (2004). Interstellar ice: The Infrared Space Observatory legacy. *Astrophys. J., Suppl. Ser.*, *151*(1), 35–73. https://doi.org/10.1086/381182

Goldsmith, P. F., & Langer, W. D. (1999). Population diagram analysis of molecular line emission. *Astrophys. J.*, *517*(1), 209–225. https://doi.org/10.1086/307195

González Díaz, C, Carrascosa de Lucas, H, Aparicio, S, Muñoz Caro, G. M., Sie, N.-E., Hsiao, L.-C., Cazaux, S, & Chen, Y.-J. (2019). Accretion and photodesorption of CO ice as a function of the incident angle of deposition. *Mon. Not. R. Astron. Soc.*, *486*(4), 5519–5525. https://doi.org/10.1093/mnras/stz1223

Gordy, W., & Cook, R. L. (1984). *Microwave molecular spectra*. New York: Wiley.

Gredel, R., Lepp, S., Dalgarno, A., & Herbst, E. (1989). Cosmic-Ray–induced Photodissociation and Photoionization Rates of Interstellar Molecules. *Astrophys. J.*, *347*, 289. https://doi.org/10.1086/168117

Green, S. D., Bolina, A. S., Chen, R., Collings, M. P., Brown, W. A., & McCoustra, M. R. S. (2009). Applying laboratory thermal desorption data in an interstellar context: Sublimation of methanol thin films. *Mon. Not. R. Astron. Soc.*, *398*(1), 357–367. https://doi.org/10.1111/j.1365-2966.2009.15144.x

Greenberg, J., Yencha, A., Corbett, J., & Frisch, H. (1972). Ultraviolet effects on the chemical composition and optical properties of interstellar grains. *Mem. Soc. Roy. Sciences Liege*, *6e serie*(Tome III), 425–436.

Guélin, M., Cernicharo, J., Travers, M. J., McCarthy, M. C., Gottlieb, C. A., Thaddeus, P., Ohishi, M., Saito, S., & Yamamoto, S. (1997). Detection of a new linear carbon chain radical: C_7H. *Astron. Astrophys.*, *317*, L1–L4.

Haenecour, P., Floss, C., José, J., Amari, S., Lodders, K., Jadhav, M., Wang, A., & Gyngard, F. (2016). Coordinated analysis of two graphite grains from the CO 3.0 LAP 031117 meteorite: First identification of a CO nova graphite and a

presolar iron sulfide subgrain. *825*(2), 88. https://doi.org/10.3847/0004-637x/825/2/88

Haynes, D. R., Tro, N. J., & George, S. M. (1992). Condensation and evaporation of water on ice surfaces. *J. Phys. Chem.*, *96*(21), 8502–8509. https://doi.org/10.1021/j100200a055

Henderson, B. L., & Gudipati, M. S. (2015). Direct detection of complex organic products in ultraviolet (Lyman-a) and electron-irradiated astrophysical and cometary ice analogs using two-step laser ablation and ionization mass spectrometry. *Astrophys. J.*, *800*(1), 66. https://doi.org/10.1088/0004-637x/800/1/66

Herbst, E. (2017). The synthesis of large interstellar molecules. *Int. Rev. Phys. Chem.*, *36*(2), 287–331. https://doi.org/10.1080/0144235X.2017.1293974

Hudson, R. L., Loeffler, M. J., & Yocum, K. M. (2017). Laboratory investigations into the spectra and origin of propylene oxide: A chiral interstellar molecule. *Astrophys. J.*, *835*(2), 225. https://doi.org/10.3847/1538-4357/835/2/225

Hudson, R. L. (2017). An IR investigation of solid amorphous ethanol — Spectra, properties, and phase changes. *Spectrochim. Acta, Part A*, *187*, 82 –86. https://doi.org/https://doi.org/10.1016/j.saa.2017.06.027

Hudson, R. L., & Ferrante, R. F. (2019). Quantifying acetaldehyde in astronomical ices and laboratory analogues: IR spectra, intensities, ^{13}C shifts, and radiation chemistry. *Mon. Not. R. Astron. Soc.*, *492*(1), 283–293. https://doi.org/10.1093/mnras/stz3323

Hudson, R. L., Gerakines, P. A., & Ferrante, R. F. (2018). IR spectra and properties of solid acetone, an interstellar and cometary molecule. *Spectrochim. Acta, Part A*, *193*, 33 –39. https://doi.org/https://doi.org/10.1016/j.saa.2017.11.055

Hudson, R. L., Moore, M. H., & Cook, A. M. (2005). IR characterization and radiation chemistry of glycolaldehyde and ethylene glycol ices [Space Life Sciences: Astrobiology: Steps toward Origin of Life and Titan before Cassini]. *Adv. Space Res.*, *36*(2), 184 –189. https://doi.org/https://doi.org/10.1016/j.asr.2005.01.017

Hudson, R. L., Yarnall, Y. Y., & Coleman, F. M. (2020). Infrared band strengths and other properties of amorphous and crystalline dimethyl ether. *Spectrochim.*

Acta, Part A, *233*, 118217. https://doi.org/https://doi.org/10.1016/j.saa.2020.118217

Hudson, R., & Donn, B. (1991). An experimental study of the sublimation of water ice and the release of trapped gases. *Icarus*, *94*(2), 326–332. https://doi.org/https://doi.org/10.1016/0019-1035(91)90231-H

Hudson, R., & Moore, M. (2000). IR spectra of irradiated cometary ice analogues containing methanol: A new assignment, a reassignment, and a nonassignment. *Icarus*, *145*(2), 661 –663. https://doi.org/https://doi.org/10.1006/icar.2000.6377

Ishibashi, A., Hidaka, H., Oba, Y., Kouchi, A., & Watanabe, N. (2021). Efficient formation pathway of methyl formate: The role of OH radicals on ice dust. *Astrophys. J., Lett.*, *921*(1), L13. https://doi.org/10.3847/2041-8213/ac3005

Jimenez-Serra, I., Martin-Pintado, J., Rivilla, V. M., Rodriguez-Almeida, L., Alonso Alonso, E. R., Zeng, S., Cocinero, E. J., Martín, S., Requena-Torres, M., Martin-Domenech, R., & Testi, L. (2020). Toward the RNA-World in the interstellar medium—detection of urea and search of 2-amino-oxazole and simple sugars. *Astrobiology*, *20*(9), 1048–1066. https://doi.org/10.1089/ast.2019.2125

Klemperer, W. (1970). Carrier of the Interstellar 89.190 GHz Line. *Nature*, *227*(5264), 1230. https://doi.org/10.1038/2271230a0

Laas, J. C., Garrod, R. T., Herbst, E., & Weaver, S. L. W. (2011). Controbutions from grain surface and gas phase chemistry to the formation of methyl formate and its structural isomers. *Astrophys. J.*, *728*(1), 71. https://doi.org/10.1088/0004-637x/728/1/71

Laas, J. C., Hays, B. M., & Widicus Weaver, S. L. (2013). Multipass millimeter/submillimeter spectrometer to probe dissociative reaction dynamics [PMID: 23678971]. *J. Phys. Chem. A*, *117*(39), 9548–9554. https://doi.org/10.1021/jp3122402

Lecacheux, A., Biver, N., Crovisier, J., Bockelée-Morvan, D., Baron, P., Booth, R. S., Encrenaz, P., Florén, H.-G., Frisk, U., Hjalmarson, A., Kwok, S., Mattila, K., Nordh, L., Olberg, M., Olofsson, A. O. H., Rickman, H., Sandqvist, Aa., von Schéele, F., Serra, G., … Winnberg, A. (2003). Observations of water in comets with Odin. *Astron. Astrophys.*, *402*(3), L55–L58. https://doi.org/10.1051/0004-6361:20030338

Lee, C.-W., Kim, J.-K., Moon, E.-S., Minh, Y. C., & Kang, H. (2009). Formation of glycine on ultraviolet-irradiated interstellar ice-analog films and implications for interstellar amino acids. *Astron. Astrophys.*, *697*(1), 428–435. https://doi.org/10.1088/0004-637x/697/1/428

Luna, R., Molpeceres, G., Ortigoso, J., Satorre, M. A., Domingo, M., & Maté, B. (2018). Densities, infrared band strengths, and optical constants of solid methanol. *Astron. Astrophys.*, *617*, A116. https://doi.org/10.1051/0004-6361/201833463

Maity, S., Kaiser, R. I., & Jones, B. M. (2015). Formation of complex organic molecules in methanol and methanol–carbon monoxide ices exposed to ionizing radiation – a combined FTIR and reflectron time-of-flight mass spectrometry study. *Phys. Chem. Chem. Phys.*, *17*, 3081–3114. https://doi.org/10.1039/C4CP04149F

Martín-Doménech, R., Muñoz Caro, G. M., & Cruz-Díaz, G. A. (2016). Study of the photon-induced formation and subsequent desorption of CH_3OH and H_2CO in interstellar ice analogs. *Astron. Astrophys.*, *589*, A107. https://doi.org/10.1051/0004-6361/201528025

McGuire, B. A., Carroll, P. B., Loomis, R. A., Finneran, I. A., Jewell, P. R., Remijan, A. J., & Blake, G. A. (2016). Discovery of the interstellar chiral molecule propylene oxide (ch_3chch_2o). *Science*, *352*(6292), 1449–1452. https://doi.org/10.1126/science.aae0328

McKellar, A. (1940). Evidence for the molecular origin of some hitherto unidentified interstellar lines. *Publ. Astron. Soc. Pac.*, *52*(307), 187. https://doi.org/10.1086/125159

Meinert, C., Myrgorodska, I., de Marcellus, P., Buhse, T., Nahon, L., Hoffmann, S. V., d'Hendecourt, L. L. S., & Meierhenrich, U. J. (2016). Ribose and related sugars from ultraviolet irradiation of interstellar ice analogs. *Science*, *352*(6282), 208–212. https://doi.org/10.1126/science.aad8137

Melosso, M., Dore, L., Tamassia, F., Brogan, C. L., Hunter, T. R., & McGuire, B. A. (2020). The submillimeter rotational spectrum of ethylene glycol up to 890 GHz and application to ALMA band 10 spectral line data of NGC 6334I [PMID: 31801346]. *J. Phys. Chem. A*, *124*(1), 240–246. https://doi.org/10.1021/acs.jpca.9b10803

Mitchell, E., Raut, U., Fulvio, D., Schaible, M., Dukes, C., & Baragiola, R. (2013). Ultraviolet photodesorption as a driver of water migration on the lunar surface. *Planet. Space Sci.*, *89*, 42–46. https://doi.org/https://doi.org/10.1016/j.pss.2013.02.002

Modica, P., & Palumbo, M. E. (2010). Formation of methyl formate after cosmic ion irradiation of icy grain mantles. *Astron. Astrophys.*, *519*, A22. https://doi.org/10.1051/0004-6361/201014101

Moore, M. H., Donn, B., Khanna, R., & A'Hearn, M. F. (1983). Studies of proton-irradiated cometary-type ice mixtures. *Icarus*, *54*(3), 388–405. https://doi.org/https://doi.org/10.1016/0019-1035(83)90236-1

Moreno, R., Lellouch, E., Cavalié, T., & Moullet, A. (2017). Detection of CS in Neptune's atmosphere from ALMA observations. *Astron. Astrophys.*, *608*, L5. https://doi.org/10.1051/0004-6361/201731472

Muñoz Caro, G. M., Chen, Y.-J., Aparicio, S., Jiménez-Escobar, A., Rosu-Finsen, A., Lasne, J., & McCoustra, M. R. S. (2016). Photodesorption and physical properties of CO ice as a function of temperature. *Astron. Astrophys.*, *589*, A19. https://doi.org/10.1051/0004-6361/201628121

Muñoz Caro, G. M., Jiménez-Escobar, A., Martín-Gago, J. Á., Rogero, C., Atienza, C., Puertas, S., Sobrado, J. M., & Torres-Redondo, J. (2010). New results on thermal and photodesorption of CO ice using the novel InterStellar Astrochemistry Chamber (ISAC). *Astron. Astrophys.*, *522*, Article A108, A108. https://doi.org/10.1051/0004-6361/200912462

Nishimura, S. Y., Gibbons, R. F., & Tro, N. J. (1998). Desorption kinetics of methanol from Al_2O_3(0001) studied using temperature-programmed desorption and isothermal desorption. *J. Phys. Chem. B*, *102*(35), 6831–6834. https://doi.org/10.1021/jp981624i

Nittler, L. R., Alexander, C. M., Davidson, J., Riebe, M. E., Stroud, R. M., & Wang, J. (2018). High abundances of presolar grains and 15n-rich organic matter in CO3.0 chondrite Dominion Range 08006. *Geochim. Cosmochim. Acta*, *226*, 107–131. https://doi.org/https://doi.org/10.1016/j.gca.2018.01.038

Nittler, L. R., Stroud, R. M., Alexander, C. M. O., & Howell, K. (2020). Presolar grains in primitive ungrouped carbonaceous chondrite northwest africa 5958. *Meteorit. Planet. Sci.*, *55*(6), 1160–1175. https://doi.org/https://doi.org/10.1111/maps.13397

Öberg, K. I., Garrod, R. T., van Dishoeck, E. F., & Linnartz, H. (2009a). Formation rates of complex organics in UV irradiated CH_3OH-rich ices - I. Experiments. *Astron. Astrophys.*, *504*(3), 891–913. https://doi.org/10.1051/0004-6361/200912559

Öberg, K. I., Linnartz, H., Visser, R., & van Dishoeck, E. F. (2009b). Photodesorption of Ices. II. H_2O and D_2O. *Astrophys. J.*, *693*(2), 1209–1218. https://doi.org/10.1088/0004-637x/693/2/1209

Öberg, K. I., van Dishoeck, E. F., & Linnartz, H. (2009c). Photodesorption of ices I: CO, N_2, and CO_2. *A&A*, *496*(1), 281–293. https://doi.org/10.1051/0004-6361/200810207

Öberg, K. I., Boogert, A. C. A., Pontoppidan, K. M., van den Broek, S., van Dishoeck, E. F., Bottinelli, S., Blake, G. A., & Evans, N. J. (2011). The Spitzer ice legacy: Ice evolution from cores to protostars. *Astrophys. J.*, *740*(2), 109. https://doi.org/10.1088/0004-637x/740/2/109

Öberg, K. I., Fuchs, G. W., Awad, Z., Fraser, H. J., Schlemmer, S., van Dishoeck, E. F., & Linnartz, H. (2007). Photodesorption of CO ice. *Astrophys. J.*, *662*(1), L23–L26. https://doi.org/10.1086/519281

Oka, A., Nakamoto, T., & Ida, S. (2011). Evolution of snow line in optically thick protoplanetary disks: Effects of water ice opacity and dust grain size. *Astrophys. J.*, *738*(2), 141. https://doi.org/10.1088/0004-637x/738/2/141

Paardekooper, D. M., Bossa, J.-B., & Linnartz, H. (2016a). Laser desorption time-of-flight mass spectrometry of vacuum UV photo-processed methanol ice. *Astron. Astrophys.*, *592*, A67. https://doi.org/10.1051/0004-6361/201527937

Paardekooper, D. M., Fedoseev, G., Riedo, A., & Linnartz, H. (2016b). A novel approach to measure photodesorption rates of interstellar ice analogues - The photodesorption rate of CO ice reinvestigated. *Astron. Astrophys.*, *596*, A72. https://doi.org/10.1051/0004-6361/201629063

Paardekooper, D. M., Fedoseev, G., Riedo, A., & Linnartz, H. (2016c). A novel approach to measure photodesorption rates of interstellar ice analogues - the photodesorption rate of co ice reinvestigated. *A&A*, *596*, A72. https://doi.org/10.1051/0004-6361/201629063

Parks, M. C., Nixon, C. A., Villanueva, G. L., Smith, M. D., Khayat, A. S. J., Thelen, A. E., Villard, E., Charnley, S. B., & Irwin, P. G. J. (2021). Observations of Mars with ALMA: potential for future constraints of global circulation models. *Journal of Astronomical Telescopes, Instruments, and Systems*, *7*(2), 1 – 14. https://doi.org/10.1117/1.JATIS.7.2.025001

Paulive, A., Shingledecker, C. N., & Herbst, E. (2020). The role of radiolysis in the modelling of $C_2H_4O_2$ isomers and dimethyl ether in cold dark clouds. *Mon. Not. R. Astron. Soc.*, *500*(3), 3414–3424. https://doi.org/10.1093/mnras/staa3458

Porterfield, D. W., Hesler, J. L., Densing, R., Mueller, E. R., Crowe, T. W., & Weikle, R. M. (1994). Resonant metal-mesh bandpass filters for the far infrared. *Appl. Opt.*, *33*(25), 6046–6052. https://doi.org/10.1364/AO.33.006046

Prasad, S. S., & Tarafdar, S. P. (1983). UV radiation field inside dense clouds - Its possible existence and chemical implications. *Astrophys. J.*, *267*, 603–609. https://doi.org/10.1086/160896

Pravdivtseva, O., Tissot, F. L. H., Dauphas, N., & Amari, S. (2020). Evidence of presolar SiC in the Allende Curious Marie calcium–aluminium-rich inclusion. *Nature Astronomy*, *4*(6), 617–624. https://doi.org/10.1038/s41550-019-1000-z

Price, R. J., Viti, S., & Williams, D. A. (2003). On the origin of diffuse clouds. *Mon. Not. R. Astron. Soc.*, *343*(4), 1257–1262. https://doi.org/10.1046/j.1365-8711.2003.06762.x

Qasim, D., Fedoseev, G., Chuang, K.-J., He, J., Ioppolo, S., van Dishoeck, E. F., & Linnartz, H. (2020). An experimental study of the surface formation of methane in interstellar molecular clouds. *Nature Astronomy*, *4*(8), 781–785. https://doi.org/10.1038/s41550-020-1054-y

Roth, N. X., Milam, S. N., Cordiner, M. A., Bockelée-Morvan, D., DiSanti, M. A., Boissier, J., Biver, N., Crovisier, J., Russo, N. D., Bonev, B. P., Qi, C., Remijan, A. J., Charnley, S. B., Gibb, E. L., de Val-Borro, M., & Jehin, E. (2021). Rapidly

varying anisotropic methanol (CH_3OH) production in the inner coma of Comet 46P/Wirtanen as revealed by the ALMA Atacama Compact Array. *Planet. Sci. J.*, *2*(2), 55. https://doi.org/10.3847/psj/abdd3a

Rubin, M., Altwegg, K., Balsiger, H., Berthelier, J.-J., Combi, M. R., De Keyser, J., Drozdovskaya, M., Fiethe, B., Fuselier, S. A., Gasc, S., Gombosi, T. I., Hänni, N., Hansen, K. C., Mall, U., Rème, H., Schroeder, I. R. H. G., Schuhmann, M., Sémon, T., Waite, J. H., … Wurz, P. (2019a). Elemental and molecular abundances in comet 67P/Churyumov-Gerasimenko. *Mon. Not. R. Astron. Soc.*, *489*(1), 594–607. https://doi.org/10.1093/mnras/stz2086

Rubin, M., Bekaert, D. V., Broadley, M. W., Drozdovskaya, M. N., & Wampfler, S. F. (2019b). Volatile species in comet 67P/Churyumov-Gerasimenko: Investigating the link from the ism to the terrestrial planets. *ACS Earth Space Chem.*, *3*(9), 1792–1811. https://doi.org/10.1021/acsearthspacechem.9b00096

Sack, N. J., & Baragiola, R. A. (1993). Sublimation of vapor-deposited water ice below 170 K, and its dependence on growth conditions. *Phys. Rev. B*, *48*, 9973–9978. https://doi.org/10.1103/PhysRevB.48.9973

Sandford, S. A., & Allamandola, L. J. (1988). The condensation and vaporization behavior of H_2O: CO ices and implications for interstellar grains and cometary activity. *Icarus*, *76*(2), 201–224. https://doi.org/https://doi.org/10.1016/0019-1035(88)90069-3

Sandford, S. A., & Allamandola, L. J. (1993). Condensation and vaporization studies of CH_3OH and NH_3 ices: Major implications for astrochemistry. *Astrophys. J.*, *417*(2), 815–825.

Schmitz, P., Polta, J., Chang, S.-L., & Thiel, P. (1987). Isotope effect in water desorption from Ru(001). *Surf. Sci.*, *186*(1), 219–231. https://doi.org/https://doi.org/10.1016/S0039-6028(87)80044-4

Schneider, H., Caldwell-Overdier, A., Coppieters 't Wallant, S., Dau, L., Huang, J., Nwolah, I., Kasule, M., Buffo, C., Mullikin, E., Widdup, L., Hay, A., Bao, S. T., Perea, J., Thompson, M., Tano-Menka, R., Van Tuyl, M., Wang, A., Bussey, S., Sachdev, N., … Arumainayagam, C. R. (2019). Detection of methoxymethanol as a photochemistry product of condensed methanol. *Mon. Not. R. Astron. Soc.: Lett.*, *485*(1), L19–L23. https://doi.org/10.1093/mnrasl/slz019

Schutte, W., Allamandola, L., & Sandford, S. (1993). An experimental study of the organic molecules produced in cometary and interstellar ice analogs by thermal formaldehyde reactions. *Icarus*, *104*(1), 118–137. https://doi.org/https://doi.org/10.1006/icar.1993.1087

Shingledecker, C. N., & Herbst, E. (2018a). A general method for the inclusion of radiation chemistry in astrochemical models. *Phys. Chem. Chem. Phys.*, *20*, 5359–5367. https://doi.org/10.1039/C7CP05901A

Shingledecker, C. N., Tennis, J., Gal, R. L., & Herbst, E. (2018b). On cosmic-ray-driven grain chemistry in cold core models. *Astrophys. J.*, *861*(1), 20. https://doi.org/10.3847/1538-4357/aac5ee

Smith, J. A., Livingston, F. E., & George, S. M. (2003). Isothermal desorption kinetics of crystalline H_2O, $H_2^{18}O$, and D_2O ice multilayers. *J. Phys. Chem. B*, *107*(16), 3871–3877. https://doi.org/10.1021/jp022503s

Smith, R. S., & Kay, B. D. (1997). Molecular beam studies of kinetic processes in nanoscale water films. *Surf. Rev. Lett.*, *04*(04), 781–797. https://doi.org/10.1142/S0218625X97000766

Smith, R. S., Huang, C., Wong, E., & Kay, B. D. (1996). Desorption and crystallization kinetics in nanoscale thin films of amorphous water ice. *Surf. Sci.*, *367*(1), L13–L18. https://doi.org/https://doi.org/10.1016/S0039-6028(96)00943-0

Speedy, R. J., Debenedetti, P. G., Smith, R. S., Huang, C., & Kay, B. D. (1996). The evaporation rate, free energy, and entropy of amorphous water at 150 K. *J. Chem. Phys.*, *105*(1), 240–244. https://doi.org/10.1063/1.471869

Swings, P., & Rosenfeld, L. (1937). Considerations Regarding Interstellar Molecules. *Astrophys. J.*, *86*, 483–486. https://doi.org/10.1086/143880

Tempelmeyer, K. E., & Mills, D. W. (1968). Refractive index of carbon dioxide cryodeposit. *J. Appl. Phys.*, *39*(6), 2968–2969. https://doi.org/10.1063/1.1656707

Terada, H., & Tokunaga, A. T. (2017). Multi-epoch detections of water ice absorption in edge-on disks around Herbig Ae stars: PDS 144N AND PDS 453. *Astrophys. J.*, *834*(2), 115. https://doi.org/10.3847/1538-4357/834/2/115

Tercero, B., Cuadrado, S., López, A., Brouillet, N., Despois, D., & Cernicharo, J. (2018). Chemical segregation of complex organic O-bearing species in Orion KL. *Astron. Astrophys.*, *620*, L6. https://doi.org/10.1051/0004-6361/201834417

Theulé, P., Endres, C., Hermanns, M., Bossa, J.-B., & Potapov, A. (2020). High-resolution gas phase spectroscopy of molecules desorbed from an ice surface: A proof-of-principle study. *ACS Earth Space Sci.*, *4*(1), 86–91. https://doi.org/10.1021/acsearthspacechem.9b00246

Townes, C. H., & Schawlow, A. L. (1975). *Microwave spectroscopy*. New York: Dover Publications.

Ulbricht, H., Zacharia, R., Cindir, N., & Hertel, T. (2006). Thermal desorption of gases and solvents from graphite and carbon nanotube surfaces. *Carbon*, *44*(14), 2931–2942. https://doi.org/https://doi.org/10.1016/j.carbon.2006.05.040

Wakelam, V., Dartois, E., Chabot, M., Spezzano, S., Navarro-Almaida, D., Loison, J.-C., & Fuente, A. (2021). Efficiency of non-thermal desorptions in cold-core conditions - testing the sputtering of grain mantles induced by cosmic rays. *Astron. Astrophys.*, *652*, A63. https://doi.org/10.1051/0004-6361/202039855

Wakelam, V., Loison, J.-C., Herbst, E., Pavone, B., Bergeat, A., Béroff, K., Chabot, M., Faure, A., Galli, D., Geppert, W. D., Gerlich, D., Gratier, P., Harada, N., Hickson, K. M., Honvault, P., Klippenstein, S. J., Picard, S. D. L., Nyman, G., Ruaud, M., … Wester, R. (2015). The 2014 KIDA Network for Interstellar Chemistry. *Astrophys. J., Suppl. Ser.*, *217*(2), 20. https://doi.org/10.1088/0067-0049/217/2/20

Westley, M. S., Baragiola, R. A., Johnson, R. E., & Baratta, G. A. (1995a). Photodesorption from low-temperature water ice in interstellar and circumsolar grains. *Nature*, *373*, 405 –407. https://doi.org/10.1038/373405a0

Westley, M., Baragiola, R., Johnson, R., & Baratta, G. (1995b). Ultraviolet photodesorption from water ice [Dust, Molecules and Backgrounds: from Laboratory to Space]. *Planet. Space Sci.*, *43*(10), 1311–1315. https://doi.org/https://doi.org/10.1016/0032-0633(95)00088-M

Widicus Weaver, S. L., Laas, J. C., Zou, L., Kroll, J. A., Rad, M. L., Hays, B. M., Sanders, J. L., Lis, D. C., Cross, T. N., Wehres, N., McGuire, B. A., & Sumner, M. C. (2017). Deep, broadband spectral line surveys of molecule-rich interstellar clouds. *Astropyhs. J., Suppl. Ser.*, *232*(1), 3. https://doi.org/10.3847/1538-4365/aa8098

Willis, E. R., Garrod, R. T., Belloche, A., Müller, H. S. P., Barger, C. J., Bonfand, M., & Menten, K. M. (2020). Exploring molecular complexity with ALMA (EMoCA): complex isocyanides in Sgr B2(N). *Astron. Astrophys.*, *636*, A29. https://doi.org/10.1051/0004-6361/201936489

Wolff, A. J., Carlstedt, C., & Brown, W. A. (2007). Studies of binary layered CH_3OH/H_2O ices adsorbed on a graphite surface. *J. Phys. Chem. C*, *111*(16), 5990–5999. https://doi.org/10.1021/jp067377x

Wollrab, J. E. (1967). *Rotational spectra and molecular structure*. New York: Academic Press.

Woods, R. C., Dixon, T. A., Saykally, R. J., & Szanto, P. G. (1975). Laboratory microwave spectrum of HCO^+. *Phys. Rev. Lett.*, *35*(19), 1269–1272. https://doi.org/10.1103/PhysRevLett.35.1269

Wu, M. C., Truong, C. M., & Goodman, D. W. (1993). Interactions of alcohols with a nickel oxide(100) surface studied by high-resolution electron energy loss spectroscopy and temperature-programmed desorption spectroscopy. *J. Phys. Chem.*, *97*(37), 9425–9433. https://doi.org/10.1021/j100139a029

Yocum, K. M., Smith, H. H., Todd, E. W., Mora, L., Gerakines, P. A., Milam, S. N., & Widicus Weaver, S. L. (2019). Millimeter/submillimeter spectroscopic detection of desorbed ices: A new technique in laboratory astrochemistry [PMID: 31556610]. *J. Phys. Chem. A*, *123*(40), 8702–8708. https://doi.org/10.1021/acs.jpca.9b04587

Zinner, E. (1998). Stellar nucleosynthesis and the isotopic composition of presolar grains from primitive meteorites. *Ann. Rev. Earth Planet. Sci.*, *26*(1), 147–188. https://doi.org/10.1146/annurev.earth.26.1.147

Ziurys, L. M., Apponi, A. J., Guélin, M., & Cernicharo, J. (1995). Detection of MgCN in IRC +10216: A new metal-bearing free radical. *Astrophys. J.*, *445*, L47–L50. https://doi.org/10.1086/187886